

UNIVERSITY OF CALIFORNIA

Santa Barbara

Carrier Transport Effects in High Speed Quantum Well Lasers

A Dissertation submitted in partial satisfaction
of the requirements for the degree of

Doctor of Philosophy

in

Electrical and Computer Engineering

by

Radhakrishnan Lakshmanan Nagarajan

Committee in charge:

Professor John E. Bowers, Chairperson

Professor Larry A. Coldren

Professor Evelyn L. Hu

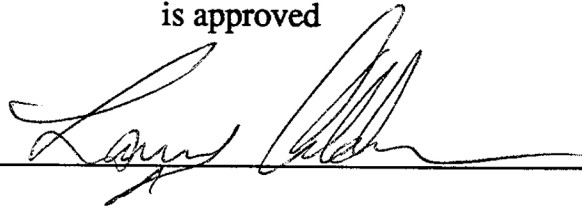
Professor Takeshi Kamiya (University of Tokyo)

Professor Mark J. Rodwell

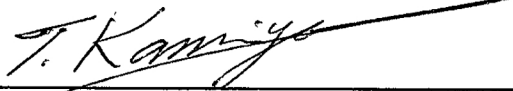
July 1992

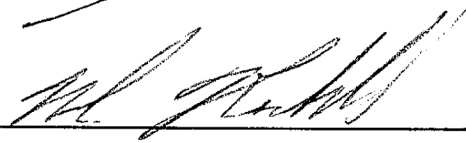
The dissertation of Radhakrishnan Lakshmanan Nagarajan

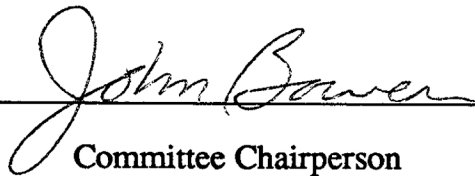
is approved











Committee Chairperson

July 1992

July 30, 1992

Copyright by
Radhakrishnan Lakshmanan Nagarajan
1992

ACKNOWLEDGMENTS

This dissertation sums up my past three years of work at the University of California, Santa Barbara. From the very first days in this country, I had the good fortune of meeting and working with many wonderful people, without whose help and support this dissertation would not have been possible.

Prof. John Bowers, my dissertation advisor, deserves a special thank you for giving me the independence that I relished so much during my graduate work, and for being completely supportive of my ideas.

I benefited much from the interactions with the fellow graduate students, visiting researchers and Professors in the department, and I regret not being able to thank them all by name. The general atmosphere in the laboratories was very conducive to research and personal development.

Good devices start with good material, and for the great molecular beam epitaxy (MBE) grown wafers that I worked with, I am indebted to Dr. Randall Geels, who is presently with the Spectra Diode Laboratories, and Richard Mirin. The very first wafers that I worked with were grown by Dr. Robert Simes, who is presently with the Alcatel Alsthom Recherche in Paris, and Bruce Young.

I would like acknowledge the visiting Japanese researchers, Toru Fukushima from the Furukawa Electric Co. and Masayuki Ishikawa from the Toshiba Corp., for their help with the noise spectra measurements and the collaboration on the various aspects of the work.

The high speed laser mounting technique that was essential to this work was developed largely through the ingenuity of Alan Mar, to whom I am grateful. I would also like to acknowledge the technical help in this area from Thomas Reynolds.

I would like to thank Scott Corzine for the program to calculate gain in strained materials, Chih Ping Chao and Jeff Scott for training me on the reactive ion etching (RIE) machine, and Yih Guey Wey, John Wasserbauer and Dr. Deborah Crawford, who is presently with the Jet Propulsion Laboratories, for their initial help in device processing, mask layout and use of the clean room facilities. I also benefited from the interactions with Dubravko Babic, Dennis Derickson, James Dudley, Roger Helkey, Judith Karin and other members of the Ultrafast Optoelectronics group.

I am thankful to Prof. Herbert Kroemer and Prof. Umesh Mishra who helped to clarify many aspects of carrier transport in semiconductor lasers, and Prof. Kazuro Kikuchi of the University of Tokyo for many useful discussions pertaining to noise in semiconductor lasers. I would like to thank Prof. Larry Coldren, Prof. Evelyn Hu, Prof. Mark Rodwell and Prof. Takeshi Kamiya (University of Tokyo) for being on my Ph.D. committee.

I would like thank the funding agencies, Rome Laboratories (Hanscom AFB) and DARPA, for the financial support of this work.

Dedicated

to

Ayano

VITA

- April 18, 1962:** Born, South India
- 1981 - June 1982:** Military Service, Singapore Armed Forces
- April 1986:** B. Eng. (1st Class Honours), Electrical Engineering
National University of Singapore, Singapore
- April 1986 - April 1987:** Completion of Military Service, Singapore Armed Forces
- September 1989:** M. Eng., Electronic Engineering
University of Tokyo, Japan
- Fall 1989 - June 1992:** Research Assistant, Department of Electrical & Computer
Engineering, University of California, Santa Barbara

PUBLICATIONS

1. R. Nagarajan, M. Fukazawa, and T. Kamiya, "Ultrashort Pulse Generation from Very Low Threshold Quantum Well Lasers," *JSAP-MRS International Conference on Electronic Materials (ICEM)*, paper W30, Tokyo, Japan, June 1988.
2. R. Nagarajan, T. Kamiya, and A. Kurobe, "Effects of Bandfilling on the Threshold Current of GaAs/AlGaAs Multi Quantum Well Lasers," *11th International Semiconductor Laser Conference*, paper C1, Boston, USA, September 1988.
3. Y. T. Lee, R. Takahashi, H. F. Liu, R. Nagarajan, and T. Kamiya, "Ultrashort Diode Laser Pulse Separation by Dispersive Fibers Suitable for Novel Time/Wavelength Division Multiplexing," *Conference on Lasers and Electrooptics (CLEO) '89*, paper TUJ12, Baltimore, USA, April 1989
4. R. Nagarajan, T. Kamiya and A. Kurobe, "Bandfilling in GaAs/AlGaAs Multi Quantum Well Lasers and its Effects on the Threshold Current," *J. Quantum Electron.*, vol. 25, no. 6, pp. 1161-1170, June 1989.
5. R. Nagarajan, and T. Kamiya, "Wavelength Switching in Multi Quantum Well Lasers: Novel Method for Generation of Ultrashort Optical Pulses," *7th International Conference on Integrated Optics and Optical Fiber Communication (IOOC) '89*, paper 20B1-6, Kobe, Japan, July 1989.

6. R. Nagarajan, T. Kamiya, A. Kasukawa, and H. Okamoto, "Generation of Ultrashort , FWHM < 4 ps, Optical Pulses from Long Wavelength Multiple Quantum Well Lasers by Electrical Gain Switching," *7th International Conference on Integrated Optics and Optical Fiber Communication (IOOC) '89*, paper 20PDB-8, Kobe, Japan, July 1989.
7. R. Nagarajan, T. Kamiya, A. Kasukawa, and H. Okamoto, "Observation of Ultrashort (<4 ps) Gain Switched Optical Pulses from Long Wavelength Multiple Quantum Well Lasers," *Appl. Phys. Lett.*, vol. 55, no. 13, pp. 1273-1275, September 1989.
8. R. Nagarajan, A. Kasukawa, I. J. Murgatroyd, T. Kamiya, and H. Okamoto, "Single Longitudinal Mode Operation of a Fabry Perot InP/InGaAsP Multi-Quantum Well Laser Under Direct Modulation," *Optoelectronics-Devices and Technol.*, vol. 5, no. 1, pp. 65-69, June 1990.
9. R. Nagarajan, "High Density Excitation Effects in Quantum Well Lasers," Masters Thesis submitted to the Department of Electronic Engineering, University of Tokyo, September 1989 (unpublished).
10. J. E. Bowers, D. L. Crawford, Y. G. Wey, R. Nagarajan, and J. Wasserbauer, "High Speed Lasers and Photodetectors," *Armed Forces Communications and Electronics Association (AFCEA), Dept. of Defense Fiber Optics Conference '90*, McLean (Virginia), USA, March 1990.
11. J. R. Karin, L. G. Melcer, R. Nagarajan, J. E. Bowers, S. W. Corzine, R. S. Geels, and L. A. Coldren, "Picosecond Gain Switching of Surface Emitting Lasers," *Conference on Lasers and Electro-Optics (CLEO) '90*, paper CFC2, Anaheim, USA, May 1990.
12. L. G. Melcer, J. R. Karin, R. Nagarajan, S. W. Corzine, and J. E. Bowers, "Minimum Pulsewidth and Delay for Multiple Quantum Well Vertical Cavity Lasers," *22nd Conference on Solid State Devices and Materials (SSDM) '90*, paper D-3-3, pp. 525-528 (*Extended Abstracts*), Sendai, Japan, July 1990.
13. J. R. Karin, L. G. Melcer, R. Nagarajan, J. E. Bowers, S. W. Corzine, P. A. Morton, R. S. Geels, and L. A. Coldren, "Generation of Picosecond Pulses with a Gain switched GaAs Surface Emitting Laser," *Appl. Phys. Lett.*, vol. 57, no. 10, pp. 963-965, July 1990.
14. J. E. Bowers, D. J. Derickson, R. J. Helkey, J. R. Karin, A. Mar, P. A. Morton, and R. Nagarajan, "Picosecond Dynamics in Semiconductor Lasers," *12th International Semiconductor Laser Conference*, paper A-3, Davos, Switzerland, September 1990.

15. R. Nagarajan, T. Fukushima, J. Bowers, R. Geels, and L. Coldren, "High Speed InGaAs/GaAs Strained Multiple Quantum Well Ridge Waveguide Lasers with Low Damping," *Optical Fiber Communication Conference (OFC) '91*, paper PD8, San Diego, USA, February 1991.
16. D. L. Crawford, R. Nagarajan, and J. E. Bowers, "Comparison of Bulk and Quantum Wire Photodetectors," *Appl. Phys. Lett.*, vol. 58, no. 15, pp. 1629-1631, April 1991.
17. L. G. Melcer, J. R. Karin, R. Nagarajan, J. E. Bowers, "Picosecond Dynamics of Optical Gain Switching in Vertical Cavity Surface Emitting Lasers," *J. Quantum Electron.*, vol. 27, no. 6, pp. 1417-1425, June 1991.
18. R. Nagarajan, T. Fukushima, and J. Bowers, "High Speed and Noise Properties of Strained InGaAs/GaAs Multiple Quantum Well Lasers," *Engineering Foundation Conference on High Speed/High Frequency Optoelectronics*, Palm Coast (Florida), USA, March 1991.
19. J. R. Karin, R. Nagarajan, L. G. Melcer, and R. S. Geels, "Gain Switching in Vertical Cavity Lasers," *Engineering Foundation Conference on High Speed/High Frequency Optoelectronics*, Palm Coast (Florida), USA, March 1991.
20. R. Nagarajan, T. Fukushima, J. E. Bowers, R. S. Geels, and L. A. Coldren, "Comparison of Modulation and Noise Properties of Strained InGaAs and Unstrained GaAs Single Quantum Well Lasers," *Conference on Lasers and Electro-Optics (CLEO) '91*, paper CTuK1, Baltimore, USA, May 1991.
21. R. Nagarajan, T. Fukushima, J. E. Bowers, R. S. Geels, and L. A. Coldren, "High Speed InGaAs/GaAs Strained Multiple Quantum Well Lasers with Low Damping," *Appl. Phys. Lett.*, vol. 58, no. 21, pp. 2326-2328, May 1991.
22. R. Nagarajan, T. Fukushima, J. E. Bowers, R. S. Geels, and L. A. Coldren, "High Speed Single Quantum Well InGaAs/GaAs Laser Design and Experiment," *Device Research Conference '91*, paper IIA-1, Boulder, USA, June 1991.
23. R. Nagarajan, T. Fukushima, J. E. Bowers, R. S. Geels, and L. A. Coldren, "Single Quantum Well Strained InGaAs/GaAs Lasers with Large Modulation Bandwidth and Low Damping," *Electron. Lett.*, vol. 27, no. 12, pp. 1058-1060, June 1991.

24. R. Nagarajan, T. Fukushima, J. E. Bowers, R. S. Geels, and L. A. Coldren, "High Speed Strained InGaAs/GaAs Quantum Well Lasers," *Government Microcircuit Applications Conference (GOMAC) '91*, paper 10.7, Orlando, USA, November 1991.
25. R. Nagarajan, T. Fukushima, S. W. Corzine, J. E. Bowers, "Effects of Carrier Transport on High Speed Quantum Well Lasers," *Appl. Phys. Lett.*, vol. 59, no. 15, pp. 1835-1837, October 1991.
26. T. Fukushima, R. Nagarajan, J. E. Bowers, R. A. Logan, and T. Tanbun-Ek, "Relative Intensity Noise Reduction in InGaAs/InP Multiple Quantum Well Lasers with Low Nonlinear Damping," *Photon. Tech. Lett.*, vol. 3, no. 8, pp. 691-693, September 1991.
27. M. Ishikawa, T. Fukushima, R. Nagarajan, and J. E. Bowers, "Temperature Dependence of Damping in High Speed Quantum Well Lasers," *Optical Society of America (OSA) Annual Meeting*, paper TuHH4, San Jose, USA, November 1991.
28. R. Nagarajan, T. Fukushima, J. E. Bowers, R. S. Geels, and L. A. Coldren, "High Speed Single Quantum Well Strained InGaAs/GaAs Lasers," *17th European Conference on Optical Communication (ECOC) '91/8th International Conference on Integrated Optics and Optical Fiber Communication (IOOC) '91*, paper Tu.A4.3, Paris, France, September 1991.
29. R. Nagarajan, M. Ishikawa, T. Fukushima, R. S. Geels and J. E. Bowers, "Carrier Transport Effects in High-Speed Quantum-Well Lasers," *Laser Diode Technology and Applications IV, OE/LASE '92 (SPIE Conference #1634)*, paper 1634-14, Los Angeles, USA, January 1992.
30. R. Nagarajan, T. Fukushima, M. Ishikawa, J. E. Bowers, R. S. Geels, and L. A. Coldren, "Transport Limits in High Speed Quantum Well Lasers: Experiment and Theory," *Photon. Tech. Lett.*, vol. 4, no. 2, pp. 121-123, February 1992.
31. R. Nagarajan, T. Fukushima, M. Ishikawa, J. E. Bowers, R. S. Geels, and L. A. Coldren, "Transport Limits in High Speed Quantum Well Lasers," *Optical Fiber Communication Conference (OFC) '92*, paper ThB5, San Jose, USA, February 1992.
32. R. Nagarajan, and J. E. Bowers, "Carrier Transport in High Speed Quantum Well Lasers," *Workshop on Compound Semiconductor Materials and Devices (WOCSEMMAD '92)*, San Antonio, USA, February 1992.

33. R. Nagarajan, M. Ishikawa and J. E. Bowers, "Effects of Carrier Transport on Relative Intensity Noise and Modulation Response in Quantum Well Lasers," *High-Speed Electronics and Optoelectronics, Symposium on Compound Semiconductor Physics and Devices, (SPIE Conference #1680)*, paper 1680-11, Somerset (New Jersey), USA, March 1992.
34. R. Nagarajan, M. Ishikawa, and J. E. Bowers, "Effects of Carrier Transport on Relative Intensity Noise and Critique of K Factor Prediction of Modulation Response," *Electron. Lett.*, vol. 28, no. 9, pp. 846-847, April 1992.
35. M. Ishikawa, T. Fukushima, R. Nagarajan, and J. E. Bowers, "Temperature Dependence of Damping in High Speed Quantum Well Lasers," *Appl. Phys. Lett.*, July 1992.
36. R. Nagarajan, M. Ishikawa, T. Fukushima, R. S. Geels and J. E. Bowers, "High Speed Quantum Well Lasers and Carrier Transport Effects," *J. Quantum Electron.*, 1992.
37. M. Ishikawa, R. Nagarajan, T. Fukushima, J. Wasserbauer, and J. E. Bowers, "Long Wavelength High Speed Semiconductor Lasers with Carrier Transport Effects," *J. Quantum Electron.*, October 1992.
38. R. Nagarajan, R. P. Mirin, T. E. Reynolds, and J. E. Bowers, "Effect of the Confinement Layer Composition on the Internal Quantum Efficiency and Modulation Response of Quantum Well Lasers," *Photon. Tech. Lett.*, August 1992.
39. R. Nagarajan, R. P. Mirin, T. E. Reynolds, and J. E. Bowers, "Carrier Confinement and its Effect on the Internal Quantum Efficiency and Modulation Response of Quantum Well Lasers," *13th International Semiconductor Laser Conference.*, Takamatsu, Japan, September 1992.
40. R. Nagarajan, and J. E. Bowers, "Effects of Bandfilling and Thermionic Emission on the Modulation response of Quantum Well Lasers," *Engineering Foundation Conference on High Speed Optoelectronic Devices and Circuits II*, Banff (Alberta), Canada, August 1992.
41. T. Fukushima, R. Nagarajan, M. Ishikawa, and J. E. Bowers, "High-Speed Dynamics in InP based Multiple Quantum Well Lasers," submitted to *Jpn. J. Appl. Phys.*

ABSTRACT

Carrier Transport Effects in High Speed Quantum Well Lasers

by

Radhakrishnan Lakshmanan Nagarajan

This dissertation deals with the design, fabrication, testing and analysis of high speed quantum well lasers. The use of quantum wells as the active area in semiconductor lasers was predicted to enhance the differential gain, and hence the modulation response, compared to the first generation bulk active area devices.

Although the enhancement of the intrinsic differential gain is important, the carrier transport effects tend to be the more dominant factor in the design and performance of high speed quantum well lasers. A small signal carrier transport model is proposed and derived in detail for the operation of forward biased *p-i-n* semiconductor laser diodes. The transport model is incorporated into the small signal rate equation model for the carrier and photon densities in the laser cavity. Simple analytic expressions are obtained for the modulation response, relative intensity noise, resonance frequency, damping rate and *K* factor including the effects of carrier transport.

Extensive experimental evidence, over a range of temperatures, is presented for the validity of the carrier transport model. The design and fabrication of high speed quantum well lasers based on the proposed model is presented. High speed ridge waveguide lasers fabricated by reactive ion etching using a self aligned mask process are demonstrated. These lasers have minimum threshold currents lower than 5 mA and maximum modulation bandwidths of 22 GHz.

TABLE OF CONTENTS

ABSTRACT.....	xii
LIST OF FIGURES.....	xvi
LIST OF SYMBOLS.....	xviii
1. INTRODUCTION	
1.1 Background.....	1
1.2 Scope and Organization of the Dissertation	8
References	10
2. CARRIER TRANSPORT MODEL	
2.1 Transport Across the SCH.....	16
2.2 Carrier Distribution in the SCH.....	20
2.3 SCH Transport Factor	21
2.4 Ballistic Carrier Transport.....	23
2.5 Carrier Capture Time of the Quantum Well.....	25
2.6 Effects of a Graded SCH Layer on Carrier Transport	27
2.7 Thermionic Emission	28
2.8 Tunneling.....	29
2.9 Multiple Quantum Well Structure	29
2.10 Effect of Interface Recombination.....	31
2.11 Analysis of Laser Dynamics.....	33
References	35
3. RATE EQUATION ANALYSIS	
3.1 Rate Equations	39
3.2 Modulation Response.....	41
3.3 Experimental Results - Effect of varying τ_r	45
3.4 Experimental Results - Effect of varying τ_e	50
3.5 Relative Intensity Noise (<i>RIN</i>) Spectrum.....	52

3.6 Experimental Results	57
3.7 Temperature Dependence Data.....	59
3.8 Maximum Possible Modulation Bandwidth.....	62
References	65
4. INTERNAL QUANTUM EFFICIENCY	
4.1 Background.....	68
4.2 Theoretical Expression Including Carrier Transport Effects.....	69
4.3 Experimental and Theoretical Results	71
References	75
5. OPTIMIZATION OF HIGH SPEED LASERS	
5.1 Material Considerations for the Enhancement of Differential Gain.....	77
5.2 Maximization of the Optical Confinement Factor.....	78
5.3 Optimization of the Quantum Well Width.....	81
5.4 Optimization of the Barrier Width.....	85
5.5 Optimization of the Barrier Height/Carrier Confinement Potential	86
5.6 Optimization of the Separate Confinement Heterostructure Width.....	87
5.7 Optimization of the Cavity Length	90
5.8 Experimental Results	91
References	99
6. DEVICE FABRICATION	
6.1 Broad Area Lasers.....	103
6.2 Self Aligned Polyimide Buried Ridge Waveguide Lasers	109
6.3 Static Characteristics of Narrow Ridge Waveguide Devices	115
6.4 Microwave Mounting and Measurement of Laser Diodes	118
References	122
7. CONCLUSION	123
APPENDIX A: BROAD AREA CHARACTERISTICS	128
APPENDIX B: MATERIAL PARAMETERS	
B.1 Bandgaps, Effective Masses and Refractive Indices.....	130

B.2 Electron and Hole Mobilities and Diffusion Coefficients	132
B.3 Optical Gain and its Temperature Dependence	136
References	139

APPENDIX C: DETAILS OF RATE EQUATION ANALYSIS

C.1 Small Signal Expansion of the Stimulated Emission Term.....	142
C.2 Maximum Modulation Bandwidth in terms of the K Factor	143

APPENDIX D: DEVICE AND MOUNT PARASITICS

D.1 Parameter Extraction from Network Analyzer Measurements.....	145
D.2 Independent Diode Series Resistance Measurements	151
References	156

LIST OF FIGURES

Fig. 1.1 Conventional approach to the design of high speed lasers	3
Fig. 1.2 Effects of carrier transport on the high speed laser parameters	7
Fig. 2.1 Single quantum well laser with separate confinement heterostructure	16
Fig. 2.2 Variation of the electron and hole transport times for a GaAs barrier	31
Fig. 3.1 Exact and analytical solutions to the modulation response	44
Fig. 3.2 Measured and calculated modulation response for a wide SCH laser.....	46
Fig. 3.3 Measured and calculated modulation response for a narrow SCH laser	47
Fig. 3.4 Variation of modulation bandwidth with square root of power.....	49
Fig. 3.5 Variation of γ_0 with SCH width	50
Fig. 3.6 Resonance frequency for devices with different SCH energy barriers	51
Fig. 3.7 Exact and analytical solutions to the <i>RIN</i> spectrum	55
Fig. 3.8 Comparison of noise spectrum and modulation response	56
Fig. 3.9 Dependence of g_0 and ϵ on SCH width	57
Fig. 3.10 Variation of the intrinsic linewidth with inverse of the optical power.....	58
Fig. 3.11 Temperature dependence of <i>K</i> factor for SQW lasers	60
Fig. 3.12 Temperature dependence of transport times and transport factor, χ	62
Fig. 3.13 Maximum possible modulation bandwidth.....	63
Fig. 4.1 Variation of internal quantum efficiency with Al content in the SCH.....	72
Fig. 4.2 Variation of internal quantum efficiency with temperature.....	73
Fig. 5.1 Approaches to enhance differential gain in semiconductor lasers	77
Fig. 5.2 Optical confinement factor for different energy profiles in the SCH.....	80
Fig. 5.3 Variation of the optical confinement factor with SCH width	81
Fig. 5.4 Optical confinement factor and the transparency carrier density.....	83
Fig. 5.5 Variation of differential gain with quantum well width	84
Fig. 5.6 Variation of modulation bandwidth with barrier thickness	85
Fig. 5.7 Variation of internal quantum efficiency with Al mole fraction.....	86
Fig. 5.8 Variation of modulation bandwidth when cladding loss dominates	88

Fig. 5.9	Variation of modulation bandwidth when active area loss dominates	89
Fig. 5.10	Calculated variation in modulation bandwidth with cavity length.....	91
Fig. 5.11	Experimental variation in modulation bandwidth with SCH width	92
Fig. 5.12	Experimental variation in modulation bandwidth with cavity length	93
Fig. 5.13	Cavity length dependence of the D factor for a 3 QW sample	94
Fig. 5.14	Variation of resonance frequency for different ridge widths.....	95
Fig. 5.15	Modulation response of an optimized 3 QW sample	96
Fig. 5.16	Variation of the gain compression factor with cavity length.....	97
Fig. 6.1	RIE system and the laser reflectivity measurement setup	104
Fig. 6.2	Variation of the reflected laser signal from the sample during Cl_2 RIE	106
Fig. 6.3	Fabrication steps for the polyimide buried ridge waveguide lasers	110
Fig. 6.4	Definition of the degree of planarization in the polyimide process	112
Fig. 6.5	Variation of the reflected signal for the O_2 etching of polyimide.....	113
Fig. 6.6	Polyimide buried ridge waveguide laser.....	114
Fig. 6.7	Longitudinal mode spectrum above threshold	115
Fig. 6.8	Variation of threshold current with ridge width.....	116
Fig. 6.9	Variation of threshold current with temperature for SQW lasers	118
Fig. 6.10	Schematic diagram of the high speed laser mount.....	119
Fig. 6.11	Experimental setup for the measurement of modulation response.....	120
Fig. 6.12	Experimental setup for the measurement of relative intensity noise.....	121
Fig. A.1	Conduction band energy diagram for the structures in this work	128
Fig. B.1	Electron Hall mobility in $\text{Al}_x\text{Ga}_{1-x}\text{As}$	134
Fig. B.2	Hole Hall mobility in $\text{Al}_x\text{Ga}_{1-x}\text{As}$	135
Fig. B.3	Variation of material gain with current density	137
Fig. B.4	Temperature dependence of gain-carrier density relationship	138
Fig. D.1	Equivalent circuit of a packaged laser diode.....	146
Fig. D.2	Equivalent circuit of laser diode active area	147
Fig. D.3	Equivalent circuit used for parameter extraction from S_{11} data	149
Fig. D.4	Passband response of the equivalent parasitic circuit of Sample C.....	150
Fig. D.5	$I \, dV/dI$ as a function of I for Sample C with the widest SCH	152

LIST OF SYMBOLS

A	area of cross section
α_a, α_b	internal loss fitting parameters
α_{active}	loss in the active layer
α_{cladding}	loss in the cladding region
$\alpha_{\text{int}}, \alpha_{\text{tot}}$	internal loss
α_{mir}	mirror loss
α_{SCH}	SCH (separate confinement heterostructure) transport factor
χ	transport factor ($= 1 + \tau_r/\tau_e$)
c	velocity of light in the vacuum
C_B	package capacitance due to the bond wire-microstrip transition
C_D	diffusion capacitance
C_P	parasitic capacitance of the laser diode structure
C_{SC}	space charge capacitance
$(\delta f)_{\text{ST}}$	intrinsic Schawlow-Townes linewidth
D	D factor - rate of increase of resonance frequency with the square root of optical power
D, D_n, D_p	diffusion coefficient (n - electrons, p - holes)
D_a	ambipolar diffusion coefficient
$\Delta\lambda$	mode spacing
E	electric field
ε	gain compression factor
E_1, E_2	odd and even perturbed energy levels
E_B	effective barrier height
E_g	direct bandgap (Γ point)
E_o, E_d	energy parameters used in the single effective oscillator model
ε_r	relative permittivity

f_{\max}, ω_{\max}	maximum possible intrinsic modulation bandwidth
F_r	Langevin force caused by spontaneous emission events
f_r, ω_r	resonance frequency ($\omega_r = 2 \pi f_r$)
Γ	optical confinement factor
γ	damping rate
G, G_0	carrier density dependent gain (o - steady state)
g, g_0	differential gain (o - steady state)
γ_0	D.C. offset in the γ - f_r^2 relationship
η	diode ideality factor
h	Planck constant
η_d	slope or differential efficiency of the L/I curve
η_{ext}	external quantum efficiency
η_i	internal quantum efficiency
$h\nu$	photon energy
i	small signal variation of the injected current
I, I_0, I_S	steady state injected current (o - steady state)
I_{bias}	bias current level of the laser diode
I_L	D. C. leakage current in a laser diode
I_W	steady state current flowing into the quantum well
J_{int}	interface recombination current
J_n, J_p	current density (n - electrons, p - holes)
J_{th}	threshold current density
K	K factor - rate of increase of damping rate with the square of resonance frequency
k	Boltzmann constant
kT/q	thermal voltage (= 25.9 mV at $T = 300$ K)
λ	wavelength of operation of the laser

L_a, L_{ao}	ambipolar diffusion length
L_B	bond wire inductance
L_B	width of barrier
L_c	cavity length
L_I	photon storage inductance (small signal parameter of the laser active area)
L_{mstrip}	length of microstrip
L_S	width of one side of separate confinement heterostructure (SCH)
L_W	width of quantum well
m^*, m_e, m_h	carrier effective mass (e - electrons, h - holes)
m_o	free electron mass
n	generic notation for carrier density except in the rate equation analysis
ν, f, ω	frequency ($\omega = 2 \pi \nu$ or $2 \pi f$)
N_B	number of carriers in the SCH
n_{mode}	mode index
N_{st}	interface defect density (per unit area)
N_W	number of carriers in the quantum well
π	pi (= 3.1415926...)
p_B	small signal variation of the carrier density in the SCH
P_B, P_{Bo}	carrier density in the SCH (o - steady state)
p_W	small signal variation of the carrier density in the quantum well
P_W, P_{Wo}	carrier density in the quantum well (o - steady state)
θ	angle of incidence of the monitor beam
q	electronic charge
R_1, R_2	front and rear facet reflectivity
R_B	bond wire resistance
R_C	resistance of cables and the probe
R_d	intrinsic diode resistance(= $\eta kT/qI_{bias}$)

r_H	Hall factor
R_S	diode series resistance
R_{S1}, R_{S2}	resistance elements in the small signal model of the laser diode active area
R_D	area
R_{SUB}	substrate resistance
σ	parameter used in the single effective oscillator model
s	small signal variation of photon density
S, S_o	photon density (o - steady state)
S_{11}, S_{21}	scattering parameters
σ_c	carrier capture cross section
S_i	interface recombination velocity
T	temperature
τ_a	ambipolar diffusion time
τ_b	barrier transport time
τ_c	effective barrier transport time
τ_e	thermionic emission time from the quantum well
τ_n	bimolecular recombination lifetime
τ_{nb}	total recombination lifetime in the SCH
τ_{nr}	nonradiative recombination lifetime in the quantum well
T_o	characteristic temperature
τ_p	photon lifetime
τ_r	carrier transport and capture across the SCH
τ_t	tunneling time between quantum well
$(V_j)_{th}$	<i>p-n</i> junction voltage at threshold
v_g	optical mode velocity
V_j	<i>p-n</i> junction voltage
V_{SCH}	volume of one side of the separate confinement heterostructure
v_{th}	carrier thermal velocity
V_W	volume of the quantum well

μ, μ_e, μ_h	mobility (e - electrons, h - holes)
$\mu_{300\text{ K}}$	mobility at 300 K
μ_d	drift (conductivity) mobility
μ_H	Hall mobility

CHAPTER 1

INTRODUCTION

1.1 Background

Semiconductor lasers that can be directly current modulated at high bit rates are a key requirement for high speed optical communication links. Directly intensity modulated transmitter systems are simpler to implement compared to ones employing external modulation. The crucial part of such a system implementation is the design and fabrication of high speed semiconductor lasers.

In principle, there are two aspects to designing high speed lasers. One is the physical aspect which involves the optimization of the active area epitaxial layers for high speed operation. The other is the device aspect which involves the fabrication of a structure, incorporating this optimized active area, that has sufficient bandwidth for the input current signal to efficiently intensity modulate the light output. Both aspects are equally important for the realization of practical high speed semiconductor lasers.

The high speed laser design begins with the quantitative treatment of the current modulation process in semiconductor lasers. The dynamics in semiconductor lasers have been conventionally modeled using a set of two coupled first order linear differential equations; one for the carrier density and the other for the photon density in the cavity [1-5]. Using this approach, the small signal response of the laser can be written as a second order transfer function, and the modulation bandwidth of such a system is determined by its resonance frequency, f_r , and the damping rate, γ . From

the small signal analysis of these rate equations, the resonance frequency and the damping rate can be written in terms of more fundamental parameters; $f_r = (1/2\pi) \sqrt{v_g g' S / \tau_p}$ and $\gamma = g' S + \epsilon S / \tau_p$, where v_g is the group velocity in the cavity, g' is the differential gain, S is the photon density, τ_p is the photon lifetime and ϵ is the gain compression factor [1-5].

In this analysis, the intrinsic limit to the speed operation of the laser is the cavity loss rate determined by the photon lifetime. Further, the optical gain is also photon density dependent, i.e. it saturates at high photon density levels, and this provides an additional source of damping. This nonlinear photon density dependence of optical gain is introduced into the rate equation formalism via a phenomenological gain compression factor, ϵ [6]. The gain or the differential gain in the laser cavity is then written as, $g' = g_o / (1 + \epsilon S)$, and in the case of small ϵS , keeping only the linear term of the Taylor expansion, it is also sometimes written as $g' = g_o (1 - \epsilon S)$ where g_o is the differential gain component determined solely by material parameters and may also be carrier density dependent. The physical origins of the gain compression factor are primarily spectral hole burning [7,8,9] and transient carrier heating [10,11,12].

The damping rate, γ , varies linearly with f_r^2 , and the proportionality constant is called the K factor [5]; $K = 4\pi^2 (\tau_p + \epsilon / v_g g_o)$. The maximum possible intrinsic modulation bandwidth is determined solely by this factor, $f_{\max} = \sqrt{2} \frac{2\pi}{K}$, and thus K is often taken as a figure of merit for high speed semiconductor lasers. Lasers with smaller K factors have also been shown to have a lower level of relative intensity noise (RIN) at low frequencies [13].

In practice, the maximum possible modulation bandwidth is usually limited by RC parasitics, device heating and maximum power handling capability of the laser,

especially the facets. It will be shown later that, particularly in quantum well lasers, carrier transport effects (diffusion, tunneling and thermionic emission) are also important and often the dominant limit.

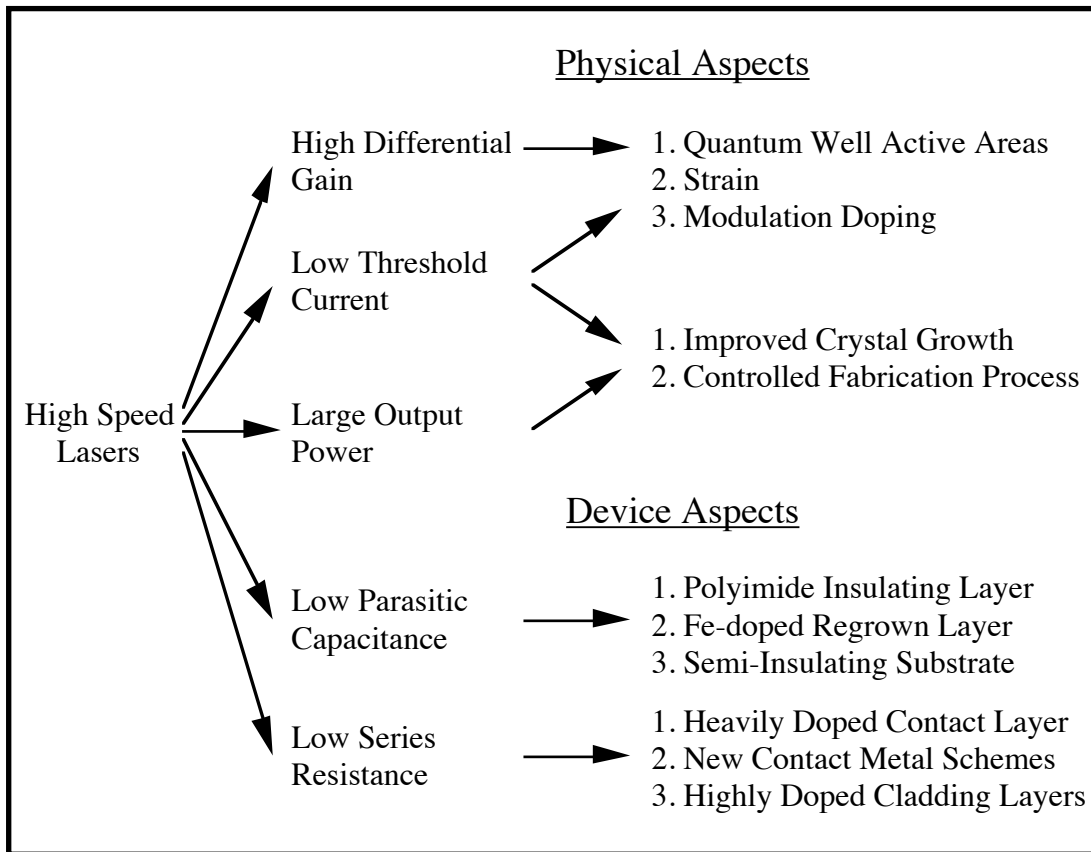


Fig. 1.1 Conventional approach to the design of high speed lasers.

Fig. 1.1 shows the schematic diagram of the conventional approach to designing high speed lasers. For the physical aspect, one used the expression for f_T as a guide, and designed lasers with tight optical mode confinement for high photon densities, short cavity lengths for short photon lifetimes, and p -doped active areas [14,15] for high differential gain. Lasers with quantum well active areas have been

theoretically and experimentally shown to have enhanced differential gain over the bulk lasers [16]. Additional enhancements can be obtained with the inclusion of strain [17,18,19], p -doping or modulation doping [20]. This led to theoretical predictions of increased modulation bandwidth in quantum well lasers [21].

Low threshold current is essential to obtain high optical powers and photon densities at low operating currents. This will minimize the detrimental effects of thermal heating at high current levels. High external quantum efficiency (low internal loss) is desirable, again for the same reason: to achieve a high operating powers at a low operating current.

Small parasitic capacitance is essential for a high speed device. The use of a polyimide dielectric layer or as in the InP material system, the use of a thick highly resistive semi-insulating Fe-doped InP layer, will reduce the parasitic capacitance. In addition, a reduction in the area of the bonding pads will reduce the parasitic capacitance even further.

Low series resistance is crucial not only for the reduction of the device parasitics, but also for the minimization of the heating effects discussed previously. The major components of the total series resistance are the contributions from the p -contacts, top p -cladding region and heterojunction interfaces. Heavily doped cap layers and different alloyed contact metal schemes have been used to minimize the contact resistance. Grading the GaAs cap layer to some intermediate composition of the smaller bandgap InGaAs has also shown to help minimize the contact resistance. The bulk resistance can be reduced by highly doping the cladding regions. Highly doped cladding layers, because their proximity to the active region, can increase the

internal loss of the laser to unacceptably high levels. This is then the upper limit to the doping that may be incorporated to minimize the series resistance.

Despite the application of these principles to the design of high speed lasers, it is only recently that the modulation bandwidth in quantum well lasers have been comparable to or better the best bulk lasers, with the quantum well lasers in the InGaAs/GaAs system [22,23] presently performing better than those in the GaAs/AlGaAs [24] and the InP systems [25,26]. Further there is a large variation in the K factors reported for quantum well lasers; 0.13 ns to 2.4 ns [13,25,27-30] implying a maximum possible intrinsic modulation bandwidth ranging from 68 GHz to 4 GHz, while K values for the bulk lasers have been in the narrow range of 0.2 ns to 0.4 ns [9]. Although the ϵ values quoted for lasers in the InGaAs/InP [9,13,27,30] system on the average are higher than the ones that we have reported for the InGaAs/GaAs system [29], they are by no means anomalously high or enhanced in quantum well lasers as they were initially speculated to be [28]. Experimental reports seem to indicate that ϵ is independent of the laser structure, and is even unaffected by the inclusion of strain, compressive or tensile, in the quantum wells [25,27,29,30].

The higher K values in some quantum well lasers over the bulk ones have been explained by either an increase in the nonlinear gain compression factor, ϵ , or a reduction in the differential gain. It has been theoretically proposed that ϵ is enhanced by quantum confinement [31], and the inclusion of strain increases it even more [32]. In Reference [33], the authors have used a spectral holeburning model for the computation of the intrinsic ϵ and its variation with quantum confinement, and optimized quantum well structures for high speed operation.

A well-barrier holeburning model [34] was proposed, and it concludes that there is an additional contribution to the intrinsic ϵ which is structure dependent. The authors have proposed that this enhancement in ϵ is responsible for the variation in the K factors that have been published.

We proposed a model for high speed quantum well lasers based on carrier transport [35], and numerically calculated the effects of carrier transport on the modulation bandwidth and obtained good agreement with the measurements done on single and multiple quantum well lasers. For the case of single quantum well lasers, we have also derived analytic expressions for the effects of carrier diffusion and thermionic emission on the modulation response [36]. We have showed theoretically and experimentally that the gain compression factor, ϵ , is fairly independent of the laser structure, and that carrier transport has a significant effect on the modulation properties of high speed lasers via a reduction of the *effective* differential gain.

Fig. 1.2 illustrates the difference in these two approaches to explaining the enhancement of K factors in quantum well lasers. From the first order rate equation analysis, the enhancement in the gain compression factor will only affect the damping rate. A reduction in differential gain will affect both the resonance frequency and the damping rate. This is the crux of the work presented here. The model to be derived in detail later in this dissertation clarifies the differences in these two approaches, and shows that the carrier transport effects lead to a reduction in the differential gain in high speed quantum well lasers resulting in a quantity called the *effective* or *dynamic* differential gain.

Starting from a set of rate equations similar to that used in [34], the authors in [37] have derived the same expression as us for the effective differential gain [36]. In

addition, they have also derived an effective gain compression factor which is dependent on the differential gain and the carrier capture and escape times [38]. We do not see this predicted [37] increase in the gain compression factor with the effective differential gain in our experimental data [36].

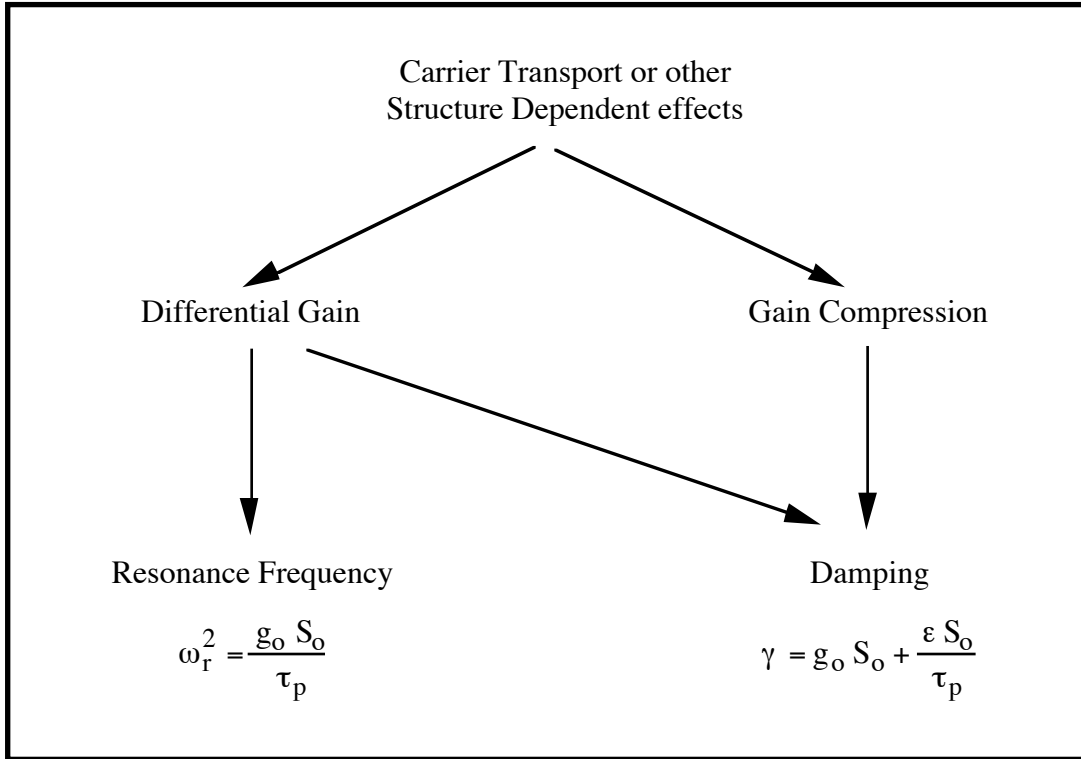


Fig. 1.2 Possible effects of carrier transport on high speed laser parameters.

A large signal numerical model has also been reported to describe the effects of carrier transport and injection bottleneck in the case of quantum well optical amplifiers [39,40]. For the case of large signal modulation, the carrier density in the separate confinement heterostructure (SCH) of the quantum well laser is no longer spatially uniform. To compute this spatial variation in the carrier density, the Poisson equation and the current continuity equation are solved simultaneously. The carrier

density distribution is then input to a set of rate equations to model the dynamic behavior of the optical amplifier.

1.2 Scope and Organization of the Dissertation

In addition to the Introduction, this Dissertation is organized into six chapters and four appendices.

In Chapter two, a small signal ambipolar carrier transport model for forward biased *p-i-n* diodes is proposed. Multiple and single quantum well structures are analyzed, and expressions for the various carrier transport times, viz. diffusion, thermionic emission and tunneling, are derived.

In Chapter three, the carrier transport model is incorporated into the small signal rate equation model for the carrier and photon densities in the laser cavity. Analytic expressions for the resonance frequency, damping rate, and *K* factor are derived for the case of single quantum well (SQW) lasers to include the effects of carrier transport. A numerical model is used in the case of multiple quantum well (MQW) lasers. It is shown theoretically and experimentally that the gain compression factor, ϵ , is fairly independent of the laser structure, and that carrier transport has a significant effect on the modulation properties of high speed lasers via a reduction of the *effective* differential gain and *not* an enhancement of ϵ . In addition, it is also shown that the carrier transport across the SCH can lead to a severe low frequency rolloff. In the presence of such a rolloff and even when *all other* extrinsic device limits are absent, the *K* factor is *no longer* an accurate measure of the maximum possible intrinsic modulation bandwidth in quantum well lasers [41]. Temperature dependence data for the *K* factor is presented as further evidence for the

significant effects of carrier transport [42]. Some experimental and theoretical results from the InGaAs(P)/InP system are also presented [43].

In Chapter four, an expression for the internal quantum efficiency of the quantum well laser is derived from the carrier transport model. Carrier overflow from the quantum wells into the confinement regions, characterized by the thermionic emission process, is shown to have a detrimental effect on the transport properties as well as the internal quantum efficiency of high speed lasers [44].

In Chapter five, the model is used to present design criteria for optimizing quantum well lasers for high speed operation. Among the parameters that are varied, are the width and number of the quantum wells, width and height of the barriers and the confinement regions, the types of compositional grading in the SCH, and the cavity length [45]. Experimental data is also presented in support of this optimization process. High speed MQW lasers with 22 GHz bandwidth are demonstrated [45].

In Chapter six, the details of the self aligned, dry etched fabrication process for the broad area and the polyimide buried ridge waveguide lasers are presented. Static and temperature dependence of threshold current characteristics of the ridge waveguide lasers are also discussed.

Chapter seven concludes the work, and presents some areas of interest and further research in the field of high speed lasers.

Appendix A presents the epitaxial structure and broad area results for the various wafers from which the devices used in this study were fabricated. Appendix B lists the various material parameters, viz. bandgaps, effective masses, refractive indices, carrier mobilities and gain carrier density curves, used as inputs to the carrier transport model. Appendix C presents the detailed derivation of some of the

commonly used terms in the rate equation analysis. Appendix D discusses the various methods to experimentally determine the device parasitics, and presents the results of the measurements done on the present structures.

References

1. R. S. Tucker, "High-Speed Modulation of Semiconductor Lasers," *J. Lightwave Technol.*, vol. 21, pp. 1180-1192, 1985.
2. K. Y. Lau, and A. Yariv, "Ultra-High Speed Semiconductor Lasers," *J. Quantum Electron.*, vol. 21, pp. 121-138, 1985.
3. J. E. Bowers, B. R. Hemenway, A. H. Gnauck, and D. P. Wilt, "High-Speed InGaAsP Constricted-Mesa Lasers," *J. Quantum Electron.*, vol. 22, pp. 833-844, 1986.
4. C. B. Su, and V. Lanzisera, "Ultra-High-Speed Modulation of 1.3 μm InGaAsP Diode Lasers," *J. Quantum Electron.*, vol. 22, pp. 1568-1578, 1986.
5. R. Olshansky, P. Hill, V. Lanzisera, and W. Powazinik, "Frequency Response of 1.3 μm InGaAsP High Speed Semiconductor Lasers," *J. Quantum Electron.*, vol. 23, pp. 1410-1418, 1987.
6. D. J. Channin, "Effect of Gain Saturation on Injection Laser Switching," *J. Appl. Phys.*, vol. 50, pp. 3858-3860, 1979.
7. M. Yamada, and Y. Suematsu, "Analysis of Gain Suppression in Undoped Injection Lasers," *J. Appl. Phys.*, vol. 52, pp. 2653-2664, 1981.
8. G. P. Agrawal, "Gain Nonlinearities in Semiconductor Lasers: Theory and Application to Distributed Feedback Lasers," *J. Quantum Electron.*, vol. 23, pp. 860-868, 1987.
9. K. Uomi, T. Tsuchiya, M. Aoki, and N. Chinone, "Oscillation Wavelength and Laser Structure Dependence of Nonlinear Damping Effect in Semiconductor Laser," *Appl. Phys. Lett.*, vol. 58, pp. 675-677, 1991.
10. M. P. Kesler, and E. P. Ippen, "Subpicosecond Gain Dynamics in GaAlAs Laser Diodes," *Appl. Phys. Lett.*, vol. 51, pp. 1765-1767, 1987.
11. B. Gomatam, and A. P. DeFonzo, "Theory of Hot Carrier Effects on Nonlinear Gain in GaAs-AlGaAs Lasers and Amplifiers," *J. Quantum Electron.*, vol. 26, pp. 1689-1704, 1990.

12. M. Willatzen, A. Uskov, J. Mørk, H. Olessen, B. Tromborg, and A. -P. Jauho, "Nonlinear Gain Suppression in Semiconductor Lasers due to Carrier Heating," *Photon. Tech. Lett.*, vol. 3, pp. 606-609, 1991.
13. T. Fukushima, R. Nagarajan, J. E. Bowers, R. A. Logan, and T. Tanbun-Ek, "Relative Intensity Noise Reduction in InGaAs/InP Multiple Quantum Well Lasers with Low Nonlinear Damping," *Photon. Tech. Lett.*, vol. 3, pp. 691-693, 1991.
14. C. B. Su, and V. Lanzisera, "Effect of Doping Level on the Gain Constant and Modulation Bandwidth of InGaAsP Semiconductor Lasers," *Appl. Phys. Lett.*, vol. 45, pp. 1302-1304, 1984.
15. W. -H. Cheng, K. -D Buehring, A. Appelbaum, D. Renner, S. Chin, C. B. Su, A. Mar, and J. E. Bowers, "High-Speed and Low-Relative-Intensity Noise 1.3 μm InGaAsP Semi-Insulating Buried Crescent Laser," *J. Quantum Electron.*, vol. 27, pp. 1642-1647, 1991.
16. Y. Arakawa, and A. Yariv, "Quantum Well Lasers-Gain, Spectra, Dynamics," *J. Quantum Electron.*, vol. 22, pp. 1887-1899, 1986.
17. S. W. Corzine, R. H. Yan, and L. A. Coldren, "Theoretical Gain in Strained InGaAs/AlGaAs Quantum Wells Including Valence-Band Mixing Effects," *Appl. Phys. Lett.*, vol. 57, pp. 2835-2837, 1990.
18. I. Suemune, "Theoretical Study of Differential Gain in Strained Quantum Well Structures," *J. Quantum Electron.*, vol. 27, pp. 1149-1159, 1991.
19. L. F. Lester, S. D. Offsey, B. K. Ridley, W. J. Schaff, B. A. Foreman, and L. F. Eastman, "Comparison of the Theoretical and Experimental Differential Gain in Strained Layer InGaAs/GaAs Quantum Well Lasers," *Appl. Phys. Lett.*, vol. 59, pp. 1162-1164, 1991.
20. K. Uomi, T. Mishima, and N. Chinone "Modulation-Doped Multi-Quantum Well (MD-MQ) Lasers. II. Experiment," *Jpn. J. Appl. Phys.*, vol. 29, pp. 88-94, 1990.

21. I. Suemune, L. A. Coldren, M. Yamanishi, and Y. Kan, "Extremely Wide Modulation Bandwidth in a Low Threshold Current Strained Quantum Well Laser," *Appl. Phys. Lett.*, vol. 53, pp. 1378-1380, 1988.
22. R. Nagarajan, T. Fukushima, J. E. Bowers, R. S. Geels, and L. A. Coldren, "High-Speed InGaAs/GaAs Strained Multiple Quantum Well Lasers with Low Damping," *Appl. Phys. Lett.*, vol. 58, pp. 2326-2328, 1991.
23. L. F. Lester, S. S. O'Keefe, W. J. Schaff, and L. F. Eastman, "Multi-quantum Well Strained-Layer Lasers with Improved Low Frequency Response and Very Low Damping," *Electron. Lett.*, vol. 28, pp. 383-385, 1992.
24. H. Lang, H. Hedrich, C. Hoyler, C. Thanner, and H. D. Wolf, "10 GBit/s Direct Modulation of GaAs/AlGaAs Multiple-Quantum-Well Ridge-Waveguide Lasers at Temperatures up to 100 °C," in *Proc. 17th ECOC / 8th IOOC '91*, 1991, p. 205.
25. Y. Hirayama, M. Morinaga, N. Suzuki, and M. Nakamura, "Extremely Reduced Nonlinear K -Factor in High-Speed Strained Layer Multi-quantum Well DFB Lasers," *Electron. Lett.*, vol. 27, pp. 875-876, 1991.
26. L. F. Lealman, M. Bagley, D. M. Cooper, N. Fletcher, M. Harlow, S. D. Perrin, R. H. Walling, and L. D. Westbrook, "Wide Bandwidth Multiple Quantum Well 1.55 μm Lasers," *Electron. Lett.*, vol. 27, pp. 1191-1193, 1991.
27. T. Fukushima, J. E. Bowers, R. A. Logan, T. Tanbun-Ek, and H. Temkin, "Effect of Strain on the Resonant Frequency and Damping Factor in InGaAs/InP Multiple Quantum Well Lasers," *Appl. Phys. Lett.*, vol. 58, pp. 1244-1246, 1991.
28. W. F. Sharfin, J. Schlafer, W. Rideout, B. Elman, R. B. Lauer, J. LaCourse, and F. D. Crawford, "Anomalously High Damping in Strained InGaAs-GaAs Single Quantum Well Laser," *Photon. Tech. Lett.*, vol. 3, pp. 193-195, 1991.
29. R. Nagarajan, T. Fukushima, J. E. Bowers, R. S. Geels, and L. A. Coldren, "Single Quantum Well Strained InGaAs/GaAs Lasers with Large Modulation Bandwidth and Low Damping," *Electron. Lett.*, vol. 27, pp. 1058-1059, 1991.

30. J. Shimizu, H. Yamada, S. Murata, A. Tomita, M. Kitamura, and A. Suzuki, "Optical-Confinement-Factor Dependencies of the K Factor, Differential Gain, and Nonlinear Gain Coefficient for $1.55 \mu\text{m}$ InGaAs/InGaAsP MQW and Strained-MQW Lasers," *Photon. Tech Lett.*, vol. 3, pp. 773-776, 1991.
31. T. Takahashi, and Y. Arakawa, " Nonlinear Gain Effects in Quantum Well, Quantum Well Wire, and Quantum Well Box Lasers," *J. Quantum Electron.*, vol. 27, pp. 1824-1829, 1991.
32. A. Ghiti, and E. P. O'Reilly, "Nonlinear Gain Effects in Strained-Layer Lasers," *Electron. Lett.*, vol. 26, pp. 1978-1980, 1990.
33. K. Uomi, and N. Chinone, "Proposal on Reducing the Damping Constant in Semiconductor Lasers by Using Quantum Well Structures," *Jpn. J. Appl. Phys.*, vol. 28, pp. L1424-L1425, 1989.
34. W. Rideout, W. F. Sharfin, E. S. Koteles, M. O. Vassell, and B. Elman, "Well-Barrier Hole Burning in Quantum Well Lasers," *Photon. Tech. Lett.*, vol. 3, pp. 784-786, 1991.
35. R. Nagarajan, T. Fukushima, S. W. Corzine, and J. E. Bowers, "Effects of Carrier Transport on High-Speed Quantum Well Lasers," *Appl. Phys. Lett.*, vol. 59, pp. 1835-1837, 1991.
36. R. Nagarajan, T. Fukushima, M. Ishikawa, J. E. Bowers, R. S. Geels, and L. A. Coldren, "Transport Limits in High Speed Quantum Well Lasers: Experiment and Theory," *Photon. Tech Lett.*, vol. 4, pp. 121-123, 1992.
37. T. C. Wu, S. C. Kan, D. Vassilovski, K. Y. Lau, C. E. Zah, B. Pathak, and T. P. Lee, "Gain Compression in Tensile-Strained $1.55 \mu\text{m}$ Quantum Well Lasers Operating at First and Second Quantized Levels," *Appl. Phys. Lett.*, vol. 60, pp. 1794-1796, 1992.
38. S. C. Kan, D. Vassilovski, T. C. Wu, and K. Y. Lau, "Quantum Capture and Escape in Quantum-Well Lasers - Implications on Direct Modulation Bandwidth Limitations," *Photon. Tech Lett.*, vol. 4, pp. 428-431, 1992.

39. N. Tessler, R. Nagar, D. Abraham, G. Eisenstein, U. Koren, and G. Raybon, "Coupling Between Barrier and Quantum Well Energy States in a Multiple Quantum Well Optical Amplifier," *Appl. Phys. Lett.*, vol. 60, pp. 665-667, 1992.
40. R. Nagar, N. Tessler, D. Abraham, G. Eisenstein, U. Koren, and G. Raybon, "Measurements of the Barrier-Well Injection Bottleneck in a Multiple Quantum Well Optical Amplifier," *Appl. Phys. Lett.*, vol. 60, pp. 1788-1790, 1992.
41. R. Nagarajan, M. Ishikawa, and J. E. Bowers, "Effects of Carrier Transport on Relative Intensity Noise and Critique of K Factor Prediction of Modulation Response," *Electron. Lett.*, vol. 28, no. 9, pp. 846-847, 1992.
42. M. Ishikawa, T. Fukushima, R. Nagarajan, and J. E. Bowers, "Temperature Dependence of Damping in High Speed Quantum Well Lasers," *Appl. Phys. Lett.*, July 1992.
43. M. Ishikawa, R. Nagarajan, T. Fukushima, J. Wasserbauer, and J. E. Bowers, "Long Wavelength High Speed Semiconductor Lasers with Carrier Transport Effects," *J. Quantum Electron.*, October 1992.
44. R. Nagarajan, R. P. Mirin, T. E. Reynolds, and J. E. Bowers, "Effect of the Confinement Layer Composition on the Internal Quantum Efficiency and Modulation Response of Quantum Well Lasers," *Photon Tech. Lett.*, August 1992.
45. R. Nagarajan, M. Ishikawa, T. Fukushima, R. S. Geels and J. E. Bowers, "High Speed Quantum Well Lasers and Carrier Transport Effects," *J. Quantum Electron.*, 1992.

CHAPTER 2

CARRIER TRANSPORT MODEL

2.1 Transport Across the SCH

Fig. 2.1 shows a typical separate confinement heterostructure (SCH) SQW. Carrier transport and capture in this structure, and the effect of these processes on the modulation response of the laser will be modeled. This is also the structure that is used in the SQW and MQW laser experiments.

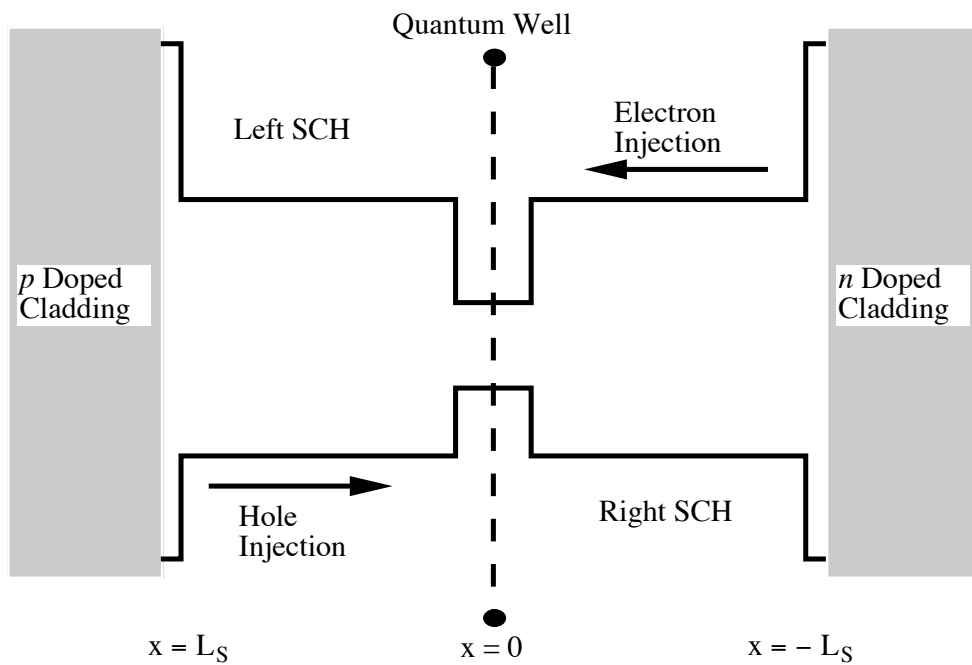


Fig. 2.1 Schematic diagram of a single quantum well laser with a separate confinement heterostructure used in the carrier transport model.

Electron and hole transport from the doped cladding layers to the quantum well consists of two parts [1,2]. First is the transport across the SCH. This is governed by the classical current continuity equations which describe the diffusion, recombination, and, in the presence of any electric field, drift of carriers across the SCH. The second part is the carrier capture by the quantum well. This is a quantum mechanical problem which has to take into account the relevant dynamics of the phonon scattering mechanism which mediates this capture. This scattering process is a function of the initial and final state wavefunctions, the coupling strength of the transition and the phonon dispersion in the material. In this analysis, as shown in Fig. 2.1, the SCH width is the *doping offset* between the quantum well active area and the point from which the claddings are being doped. For carrier transport, it is the width of the undoped region between the quantum well and the cladding layer that is of significance, and in most cases, like ours, it is the width of the SCH.

The next transport mechanism which is significant in devices operating at room temperature is the thermally activated carrier escape from the quantum well or thermionic emission. Although this process is in opposition to carrier capture and degrades the overall carrier capture efficiency of a SQW structure, it is essential for carrier transport between quantum wells in a MQW structure. Another transport process of interest in a MQW system is tunneling between the quantum wells. Thermionic emission is a strong function of barrier height while tunneling is sensitive to both barrier height and width. The barriers in a MQW structure would have to be designed such that the quantum wells efficiently capture and contain the carriers for laser action in a two dimensionally confined system, without adversely sacrificing the transport (leading to carrier trapping) across the structure.

For small-signal modulation experiments, the laser diode is forward biased and a small microwave signal is imposed upon this D.C. bias. The response of the laser is then measured using a high speed photodiode. Since the modulating signal is very small, the device is essentially at constant forward bias. Further, the SCH is not compositionally graded, and this excludes any built-in fields in the SCH to aid carrier transport.

Under normal operation, the semiconductor laser is essentially a forward biased *p-i-n* diode, with the left and right claddings doped *p* and *n* respectively, and the SCH region nominally undoped (Fig. 2.1). In Fig. 2.1, the electrons are injected from the right and the holes from the left, and across the SCH. The important difference is the quantum well in the middle of the SCH where the injected carriers recombine. Although the carrier injection is from the opposite ends of the SCH, any physical separation of the two types of charges across the quantum well layer would lead to very large electric fields between them. The laser normally operates under high forward injection where the carrier density levels are about 10^{18} cm^{-3} , and solving the Poisson equation in one dimension, assuming that the SCH layers on right and left hand side of the quantum well are uniformly pumped with electrons and holes respectively, leads to electric fields in excess of 10^6 V/cm between the carrier distributions. Since the carriers are highly mobile, they would redistribute themselves until the charge neutrality condition is satisfied throughout the SCH. Further, at this level of carrier injection, the unintentional background doping levels are negligible.

This laser structure can then be analyzed like a heavily forward biased *p-i-n* diode [3]. The equations for the electron and hole current densities, including both the drift and diffusion components are given by,

$$J_n = qD_n \left(\frac{qnE}{kT} + \frac{\partial n}{\partial x} \right)$$

$$J_p = qD_p \left(\frac{qpE}{kT} - \frac{\partial p}{\partial x} \right)$$

In this expression we have used the Einstein relation; $\frac{D}{\mu} = \frac{kT}{q}$.

The current continuity conditions are,

$$\frac{\partial n}{\partial t} = \frac{1}{q} \frac{\partial J_n}{\partial x} - U(n, p)$$

$$\frac{\partial p}{\partial t} = -\frac{1}{q} \frac{\partial J_p}{\partial x} - U(n, p)$$

where $U(n, p)$ is the net recombination rate. Assuming high injection conditions, $n \approx p$, and charge neutrality, $\frac{\partial E}{\partial x} = 0$, the above equations can be combined. The electric field term, E , can be eliminated to give the following equation under steady state conditions, i.e. $\frac{\partial n}{\partial t} = \frac{\partial p}{\partial t} = 0$.

$$\frac{d^2 p}{dx^2} - \frac{D_n + D_p}{2D_n D_p} U(p) = 0$$

This simplification does not mean that the dynamic carrier effects have been eliminated from the charge transport equations. The steady state carrier density distribution profile is derived first, and then the small signal response of this distribution is computed to determine the dynamic properties of the device under current modulation. In the above equation, if an ambipolar diffusion coefficient, $D_a = \frac{2D_n D_p}{D_n + D_p}$, is introduced, and if the recombination rate, U , is determined by an ambipolar lifetime, τ_a , then the equation modifies to,

$$\frac{d^2 p}{dx^2} - \frac{p}{L_{ao}^2} = 0$$

where $L_{ao} = \sqrt{D_a \tau_a}$ is the ambipolar diffusion length. In the GaAs system $D_n \gg D_p$, and this leads to an ambipolar diffusion coefficient $D_a \approx 2D_p$. In other words, the carrier transport proceeds as if it is purely diffusion, but with an effective diffusion coefficient which is twice the normal hole diffusion coefficient. Subpicosecond luminescence spectroscopy experiments done in graded and ungraded SCH GaAs/Al_xGa_{1-x}As quantum well structures have revealed evidence for ambipolar transport of carriers in structures similar to the one that we are modeling here [4,5].

2.2 Carrier Distribution in the SCH

The steady state carrier distribution in the SCH region is obtained by solving the ambipolar diffusion equation with appropriate boundary conditions. The general solution to this second order differential equation is,

$$p(x) = C_1 e^{+x/L_{ao}} + C_2 e^{-x/L_{ao}}$$

where C_1 and C_2 are constants to be determined from the relevant boundary conditions. At $x = -L_s$, a constant supply of carriers is established by the D.C. bias current flowing into the SCH. For a D.C. current of I_s , the required boundary condition is,

$$\frac{I_s}{A} = -qD_a \left. \frac{dp}{dx} \right|_{x=-L_s}$$

where A is the cross sectional area of the laser diode. The second boundary condition is that at $x = 0$, i.e. at the position of the quantum well, the carrier density is given by

the steady state carrier density in the well, P_W . The carrier density in the quantum well is determined by the steady state carrier-photon dynamics within the quantum well. This is modeled later using a set of rate equations for the carrier and photon densities.

The coefficients C_1 and C_2 are then,

$$C_1 = \frac{P_W e^{+L_s/L_{ao}} - \frac{I_s L_{ao}}{q D_a A}}{e^{+L_s/L_{ao}} + e^{-L_s/L_{ao}}} \quad C_2 = \frac{P_W e^{-L_s/L_{ao}} + \frac{I_s L_{ao}}{q D_a A}}{e^{+L_s/L_{ao}} + e^{-L_s/L_{ao}}}$$

The current flowing into the quantum well under steady state conditions, I_W , is given by,

$$\begin{aligned} I_W &= -q D_a A \left. \frac{dp}{dx} \right|_{x=0} \\ &= I_s \operatorname{sech} \left(\frac{L_s}{L_{ao}} \right) - q V_W \left(\frac{L_{ao}}{L_W} \right) \tanh \left(\frac{L_s}{L_{ao}} \right) \frac{P_W}{\tau_a} \end{aligned}$$

where V_W is the volume of the quantum well and L_W is the width of the quantum well; $V_W = A L_W$.

2.3 SCH Transport Factor

A differential SCH transport factor, α_{SCH} , analogous to the common base current gain of a bipolar junction transistor (BJT) [6] can be defined,

$$\alpha_{SCH} = \frac{\partial I_W}{\partial I_s} = \operatorname{sech} \left(\frac{L_s}{L_{ao}} \right)$$

The quantity of interest is the small-signal value of α_{SCH} . The expression for this can be derived by substituting L_{ao} by L_a which is given by,

$$L_a = \sqrt{\frac{L_{ao}^2}{1 + j\omega\tau_a}}$$

The small-signal expression simplifies to

$$\alpha_{SCH, \text{small signal}} = \frac{1}{\cosh\left(\left(L_s^2 / D_a \tau_a\right)^{1/2} \sqrt{1 + j\omega\tau_a}\right)} \approx \frac{1}{1 + j\omega \frac{L_s^2}{2D_a}}$$

In the final expression on the right, the width of one side of the SCH has been assumed to be much smaller than the ambipolar diffusion length, i.e. $L_s \ll L_{ao}$ ($= \sqrt{D_a \tau_a}$). This is a valid assumption because the nonradiative lifetime and even the spontaneous recombination lifetime in the SCH layer are of the order of nanoseconds, and are much longer than the SCH layer ambipolar transport time given by, $\tau_r = \frac{L_s^2}{2D_a}$. This is similar to the base layer of a BJT, where the bandwidth limit due to the minority carrier transport time is called the alpha cutoff frequency, and is given by $f_T = \frac{1}{2\pi\tau_r}$. The transport time across the SCH has been directly determined from gain recovery measurements in quantum well optical amplifiers, and has been shown to experimentally vary as the square of SCH width [7,8].

The expression for τ_r , derived above, can also be written as,

$$\tau_r = \frac{L_s^2}{2D_a} = \frac{L_s^2}{2} \left(\frac{D_n + D_p}{2D_n D_p} \right) = \frac{1}{2} \left(\frac{L_s^2}{2D_p} + \frac{L_s^2}{2D_n} \right) = \frac{\tau_{r, \text{holes}} + \tau_{r, \text{electrons}}}{2}$$

This means that the total ambipolar diffusion time can be viewed *as an average* of the individual hole and electron diffusion times. This is a rather useful way of conceptualizing the ambipolar carrier transport in a quantum well structure, and will be used extensively later.

2.4 Ballistic Carrier Transport

Due to the energy step between the cladding and the SCH layer, the carriers that are being injected into the SCH possess excess energy in the direction of their motion. Thus, it may seem that ballistic or *near* ballistic effects, i.e. where only some fraction of the total carriers are traveling ballistically, may be a significant factor in the carrier transport process. This may lead to velocity overshoot effects, and a possible reduction in the carrier transport times. Although these effects are important for some devices, for the following reasons, they do not significantly alter the results of the model presented here.

The cladding is nominally composed of $\text{Al}_{0.6}\text{Ga}_{0.4}\text{As}$. In this material the electrons are confined to the X valley, whereas in the SCH which is typically composed of $\text{Al}_{0.1}\text{Ga}_{0.9}\text{As}$, the electrons are confined to the Γ valley. For laser structures that are grown on [100] oriented substrates, like ones used here, electrons in only one of the three equivalent X valleys of the cladding layer have momentum in the direction of carrier transport across the SCH. Furthermore the longitudinal effective mass in the X valley is 1.9 times the free electron mass, which is about 30 times the effective mass in the Γ valley [9]. Thus, the initial velocity of the electrons in the X valley is small. When the electrons cross into the SCH layer they would have to scatter into the Γ valley. Although at this point they still possess considerable excess energy, the scattering process into the Γ valley makes the momentum distribution of the injected electrons more or less isotropic. This results in a rather small fraction of the hot electrons possessing momentum in the right direction for ballistic transport. This scattering process will also introduce a finite time delay to electron transport. Although the scattering times for X to Γ valley transfer are

complicated, there is an experimental measurement that places the electron scattering time in GaAs from the bottom of the L to Γ valley at around 2 ps [10]. The laser is operating at room temperature, and the smallest SCH width we have experimentally investigated is 700 Å and the largest is 3000 Å. Under these conditions, ballistic electron transport should be negligible for the long SCH devices, and may be present in the short SCH ones. Even for short SCH devices, ballistic transport of electrons would not alter the final result, because the real limit to the high speed performance of these devices is hole and not electron transport. Furthermore, at the high carrier densities encountered in lasers, the electron-electron scattering times are very short, and this would adversely affect ballistic transport. Using 100 fs optical pulses in a pump-probe type differential absorption measurement, carrier thermalization times less 10 fs in GaAs quantum wells have been inferred from the experimental results using a relaxation time approximation model [11]. More recently, direct measurement of this carrier thermalization time in bulk GaAs has been done using 9 fs wide optical pulses. By analyzing the polarization rotation of linearly polarized probe pulses, redistribution of carrier momentum has been measured to occur at times faster than 25 fs at carrier densities larger than $8 \times 10^{17} \text{ cm}^{-3}$ [12].

Any ballistic transport of holes on the other hand could in principle influence the results of our model. Due to their much larger mass and a lower valence band discontinuity in this material system and therefore lesser excess energy, and in the presence of high injected carrier densities, the holes would thermalize quickly on crossing into the SCH. Thus for the wide SCH devices, near ballistic or hot carrier effects of holes are not significant *at room temperature*, especially over a distance of 3000 Å. For the short SCH devices this again may not pose a problem, because we

believe that in our present structures the RC parasitic and device heating limits are lower than the carrier transport limit.

2.5 Carrier Capture Time of the Quantum Well

Calculating the carrier capture time by the quantum well involves the computation of the probability per unit time that a carrier in some initial state in the SCH emits a longitudinal optical (LO) phonon, and ends up in some final state within the quantum well as dictated by energy and momentum conservation conditions. Early theoretical works based on semi-classical treatment argued that the quantum well width had to be of the order of or larger than the LO phonon scattering limited electron mean free path ($\approx 100 \text{ \AA}$) for the quantum well to efficiently capture carriers, and act as a center for radiative recombination [13,14].

More recent quantum mechanical calculations have relaxed this condition, but have predicted strong oscillations in the capture time as a function of the quantum well width. As the well width increases, first the states within the quantum well become more tightly bound, and secondly the virtual states above the quantum well become bound to the well. These result in the final energy states within the quantum well moving in and out of the reach of any state in the SCH separated by a phonon energy, from which a carrier can scatter [15,16,17]. Theoretically calculated capture times in SQW structures have been found to oscillate between 10 ps and 1 ns for quantum wells with an ungraded SCH [15], and between 20 ps and 200 ps for quantum wells with a linearly graded SCH [16].

Recently, calculations done for MQW structures have predicted carrier capture times in the range of 1 ps, closer to the experimentally observed values [18].

This calculation is an adaptation of the previous one for the SQW structure. The difference is that the increase in the number of wells results in an increase in the total number of final states to which carrier may scatter, and a corresponding decrease in the capture time. The capture time has in fact been calculated to be nearly inversely proportional to the number of wells with all other structural parameters held constant [18]. As previously, the capture time is a function of the quantum well width, and in addition it is also sensitive to the choice of the SCH width (also applicable to the SQW case), barrier width and barrier height.

Experimentally the carrier capture times have been measured by subpicosecond luminescence up-conversion spectroscopy [2,19,20]. Using this technique the time resolved barrier and quantum well luminescence are measured, and the effective electron and hole capture times are extracted from these measurements. Since the luminescence intensity is proportional to both the number of electrons and holes, the barrier luminescence is expected to decay with the faster of the two effective capture times and quantum well luminescence is expected to rise with the slower of the two [19]. The rise in the quantum well luminescence is not only influenced by the carrier transfer from the barrier layers but also by the carrier relaxation time within the quantum wells. This introduces additional complications to the interpretation of the quantum well luminescence rise time [20]. The quantum mechanical calculations indicate that the hole capture times are smaller than the electron capture times because of their larger effective mass [15-18]. Faster hole capture times have been directly measured in experimental setups where it has been possible to distinguish between the two carrier types [20].

The experimentally measured effective capture times are tabulated below

Reference	Material System	Hole Capture Time (ps)	Electron Capture Time (ps)
19	InGaAs/InP	< 0.3	< 1.0
2	GaAs/AlGaAs	≈ 0.65	≈ 1.2
20	InGaAs/InP	≈ 0.2	≈ 0.8

One important aspect of the experimental results is that the capture times are independent of quantum well width in all the cases reviewed above. This is in contrast to all the theoretical work that has been reported to date. The dispersion of the LO phonons were neglected in these calculations, and it has been speculated that the resonances resulting from the variations in the confined phonon modes, as a function of well width, could eventually modify these theoretical results [2].

2.6 Effects of a Graded SCH Layer on Carrier Transport

The use of a linearly or parabolically graded index (L-GRIN or P-GRIN) SCH layer has been experimentally shown to enhance the carrier collection efficiency of the quantum well [1,2]. In the GaAs/Al_xGa_{1-x}As system, this grading is achieved during crystal growth by continually varying the Al mole fraction, x , to introduce a quasi-electric field within the SCH. At low temperatures (6 K), quantum wells with the L-GRINSCH have been shown to exhibit almost 100% collection efficiency while those with an ungraded SCH only about 50% [1]. Time resolved photoluminescence experiments have shown that the decay time of the luminescence from a L-GRINSCH (2 ps) can be as much as 11 times faster than the ungraded SCH (22 ps) luminescence at low temperatures (80K) [2]. The performance of the P-GRINSCH quantum well is

in between these two limits, probably due to the electric field going to zero at the quantum well interface.

At low temperatures, the main transport limit in the L-GRINSCH is the carrier capture by the quantum well. At room temperature the drift time in the L-GRINSCH becomes important compared to the quantum well capture time. This is in contrast to the ungraded SCH where the variation in transport time is essentially due to the variation of mobility with temperature. Thus at room temperature the L-GRINSCH has been predicted to be only twice as fast as the ungraded SCH [2]. This would not lead to any improvement in the high speed performance of L-GRINSCH lasers because the width of the L-GRINSCH needed to maximize the optical confinement factor is about twice that for an ungraded SCH, and for any shorter widths the confinement factor decreases rather rapidly. Further, some recent experiments, in contrast to the previous ones, have determined that the gain recovery times, which are a measure of the carrier transport/dwell times in the SCH, in L-GRINSCH (≈ 14 ps) quantum well optical amplifiers are actually about 3 to 4 times larger than in ones with ungraded SCH (≈ 4 ps) of comparable width [8]. Thus, at room temperature there may not be any advantage in using a L-GRINSCH for the design of a high speed quantum well laser.

2.7 Thermionic Emission

Assuming that the carriers in the barriers have bulk-like properties and obey Boltzmann statistics, the thermionic emission lifetime, τ_e , from a quantum well is [21],

$$\tau_e = \left(\frac{2\pi m^* L_W^2}{k T} \right)^{1/2} \exp\left(\frac{E_B}{k T} \right)$$

where E_B is the effective barrier height, m^* is the carrier mass, k is the Boltzmann constant and T is temperature in K. Thermionic emission is a sensitive function of barrier height and temperature.

2.8 Tunneling

In a MQW structure there are a number of wells each separated by barriers of energy height, E_B , and thickness, L_b . In this case the electron and hole wavefunctions are no longer completely localized within the individual quantum wells, and for any finite L_b there will be coupling between the wells. For a system of two symmetric wells, the inter-well coupling would remove the energy degeneracy that exists in the limit of infinite L_b . The lowest odd (E_1) and even (E_2) bound states of such a two well system are separated by some small energy, $\Delta E = E_1 - E_2$ ($E_1 > E_2$) [22,23]. The overall linear superposition wavefunction of this system corresponds to an electron or a hole oscillating between the wells at a frequency given by $\frac{\Delta E}{\hbar}$ where h is the Planck constant. The tunneling time, defined as the one half period of the oscillation, is given by

$$\tau_t = \frac{h}{2\Delta E}$$

Although this result has been derived for a two well system, it will generally be true for a MQW system in the limit of weak inter-well coupling [22].

2.9 Multiple Quantum Well Structure

There are additional complications due to carrier transport between the various wells in the MQW system. Again charge neutrality is assumed to hold in the entire intrinsic SCH region, and holes dominate the carrier dynamics. The analyses

for carrier transport across the SCH and capture by the first quantum well is the same as for the SQW case.

Due to their very small capture time we can assume that all the holes are captured by the first quantum well, and subsequent transport across the MQW structure is either via thermionic emission, then diffusion across the barrier and capture by the next quantum well or tunneling through the barrier. For a well designed barrier, the subsequent diffusion and capture times are negligible compared to the initial thermionic emission time. Thermionic emission and tunneling are competing processes, and the faster one will dominate. If a barrier transport time, τ_b , is defined, then

$$\frac{1}{\tau_b} = \frac{1}{\tau_e} + \frac{1}{\tau_t}$$

The barrier transport time, τ_b , corresponding to the electrons and holes will be different. Since the ambipolar transport times can be viewed *as an average* of the respective hole and electron transport times, a quantity called the effective barrier transport time can be defined as follows:

$$\tau_c = \frac{\tau_{b,holes} + \tau_{b,electrons}}{2}$$

Fig. 2.2 shows the variation of the carrier transport times, at room temperature, for different barrier thicknesses for an $\text{In}_{0.2}\text{Ga}_{0.8}\text{As}$ quantum well and a GaAs barrier. For sufficiently small widths ($< 50 \text{ \AA}$) tunneling dominates the carrier transport across the barriers. For intermediate structures, hole transport is mainly by thermionic emission while tunneling dominates electron transport. For thick barriers, the experimental tunneling times are somewhat larger than the calculated ones because the scattering in

the barriers makes the tunneling process incoherent [24]. This does not effect our model as thermionic emission and subsequent diffusion across the barriers dominate both electron and hole transport in this regime. The slope of the electron and hole transport times decreases for wide barriers, and this apparent saturation is due to the fact that the diffusion time is still a small part of the total transport time across the barrier. For very wide barriers, the diffusion time across the barrier dominates over the thermionic emission time, which is independent of the barrier width.

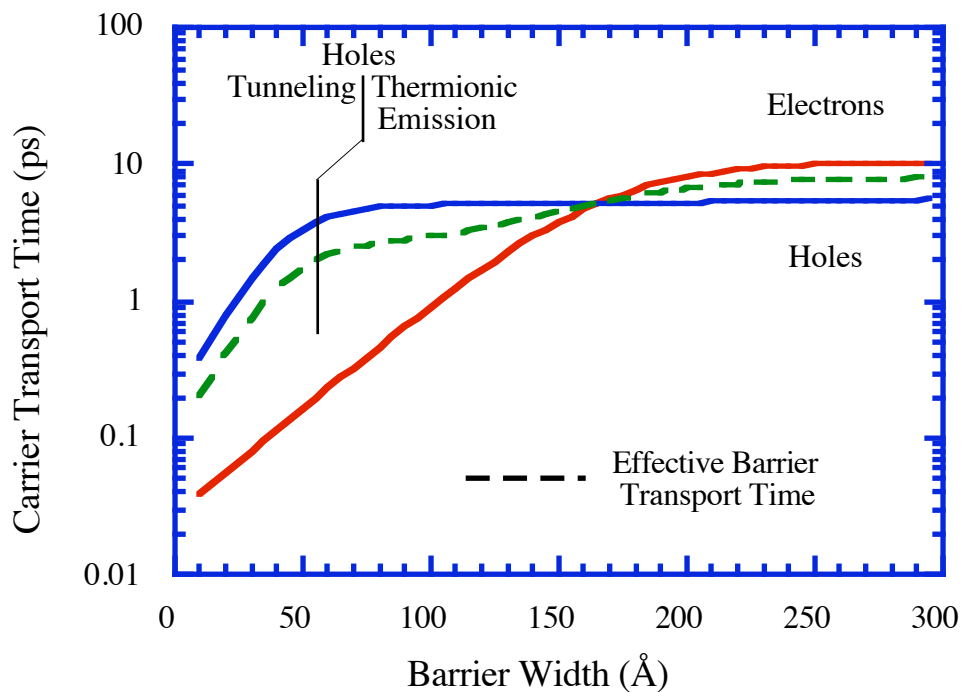


Fig. 2.2 Variation of the electron and hole transport times between two 80 Å $\text{In}_{0.2}\text{Ga}_{0.8}\text{As}$ quantum wells with barrier thickness, for a GaAs barrier. The effective transport time is the average of the individual transport times.

2.10 Effect of Interface Recombination

Nonradiative recombination centers formed by defects and traps can have a significant effect on the carrier injection process in semiconductor lasers. These defects

are normally formed at the interfaces between the various epitaxial layers, or exposed surfaces like the cleaved facets and etched layers. Advanced crystal growth techniques these days have managed to dramatically reduce the formation of defects at epitaxial heterointerfaces, even in the case of lattice mismatched layers (below the critical layer thickness) where the strain can be accommodated via lattice deformation.

The current component due to interface recombination J_{int} is written as [25],

$$J_{\text{int}} = q S_i A n$$

where A is the surface area of the interface, n is the carrier density at the interface and S_i is the interface recombination velocity. The interface recombination velocity can be written in terms of more fundamental parameters [26],

$$S_i = \sigma_a v_{\text{th}} N_{\text{st}}$$

where σ_a is the carrier capture cross-section of the defect, v_{th} is the carrier thermal velocity and N_{st} is the per unit area density of surface defects. The surface recombination velocity, for exposed surfaces like cleaved facets, is about 10^7 cm/s for GaAs which is two orders of magnitude larger than for exposed InP surfaces. Surface passivation techniques, like dielectric coatings, are generally employed to reduce the surface recombination velocity [25].

The most significant effect of interface recombination is the increase in the threshold current by J_{int} , and the reduction in the internal quantum efficiency (Chapter four). The experimentally measured threshold current density and internal quantum efficiency of all the wafers used in the modulation experiments here have been listed in Appendix B. Given the low threshold current density and the high internal quantum efficiency of these samples, it can be concluded that the epitaxial

layers are of high quality, and the incidence of defect formation and carrier recombination at the heterointerfaces is minimal.

Dynamic properties of the lasers will not be *directly* affected, at least in the case of small signal carrier density variations. Since J_{int} is proportional to the carrier density and significant variation in carrier density does not occur above threshold, the interface recombination mainly affects the static properties of the high speed laser. The degradation of the static properties may *indirectly* affect the dynamic properties of the laser. The increase in the threshold current and the decrease in the internal quantum efficiency means that a larger bias current is required to obtain a given optical power output. This will result in increased levels of device heating for the same photon density, and, hence, lead to a degradation of the high speed properties of the laser.

2.11 Analysis of Laser Dynamics

The various carrier transport times derived here are central to the analysis of the modulation dynamics in quantum well lasers. These lifetimes will be incorporated into the laser rate equations for the carrier and photon densities to form the complete dynamic model.

In the conventional rate equations, the input current directly modulates the carrier density in the active region [27-30]. In the present analysis the input current supplies the carrier reservoir in the SCH, which in turn feeds the quantum well active region. The carrier transport time across the SCH determines the maximum rate at which the quantum well can be pumped. This carrier feed rate will then set the upper limit to the speed at which the quantum well may be modulated, irrespective of the rate of variation of the modulating signal applied at the terminals of the laser diode.

The thermionic emission is a carrier loss process from the quantum well that competes directly with the carrier pump process. The thermionic emission rate must be significantly smaller than the carrier capture rate for the quantum well active area to be efficiently modulated. In an MQW laser, the effective barrier transport time will determine if all the quantum wells in the structure can be efficiently modulated without significant variation in the carrier population of the individual wells.

In Chapter three, the complete rate equation formulation of the laser dynamics, including the carrier transport effects is presented. Small-signal analytic solution to the rate equations is derived, and the effects of carrier transport on the modulation response of quantum well lasers are discussed. Further, extensive set experimental evidence is presented in support of the dynamic model.

References

1. H. -J. Pollard, K. Leo, K. Rother, K. Ploog, J. Feldman, G. Peter, and E. O. Göbel, "Trapping of Carriers in Single Quantum Wells with Different Configuration of the Confinement Layers," *Phys. Rev.*, vol. B 38, pp. 7635-7648, 1988.
2. S. Morin, B. Deveaud, F. Clerot, K. Fujiwara, and K. Mitsunaga, "Capture of Photoexcited Carriers in a Single Quantum Well with Different Confinement Structures," *J. Quantum Electron.*, vol. 27, pp. 1669-1675, 1991.
3. N. R. Howard, and G. W. Johnson, " P^+IN^+ Silicon Diodes at High Forward Current Densities," *Solid State Electron.*, vol. 8, pp. 275-284, 1965.
4. B. Deveaud, J. Shah, and T. C. Damen, "Bloch Transport of Electrons and Holes in Superlattice Minibands: Direct Measurement by Subpicosecond Luminescence Spectroscopy," *Phys. Rev Lett.*, vol. 58, pp. 2582-2585, 1987.
5. P. W. M. Blom, R. F. Mols, J. E. M. Haverkort, M. R. Ley, and J. H. Wolter, "Measurement of the Ambipolar Carrier Capture Time in a GaAs/ $Al_xGa_{1-x}As$ Separate Confinement Heterostructure Quantum Well," *Superlattice Microstructure*, vol. 7, pp. 319-321, 1990.
6. S. M. Sze, *Physics of Semiconductor Devices*, 2nd ed. New York:Wiley, 1981, pp. 159.
7. G. Eisenstein, J. M. Wiesenfeld, M. Wegener, G. Sucha, D. S. Chemla, S. Weiss, G. Raybon, and U. Koren, "Ultrafast Gain Dynamics in 1.5 μm Multiple Quantum Well Optical Amplifiers," *Appl. Phys. Lett.*, vol. 58, pp. 158-160, 1991.
8. S. Weiss, J. M. Wiesenfeld, D. S. Chemla, G. Raybon, G. Sucha, M. Wegener, G. Eisenstein, C. A. Burrus, A. G. Dentai, U. Koren, B. I. Miller, H. Temkin, R. A. Logan, and T. Tanbun-Ek, "Carrier Capture Times in 1.5 μm Multiple Quantum Well Optical Amplifiers," *Appl. Phys. Lett.*, vol. 60, pp. 9-11, 1992.

9. J. S. Blakemore, "Semiconducting and other Major Properties of Gallium Arsenide," *J. Appl. Phys.*, vol. 53, pp. R123-R181, 1982.
10. J. Shah, B. Deveaud, T. C. Damen, W. T. Tsang, A. C. Gossard, and P. Lugli, "Determination of Intervalley Scattering Rates in GaAs by Subpicosecond Luminescence Spectroscopy," *Phys. Rev Lett.*, vol. 59, pp. 2222-2225, 1987.
11. W. H. Knox, D. S. Chemla, G. Livescu, J. E. Cunningham, and J. E. Henry, "Femtosecond Carrier Thermalization in Dense Fermi Seas," *Phys. Rev Lett.*, vol. 61, pp. 1290-1293, 1988.
12. M. T. Portella, J.-Y. Bigot, R. W. Schenlein, J. E. Cunningham, and C. V. Shank, "*k*-Space Carrier Dynamics in GaAs," *Appl. Phys. Lett.*, vol. 60, pp. 2123-2125, 1992.
13. M. Shichijo, R. M. Kolbas, N. Holonyak, Jr., R. D. Dupuis, and P. D. Dapkus, "Carrier Collection in a Semiconductor Quantum Well," *Solid State Comm.*, vol. 27, pp. 1029-1032, 1978.
14. J. Y. Tang, K. Hess, N. Holonyak, Jr., J. J. Coleman, and P. D. Dapkus, "The Dynamics of Electron-Hole Collection in Quantum Well Heterostructures," *J. Appl. Phys.*, vol. 53, pp. 6043-6046, 1982.
15. J. A. Brum, and G. Bastard, "Resonant Carrier Capture by Semiconductor Quantum Wells," *Phys. Rev.*, vol. B 33, pp. 1420-1423, 1986.
16. J. A. Brum, T. Weil, J. Nagle, and B. Vinter, "Calculation of Carrier Capture Time of a Quantum Well in Graded-Index Separate-Confinement Heterostructures," *Phys. Rev.*, vol. B 34, pp. 2381-2384, 1986.
17. M. Babiker, and B. K. Ridley, "Effective-Mass Eigenfunction in Superlattices and their Role in Well-Capture," *Superlattice Microstructure*, vol. 2, pp. 287-291, 1986.

18. P. W. M. Blom, J. E. M. Haverkort, and J. H. Wolter, "Optimization of Barrier Thickness for Efficient Carrier Capture in Graded-Index and Separate-Confinement Multiple Quantum Well Lasers," *Appl. Phys. Lett.*, vol. 58, pp. 2767-2769, 1991.
19. B. Deveaud, J. Shah, T. C. Damen, and W. T. Tsang, "Capture of Electrons and Holes in Quantum Wells," *Appl. Phys. Lett.*, vol. 52, pp. 1886-1888, 1988.
20. R. Kersting, R. Schwedler, K. Leo, and H. Kruz, "Ultrafast Carrier Transport and capture in InGaAs/InP Heterostructures," *Proc. 4th Int. Conf. Indium Phosphide and Related Materials*, paper THP19, 1992, pp. 565.
21. H. Schneider, and K. v. Klitzing, "Thermionic Emission and Gaussian Transport of Holes in a GaAs/Al_xGa_{1-x}As Multiple-Quantum-Well Structure," *Phys. Rev.*, vol. B 38, pp. 6160-6165, 1988.
22. H. Kroemer, and H. Okamoto, "Some Design Considerations for Multi-Quantum-Well Lasers," *Jpn. J. Appl. Phys.*, vol. 23, pp. 970-974, 1984.
23. G. Bastard, *Wave Mechanics Applied to Semiconductor Heterostructures*, New York:Wiley, 1988, pp. 14.
24. K. Leo, J. Shah, J. P. Gordon, T. C. Damen, D. A. B. Miller, C. W. Tu, and J. E. Cunningham, "Effect of Collisions and Relaxation on Coherent Resonant Tunneling: Hole Tunneling in GaAs/Al_xGa_{1-x}As Double-Quantum-Well Structures," *Phys. Rev.*, vol. B 42, pp. 7065-7068, 1990.
25. G. P. Agrawal, and N. K. Dutta, *Long Wavelength Semiconductor Lasers*, New York:Van Nostrand Reinhold, 1986, pp. 449, 183.
26. S. M. Sze, *Physics of Semiconductor Devices*, 2nd ed. New York:Wiley, 1981, pp. 57.
27. R. S. Tucker, "High-Speed Modulation of Semiconductor Lasers," *J. Lightwave Technol.*, vol. 21, pp. 1180-1192, 1985.

28. K. Y. Lau, and A. Yariv, "Ultra-High Speed Semiconductor Lasers," *J. Quantum Electron.*, vol. 21, pp. 121-138, 1985.
29. J. E. Bowers, B. R. Hemenway, A. H. Gnauck, and D. P. Wilt, "High-Speed InGaAsP Constricted-Mesa Lasers," *J. Quantum Electron.*, vol. 22, pp. 833-844, 1986.
30. R. Olshansky, P. Hill, V. Lanzisera, and W. Powazinik, "Frequency Response of 1.3 μm InGaAsP High Speed Semiconductor Lasers," *J. Quantum Electron.*, vol. 23, pp. 1410-1418, 1987.

CHAPTER 3

RATE EQUATION ANALYSIS

3.1 Rate Equations

Rate equations are used to describe the carrier density dynamics in the quantum well and the SCH layer, and photon density dynamics in the laser cavity, for both the SQW and MQW lasers. A small-signal solution of the rate equations gives the modulation response or the relative intensity noise spectrum depending on the nature of the driving force. Complete analytical solutions are done only for the SQW case, while the MQW case is analyzed using a numerical model.

The rate equations for the carrier density in the quantum well (P_W) and the SCH layer (P_B) and the photon density in the cavity (S) are written as,

$$\begin{aligned}\frac{dP_B}{dt} &= \frac{I}{q V_{SCH}} - \frac{P_B}{\tau_r} + \frac{P_W(V_W / V_{SCH})}{\tau_e} \\ \frac{dP_W}{dt} &= \frac{P_B(V_{SCH} / V_W)}{\tau_r} - \frac{P_W}{\tau_n} - \frac{P_W}{\tau_e} - \frac{v_g G(P) S}{1 + \epsilon S} \\ \frac{dS}{dt} &= \frac{\Gamma v_g G(P) S}{1 + \epsilon S} - \frac{S}{\tau_p}\end{aligned}$$

where τ_n is the bimolecular recombination lifetime, τ_p is the photon lifetime, Γ is the optical confinement factor, $G(P)$ is the carrier density dependent gain, v_g is the mode velocity, ϵ is the gain compression factor, V_W is the volume of the quantum well, and V_{SCH} is the volume of the SCH. We have neglected the spontaneous emission feedback term because it does not have a significant effect on the modulation

response. Two independent equations for the carrier density in the SCH may be used; one for the layer to the right of the quantum well and the other for the layer to the left. The final results are not altered in any way if only one equation is used for the carrier density in the barrier [1]. The optical gain $G(P)$ is a function of both the electron and hole carrier density within the quantum well. Since charge neutrality has been assumed, the electron and hole densities are equal to one another in the quantum well. We have ignored carrier recombination in the SCH layer.

In the rate equations, the terms with τ_e represent the loss of carriers from the quantum well and the gain by the SCH layer, and the terms with τ_r vice versa. The finite capture time of the quantum well is small (< 1 ps) for the holes which primarily contribute to the magnitude of τ_r (see Chapter 2). The X to Γ valley scattering time would contribute to the total electron transport time, but even with this addition hole diffusion would dominate, except for very small SCH widths, and this does not affect the expression for τ_r again. The carriers in the quantum well are two dimensionally confined and the ones in the SCH layer have bulk-like properties. The rate equations have been written in terms of volume carrier densities. The volume ratios V_{SCH}/V_W and V_W/V_{SCH} have been used in the rate equations to account for the fact that P_B and P_W are normalized with respect to two different volumes.

The small-signal solution of the equations is done by first making the following substitution: $I = I_o + i e^{j\omega t}$, $P_B = P_{Bo} + p_B e^{j\omega t}$, $P_W = P_{Wo} + p_W e^{j\omega t}$, $S = S_o + s e^{j\omega t}$ and $G = G_o + g_o p_W e^{j\omega t}$. Although $G(P)$ is a sublinear function of the carrier density, it can always be linearized about some steady state operating point, where g_o is the differential gain at that steady state carrier density. For the small-signal carrier density variation, p_W , g_o is a constant because the steady state carrier density in the

quantum well is clamped at the steady state value of P_{W_0} . The g_0 value is then different for different values of P_{W_0} , and this accounts for the saturation of gain at high carrier densities in quantum well lasers.

3.2 Modulation Response

After the small-signal quantities are substituted into the rate equations, the steady-state quantities are set to zero. The resulting small-signal equations are [2,3],

$$\begin{aligned}
 j \omega p_B &= \frac{i}{q V_{SCH}} - \frac{p_B}{\tau_r} + \frac{p_W (V_W / V_{SCH})}{\tau_e} \\
 j \omega p_W &= \frac{p_B (V_{SCH} / V_W)}{\tau_r} - \frac{p_W}{\tau_n} - \frac{p_W}{\tau_e} - \frac{v_g g_0 S_0}{1 + \epsilon S_0} p_W - \frac{v_g G_0}{(1 + \epsilon S_0)^2} s \\
 j \omega s &= \frac{\Gamma v_g g_0 S_0}{1 + \epsilon S_0} p_W + \frac{s}{\tau_p (1 + \epsilon S_0)} - \frac{s}{\tau_p}
 \end{aligned}$$

The steady-state solution to the photon density equation gives the basic gain-loss relationship in the laser cavity; $\frac{\Gamma v_g G_0}{1 + \epsilon S_0} = \frac{1}{\tau_p}$. This set of small-signal equations can be reduced by eliminating p_B and p_W to give a relationship between the modulating current, i , and the optical output, s . The modulation response is given by $|M(\omega)|$, where $M(\omega) = \frac{s(\omega)}{i}$. The complete $M(\omega)$ function is [3],

$$M(\omega) = \left(\frac{\Gamma v_g g_0 S_0}{q V_W} \right) \frac{1}{A_0 + j A_1 \omega - A_2 \omega^2 - j A_3 \omega^3}$$

where the denominator terms are given by,

$$\begin{aligned}
A_0 &= \frac{v_g g_o S_o}{\tau_p} \left(1 + \frac{\varepsilon}{v_g g_o \tau_n} \right) \\
A_1 &= v_g g_o S_o \left(1 + \frac{\tau_r}{\tau_p} \right) + \frac{\varepsilon S_o}{\tau_p} \left(1 + \frac{\tau_r}{\tau_e} + \frac{\tau_r}{\tau_n} \right) + \frac{1}{\tau_n} (1 + \varepsilon S_o) \\
A_2 &= (1 + \varepsilon S_o) \left(1 + \frac{\tau_r}{\tau_e} + \frac{\tau_r}{\tau_n} \right) + v_g g_o S_o \tau_r + \frac{\varepsilon S_o \tau_r}{\tau_p} \\
A_3 &= \tau_r (1 + \varepsilon S_o)
\end{aligned}$$

The denominator of the exact expression is a third order polynomial, and can be solved numerically. The exact expression for $M(\omega)$ can be rewritten as [2,4,5],

$$M(\omega) = \left(\frac{1}{1 + j \omega \tau_r} \right) \times \frac{\frac{\Gamma v_g g_o S_o}{q V_w}}{\left(j \omega \left(1 + \left[\frac{\tau_r}{1 + j \omega \tau_r} \right] \frac{1}{\tau_e} \right) + \frac{v_g g_o S_o}{1 + \varepsilon S_o} \right) \left(j \omega (1 + \varepsilon S_o) + \frac{\varepsilon S_o}{\tau_p} \right) + \frac{v_g g_o S_o}{\tau_p (1 + \varepsilon S_o)}}$$

$M(\omega)$ can be simplified by neglecting the frequency dependence of τ_r , i.e. by replacing the term within the square brackets in the denominator by τ_r . With this replacement $M(\omega)$ is written as;

$$M(\omega) = \left(\frac{1}{1 + j \omega \tau_r} \right) \frac{A}{\omega_r^2 - \omega^2 + j \omega \gamma}$$

The expressions for A , ω_r^2 and γ are,

$$\begin{aligned}
A &= \frac{\Gamma (v_g g_o / \chi) S_o}{q V_W (1 + \varepsilon S_o)} \\
\omega_r^2 &= \frac{(v_g g_o / \chi) S_o}{\tau_p (1 + \varepsilon S_o)} \left(1 + \frac{\varepsilon}{v_g g_o \tau_n} \right) \\
\gamma &= \frac{(v_g g_o / \chi) S_o}{(1 + \varepsilon S_o)} + \frac{\varepsilon S_o / \tau_p}{(1 + \varepsilon S_o)} + \frac{1}{\chi \tau_n}
\end{aligned}$$

where a transport factor, $\chi = 1 + \frac{\tau_r}{\tau_e}$, has been introduced into the equations. The original expressions for γ and ω_r^2 are recoverable in the limit of $\chi = 1$, i.e. in the limit of short transport time across the SCH [6].

From these analytic expressions a relationship for the K factor can be derived. The K factor was originally defined as, $\gamma = Kf_r^2$ [7]. However, experimentally, a D.C. offset is always observed, and therefore a better definition is $\gamma = Kf_r^2 + \gamma_o$ [1]. From this definition,

$$\begin{aligned}
K &= 4 \pi^2 \left(\tau_p + \frac{\varepsilon}{(v_g g_o / \chi)} \right) \\
\gamma_o &= \frac{1}{\chi \tau_n}
\end{aligned}$$

Therefore, depending on the laser structure, the K factor can be significantly affected by transport.

Fig. 3.1 compares the modulation response computed using the analytic and the exact solutions for the case of the widest SCH devices used in the experiments [1]. The agreement is good, and more evidence will be presented later to show that the analytic solutions are in fact valid.

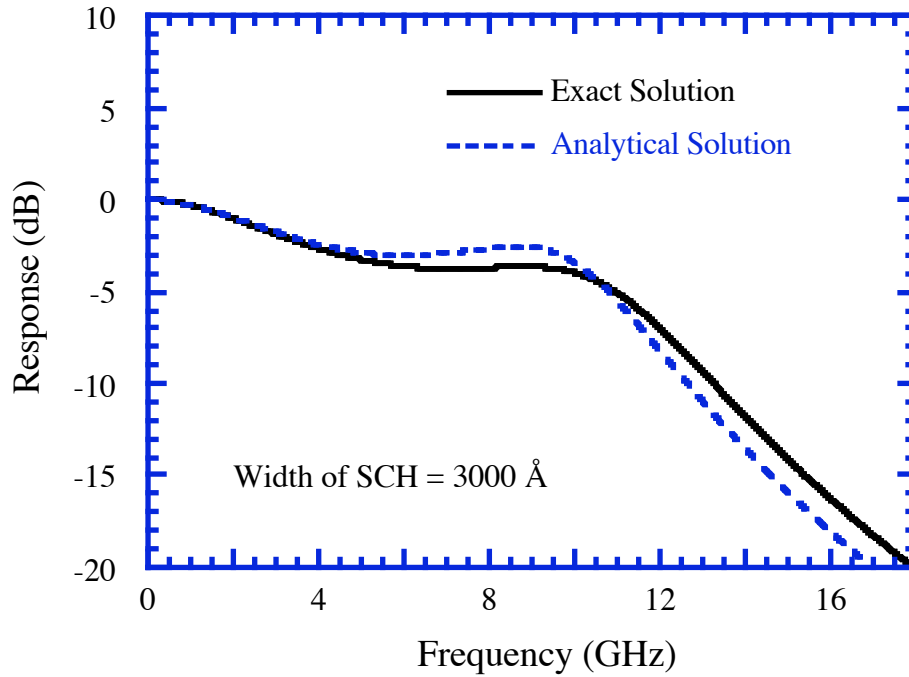


Fig. 3.1 Comparison of the exact and analytical solutions to the modulation response for an 80 Å $\text{In}_{0.2}\text{Ga}_{0.8}\text{As}$ SQW laser with 300 μm cavity length at 40 mW of output power. The modulation response has been normalized with respect to $\text{IM}(0)$.

From these analytic expressions a number of effects of transport are evident.

1.	The low frequency rolloff in the modulation response is <i>only</i> due to the transport time across the SCH [1,2,8,9]. This is a parasitic-like rolloff which would significantly limit the - 3 dB modulation bandwidth for large τ_r , and is <i>indistinguishable</i> from parasitics.
2.	The effective differential gain has been reduced to g_o/χ . This reduction is <i>not</i> responsible for the rolloff in (1) above, and is present even in the absence of a significant rolloff. This results in the reduction of the resonance frequency [1].

3.	The effective bimolecular recombination lifetime has been increased to $\chi\tau_n$. This leads to a structure dependence of γ_o [1].
4.	The gain compression factor remains unmodified [1]. This is in contrast to Reference [8] where a well barrier holeburning model has been used to explain the degradation of K factor via an enhancement in ϵ .

The low frequency rolloff caused by transport means that the maximum possible - 3 dB modulation bandwidth in a laser is not given by, $f_{\max} = \sqrt{2} \frac{2\pi}{K}$. The K factor is an upper limit to the modulation bandwidth. In the presence of severe low frequency rolloff due to carrier transport across the SCH, the transport determines the *intrinsic* limit to the maximum modulation bandwidth.

3.3 Experimental Results - Effect of varying τ_r

Lasers were fabricated from three SQW samples with different SCH widths; Sample A with 760 Å wide SCH, Sample B with 1500 Å wide SCH and Sample C with 3000 Å wide SCH, to investigate the effects of varying the transport time, τ_r , on the modulation response. Figures 3.2 (a) and 3.3 (a) show the experimental C.W. modulation response of Samples A and C. The samples both have 300 μm long cavities and 2.5 μm wide ridges. Although the devices are identical except for the SCH width, the modulation response of Sample C with the widest SCH region is completely damped at about half the output power level of Sample A, and the bandwidth of Sample A is six times that of Sample C at higher power levels. The maximum C.W. modulation bandwidth for Sample A is 18.1 GHz, which is the largest reported to date in SQW lasers.

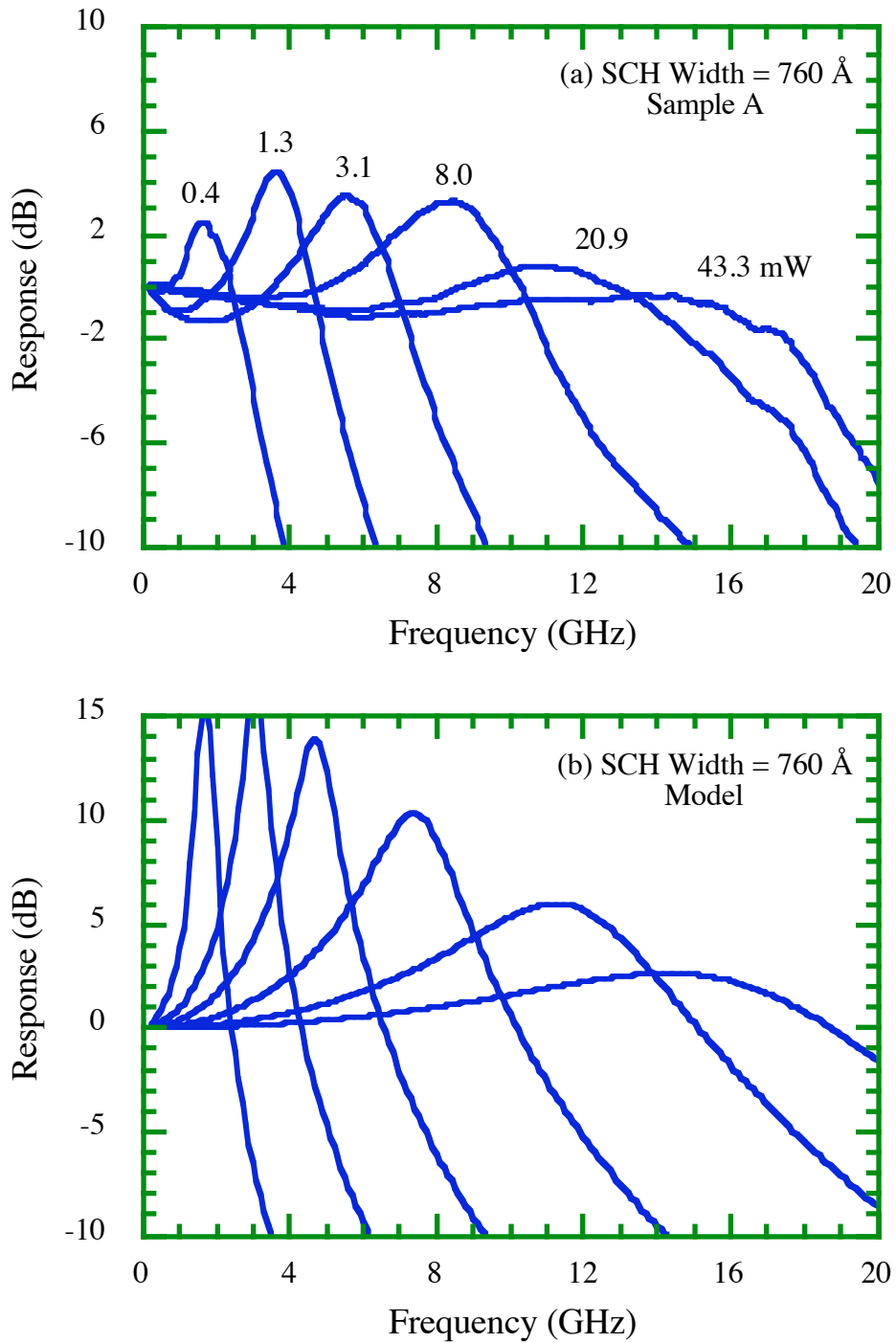


Fig. 3.2 (a) C.W. modulation response for the narrow SCH Sample A, compared to the results from the model in (b). The overestimation in the peak of the response at low power levels is due to the omission of the spontaneous emission feedback factor in the model.

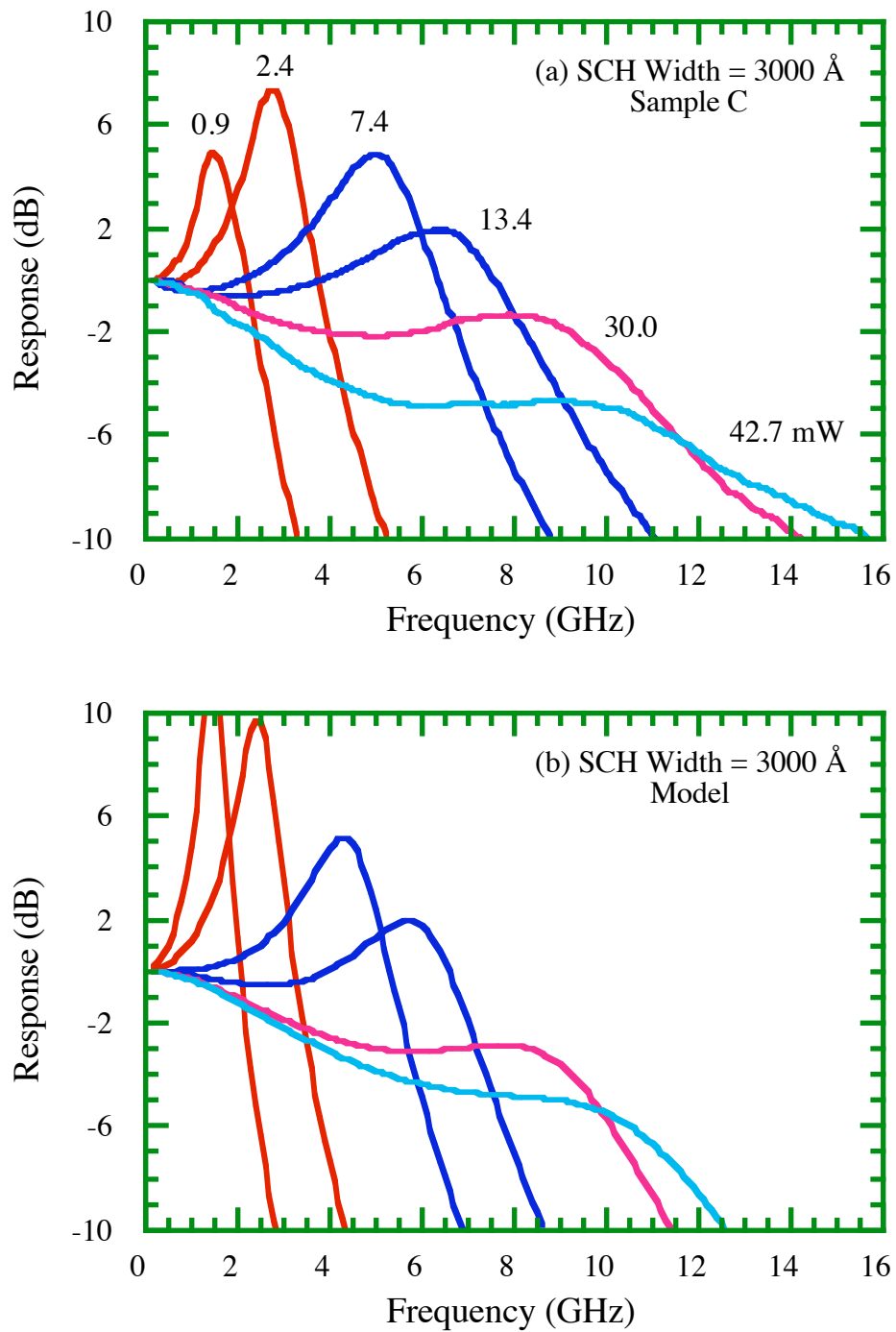


Fig. 3.3 (a) C.W. modulation response for the wide SCH Sample C, compared to the results from the model in (b). The overestimation in the peak of the response at low power levels is due to the omission of the spontaneous emission feedback factor in the model.

The damped response of Sample C shows all the effects predicted by the transport model. The response is *similar* to one of a device which is limited by a low frequency parasitic-like rolloff. In this case it cannot be attributed to device parasitics because both devices had been identically processed. To ascertain this, the parasitics, including the bond wire inductance, were extracted from the S_{11} parameter measured at the input port to the laser mount, and in addition the series resistance was measured using the HP 4145B semiconductor parameter analyzer. The series resistance of the devices is 4Ω . The rolloff frequency due to the device parasitics is about 25 GHz [1] (Appendix D). The spontaneous emission feedback factor, β , does not affect the modulation response at high power levels, but causes an additional damping at sufficiently low power levels. Omission of this factor in the model leads to an overestimation in the peaks of the response at low power levels, as shown in Figs. 3.2 (b) and 3.3 (b).

From the fit to the low frequency rolloff in the modulation response of Sample C, the value of τ_r is determined to be about 54 ps for the 3000 Å SCH width. Using the mobility values quoted in Appendix B, the calculated value for τ_r is 46 ps which is close to the experimental result.

Fig. 3.4 shows the variation of the -3 dB modulation bandwidth with the square root of optical power for Samples B and C. There is good agreement between the experiment and model over a large range of optical power, and the model accurately predicts the discontinuity, caused by carrier transport, in the -3 dB bandwidth for Sample C. The value for ϵ is taken to be $1.5 \times 10^{-17} \text{ cm}^{-3}$ throughout. The bold line gives the exact solution and the dashed line shows the analytical results. For the SCH width of 1500 Å both equations give identical results. At 3000 Å the

bandwidth values predicted by both expressions are almost the same, except in the vicinity of the power level at which the low frequency rolloff causes a *jump* in the curve. This shows that the assumption made to obtain the analytic expressions is valid even for the devices with the widest SCH layers.

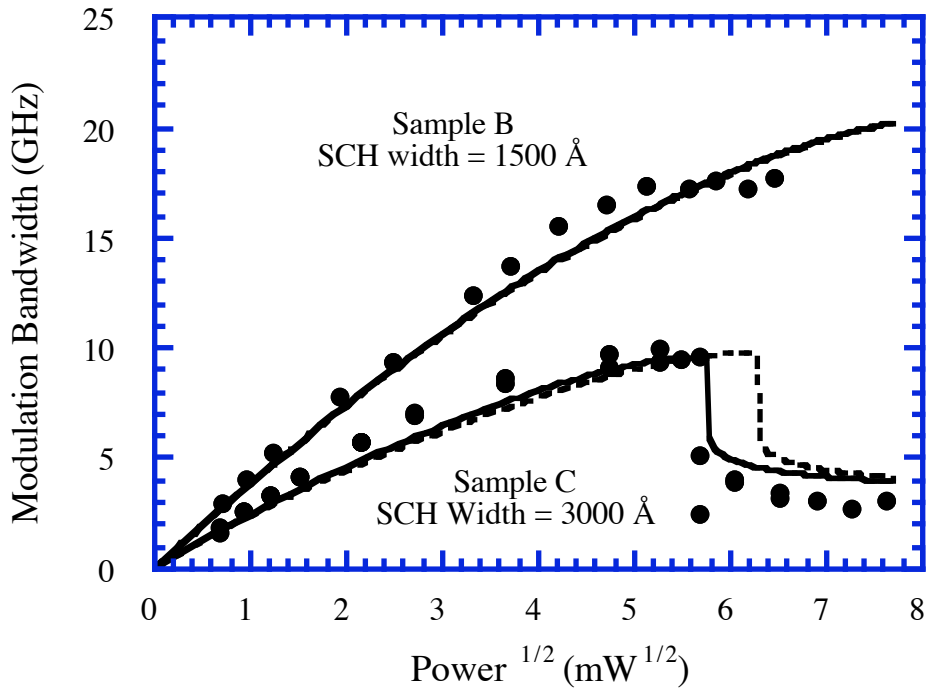


Fig. 3.4 Comparison of the carrier transport model and experiment for the variation of modulation bandwidth with the square root of power. The dashed line is the result from the analytic solution and the bold line that of the exact expression. Severe low frequency rolloff due to carrier transport causes the discontinuity in the curve for Sample C at higher power levels.

Another effect of carrier transport that was predicted is the reduction of γ_0 with increasing SCH width, and this is shown in Fig. 3.5. Increasing the width of SCH, increases χ which decreases γ_0 which is given by $1/\chi\tau_n$. The experimental

values for γ_0 suggest effective bimolecular recombination lifetimes between 125 ps to 250 ps. These are 4 to 8 times smaller than the value of 1 ns typically quoted for radiative recombination lifetimes in semiconductor lasers. The value for γ_0 which is the damping rate at low frequencies, i.e. at low powers, is affected by the spontaneous emission factor, β . Omission of this factor in the model underestimates γ_0 , which is larger in practice due to the contribution to damping from β at low power levels.

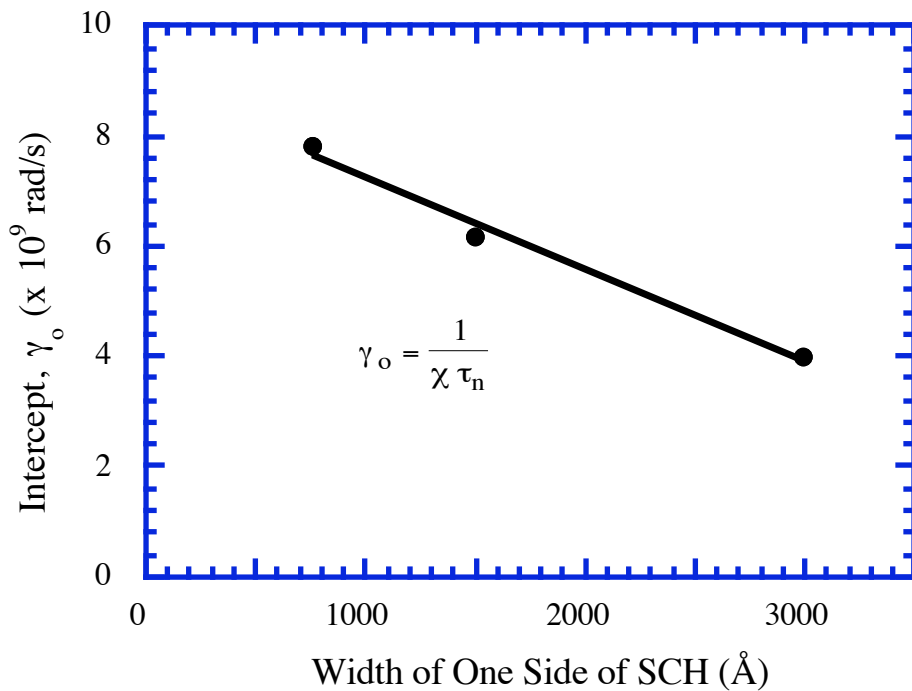


Fig. 3.5 The value of the intercept, γ_0 , of the linear relationship between γ and f_r^2 at various SCH widths. The trend is consistent with the carrier transport model which predicts γ_0 to increase as χ increases with increasing the SCH width.

3.4 Experimental Results - Effect of varying τ_e

The experimental data for the dependence of the high speed parameters on the thermionic emission time is obtained from two samples with different energy barriers

in the SCH; Sample D with $\text{Al}_{0.15}\text{Ga}_{0.85}\text{As}$ SCH and Sample E with GaAs SCH. Fig. 3.6 shows the variation of the resonance frequency with the square root of power obtained from the modulation response data for the two cases considered here. The resonance frequency for the MQW laser with $\text{Al}_{0.15}\text{Ga}_{0.85}\text{As}$ SCH (higher barrier and hence a longer thermionic emission time) is almost twice that of the laser with GaAs SCH at equivalent power levels.

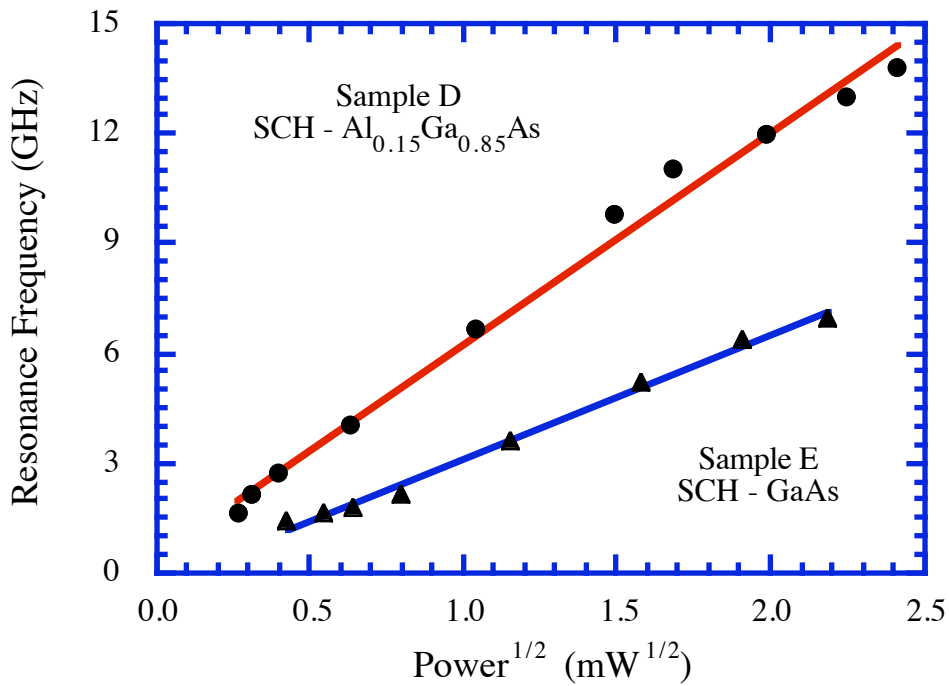


Fig. 3.6 Dependence of the resonance frequency on the square root of power for the MQW samples with a higher ($\text{Al}_{0.15}\text{Ga}_{0.85}\text{As}$) and lower (GaAs) energy barrier in the SCH. The samples each have a $205 \mu\text{m}$ long cavity and a $2 \mu\text{m}$ wide ridge. The slopes are $5.8 \text{ GHz/mW}^{1/2}$ for the $\text{Al}_{0.15}\text{Ga}_{0.85}\text{As}$ SCH and $3.4 \text{ GHz/mW}^{1/2}$ for the GaAs SCH.

The data for the comparison is summarized in the following Table [10], where it can be seen that the differential gain for Sample D is more than 2.5 times that of

Sample E, in agreement with [11]. The gain compression coefficient, ϵ , for both cases is about the same. Both devices have a 205 μm long cavity and a 2 μm wide ridge.

Sample	Threshold Gain	Differential Gain	Gain Compression Factor
D	1440 cm^{-1}	8.6 x 10 ⁻¹⁶ cm^2	1.8 x 10 ⁻¹⁷ cm^3
E	1080 cm^{-1}	3.3 x 10 ⁻¹⁶ cm^2	1.3 x 10 ⁻¹⁷ cm^3

The larger differential gain in the case of Sample D, with $\text{Al}_{0.15}\text{Ga}_{0.85}\text{As}$ SCH, is surprising considering that it had a larger threshold gain, due to a larger internal loss and a smaller optical confinement factor. Consequently, due to gain saturation in quantum well lasers it is *expected* to have a lower differential gain. This result is consistent with the carrier transport model which attributes part of this discrepancy to the reduction in the *effective* or *dynamic* differential gain in Sample E due to an increase in χ caused by a reduction in τ_e [1]. Further, the lower energy barrier and the larger density of states in SCH of Sample E, leads to a severe *carrier overflow* thereby causing a much slower rise in the quasi-Fermi levels under carrier injection [12,13,14]. This reduces the differential gain even under *static* operating conditions.

3.5 Relative Intensity Noise (RIN) Spectrum

The relative intensity noise spectrum can be derived using the same formalism. The difference in this case is that the driving force is no longer the input current, but rather the real part of the Langevin force, F_r , of the field due to the

spontaneous emission which is assumed to be uncorrelated white Gaussian noise [15].

Including this term, the small-signal equations are [4,5],

$$\begin{aligned}
 j \omega p_B &= -\frac{p_B}{\tau_r} + \frac{p_W (V_W / V_{SCH})}{\tau_e} \\
 j \omega p_W &= \frac{p_B (V_{SCH} / V_W)}{\tau_r} - \frac{p_W}{\tau_n} - \frac{p_W}{\tau_e} - \frac{v_g g_o S_o}{1 + \epsilon S_o} p_W - \frac{1}{\Gamma \tau_p (1 + \epsilon S_o)} s \\
 j \omega s &= \frac{\Gamma v_g g_o S_o}{1 + \epsilon S_o} p_W + \frac{s}{\tau_p (1 + \epsilon S_o)} - \frac{s}{\tau_p} + F_r
 \end{aligned}$$

p_B and p_W are eliminated to obtain the expression for the Fourier component of the amplitude fluctuations, $R(\omega)$, due to F_r . Without any simplifying assumptions, $R(\omega)$ is given by [4,5],

$$R(\omega) = F_r \frac{B_0 + j B_1 \omega - B_2 \omega^2}{A_0 + j A_1 \omega - A_2 \omega^2 - j A_3 \omega^3}$$

where the numerator terms are given by,

$$\begin{aligned}
 B_0 &= v_g g_o S_o + \frac{1}{\tau_n} (1 + \epsilon S_o) \\
 B_1 &= (1 + \epsilon S_o) \left(1 + \frac{\tau_r}{\tau_e} + \frac{\tau_r}{\tau_n} \right) + v_g g_o S_o \tau_r \\
 B_2 &= \tau_r (1 + \epsilon S_o)
 \end{aligned}$$

The denominator terms remain unchanged as in the expression for $M(\omega)$. The AM noise spectrum is defined as the power spectral density function, $S_A(\omega)$, of the amplitude fluctuation, and it is written in terms of the Fourier transform of the amplitude fluctuations defined in the time interval $-T/2 < t < T/2$ [15].

$$S_A(\omega) = \lim_{T \rightarrow \infty} \frac{1}{T} \langle R^*(\omega) R(\omega) \rangle$$

The relative intensity noise (*RIN*) is the ratio of the intensity fluctuation to the averaged intensity. To obtain the γ and ω_r in the *conventional* sense of their definitions, i.e. with respect to a second order polynomial in the denominator, one would have to first compute the *RIN* spectrum using the expression given above, and then numerically fit it to a conventional form of the expression and extract the relevant parameters [16].

Again neglecting the frequency dependence of τ_r as previously, the resulting expression for $R(\omega)$ is [4,5],

$$R(\omega) = F_r \frac{\gamma^* + j\omega}{\omega_r^2 - \omega^2 + j\omega\gamma}$$

$$\gamma^* = \frac{(v_g g_o / \chi) S_o}{1 + \epsilon S_o} + \frac{1}{\chi \tau_n}$$

The other terms of the expression are the same as the modulation response function. The γ and γ^* terms are almost identical at sufficiently low powers and small ϵ . The *RIN* spectrum can be easily written in this case as,

$$RIN(f) = \frac{4}{\pi} (\delta f)_{ST} \frac{f^2 + (\gamma^* / 2\pi)^2}{(f_r^2 - f^2)^2 + (\gamma / 2\pi)^2 f^2}$$

where $(\delta f)_{ST}$ is the intrinsic Schawlow-Townes linewidth which is due to spontaneous emission events [15].

The additional low frequency rolloff present in the expression for the modulation response is absent here. For large values of τ_r the modulation bandwidth

could be severely reduced, although the K factor values, which are affected by χ alone and not the low frequency rolloff, as determined from the noise measurements could still be optimistic. It is generally believed that the noise spectrum measurement is a *parasitic free* means of determining the actual or potential modulation performance of a laser. In the presence of significant transport effects this is no longer true.

Fig. 3.7 compares the RIN spectrum computed using the analytic and the exact solutions for the case of the widest SCH devices used in the relative intensity noise spectrum measurements [17]. The agreement is good, as in the case of the analytic expression for the modulation response (Fig. 3.1).

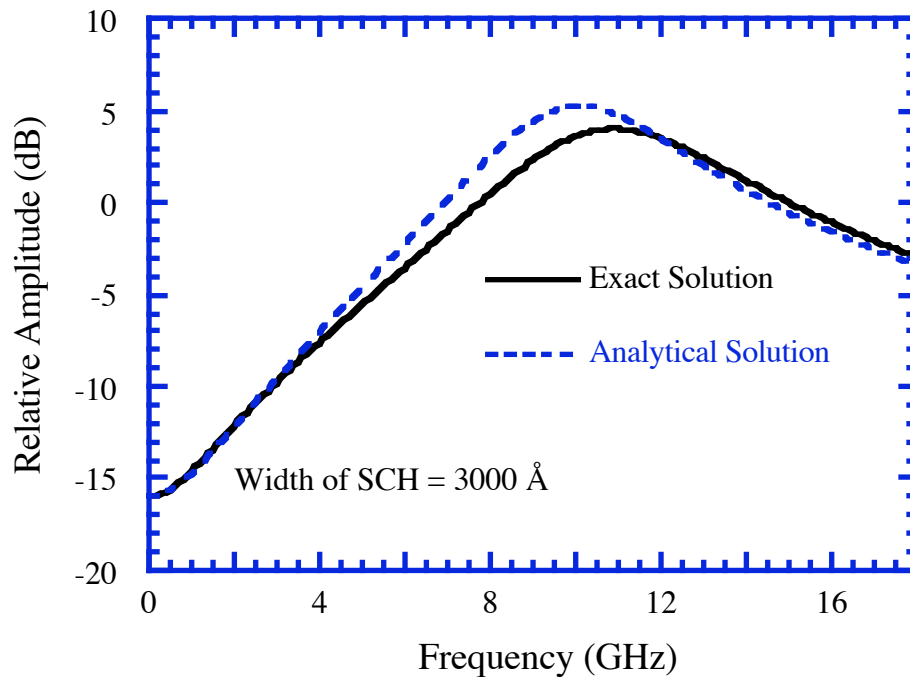


Fig. 3.7 Comparison of the exact and analytical solutions to the RIN spectrum for the laser parameters in Fig. 3.1. The RIN spectrum has been plotted on a relative scale, and does not give the actual noise level for the present set of laser parameters.

Fig. 3.8 shows the modulation response and noise spectrum calculated using the exact expressions, at a power level of 40 mW for a SQW laser with a SCH width of 3000 Å. The peak of the noise spectrum, which is a good indication of the resonance frequency in the presence of small damping, occurs at 10.9 GHz implying a maximum possible modulation bandwidth of 16.9 GHz [4,5] at that power level. This is clearly a wrong conclusion as the *actual* bandwidth limited by carrier transport in this case is only 4.5 GHz.

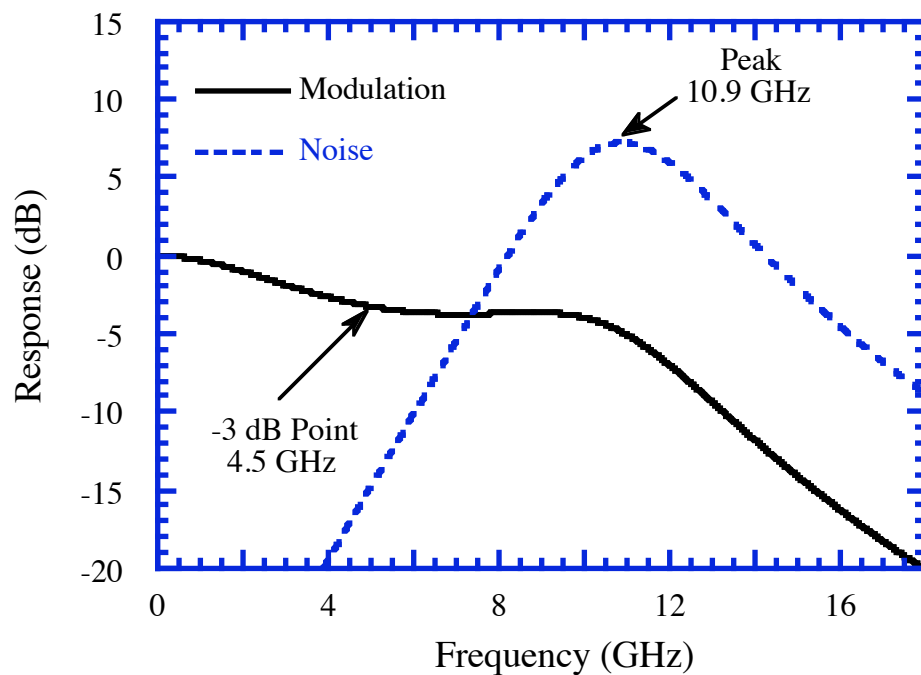


Fig. 3.8 Comparison of the noise spectrum and the modulation response for the same parameters as in Fig. 3.1. The noise spectrum indicates a much larger modulation bandwidth than is physically possible. The modulation response has been normalized with respect to $IM(0)$, and the noise spectrum has been normalized such that it may be conveniently plotted on the same scale as the modulation response.

3.6 Experimental Results

The variation of differential gain and gain compression factor, ϵ , with SCH width (Samples A, B and C) was obtained from the modulation response as well as the relative intensity noise spectra of these lasers. As shown in Fig. 3.9, the results from the modulation response agree with the data extracted from the noise spectra measurements. Fig. 3.9 shows that the gain compression factor slightly increases for larger SCH widths, but given the scatter in the data, this variation of ϵ with SCH is not significant, and this variation alone cannot explain the severe low frequency rolloff (Section 3.3) in Sample C with the widest SCH region.

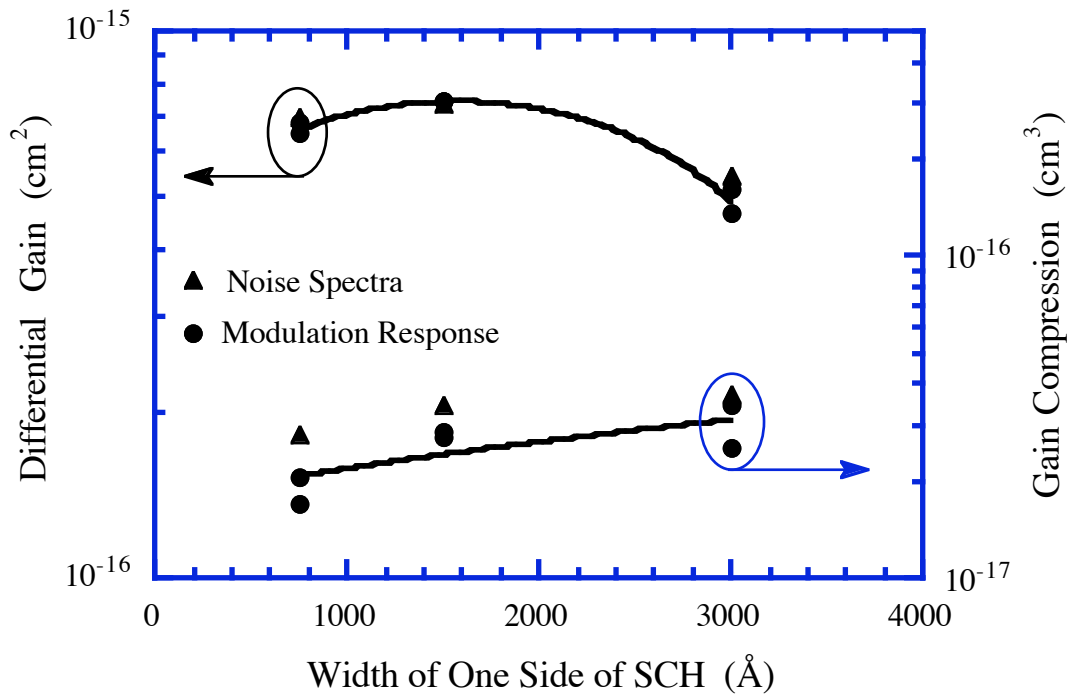


Fig. 3.9 Differential gain and gain compression factor determined from the modulation response and noise spectra. They are in good agreement with one another.

The variation of the differential gain extracted from the modulation response and noise spectra measurements, which can be thought of as an *effective* differential gain, is in contrast to the results from the threshold gain measurements which predict an increasing differential gain value with increasing width of the SCH layer (Fig. B.3). Sample C with the lowest threshold current density has the lowest effective differential gain. This is again due to carrier transport which reduces the differential gain from g_0 to g_0/χ . This reduction in the differential gain is also responsible for the reduction in the resonance frequency at high power levels in Sample C compared to Sample A (Fig. 3.3 (a) compared to 3.2 (a)).

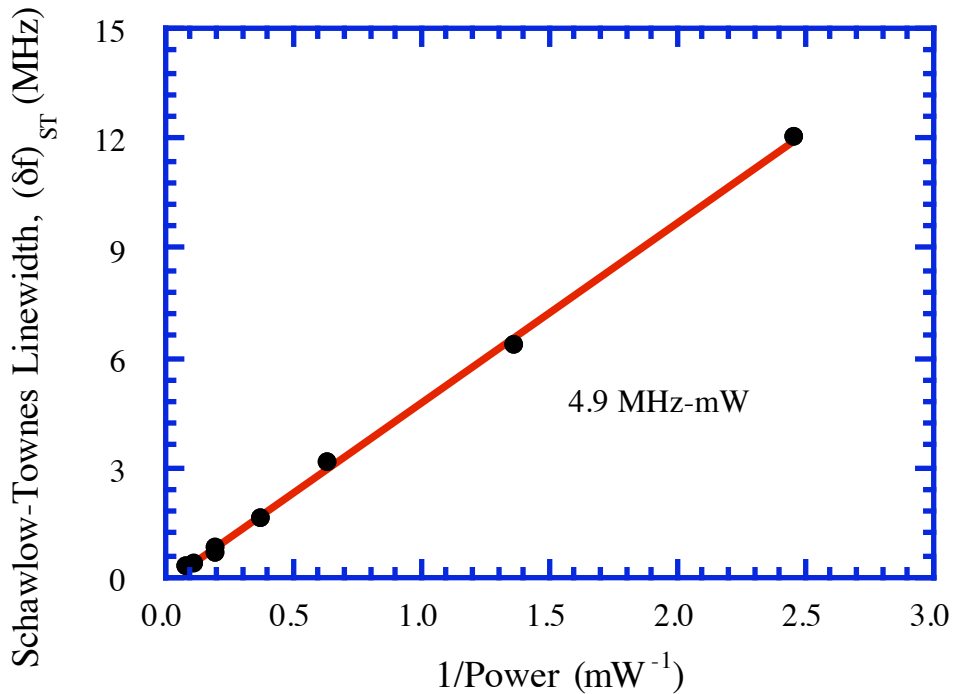


Fig. 3.10 Variation of the Schawlow-Townes linewidth with inverse of the optical power for Sample F device; a SQW laser with 200 μm cavity length and 2.0 μm ridge width.

Fig. 3.10 shows the variation of the Schawlow-Townes linewidth determined from the *AM* noise spectra for a Sample F device with a 200 μm cavity length and a 2.0 μm ridge width. The linewidth, $(\delta f)_{\text{ST}}$, is a parameter which is strictly valid for the case of single frequency lasers. This is the intrinsic linewidth of the laser, and the experimentally measured linewidth is broader due to the linewidth enhancement factor. Although the Fabry Perot lasers used here have a side mode suppression ratio of about 20 dB, $(\delta f)_{\text{ST}}$ in this case is more a measure of an effective *linewidth like* quantity which determines the magnitude of the *AM* noise.

3.7 Temperature Dependence Data

The various carrier transport times in a quantum well laser are a sensitive function of temperature. As a further proof of validity of the present model, the noise spectra of the lasers at various temperatures between - 65 °C and + 50 °C were measured, and the temperature dependence of *K* factor was extracted.

In semiconductor lasers, even in the absence of transport effects, the *K* factor would increase with temperature if the gain compression factor is temperature independent. This is because the gain, and thus the differential gain, decreases as the temperature increases (Fig. B.4). In the presence of transport effects, this increase would be more pronounced because the transport factor χ also increases with temperature leading to a further reduction in the differential gain.

Fig. 3.11 (a) shows the variation of *K* factor with temperature for Sample F, which is a SQW laser with a SCH width of 900 Å, and Fig. 3.11 (b) that of Sample C, which is also a SQW laser but with a SCH width of 3000 Å [17]. The *K* factor for Sample C is much more sensitive to temperature variations than Sample F.

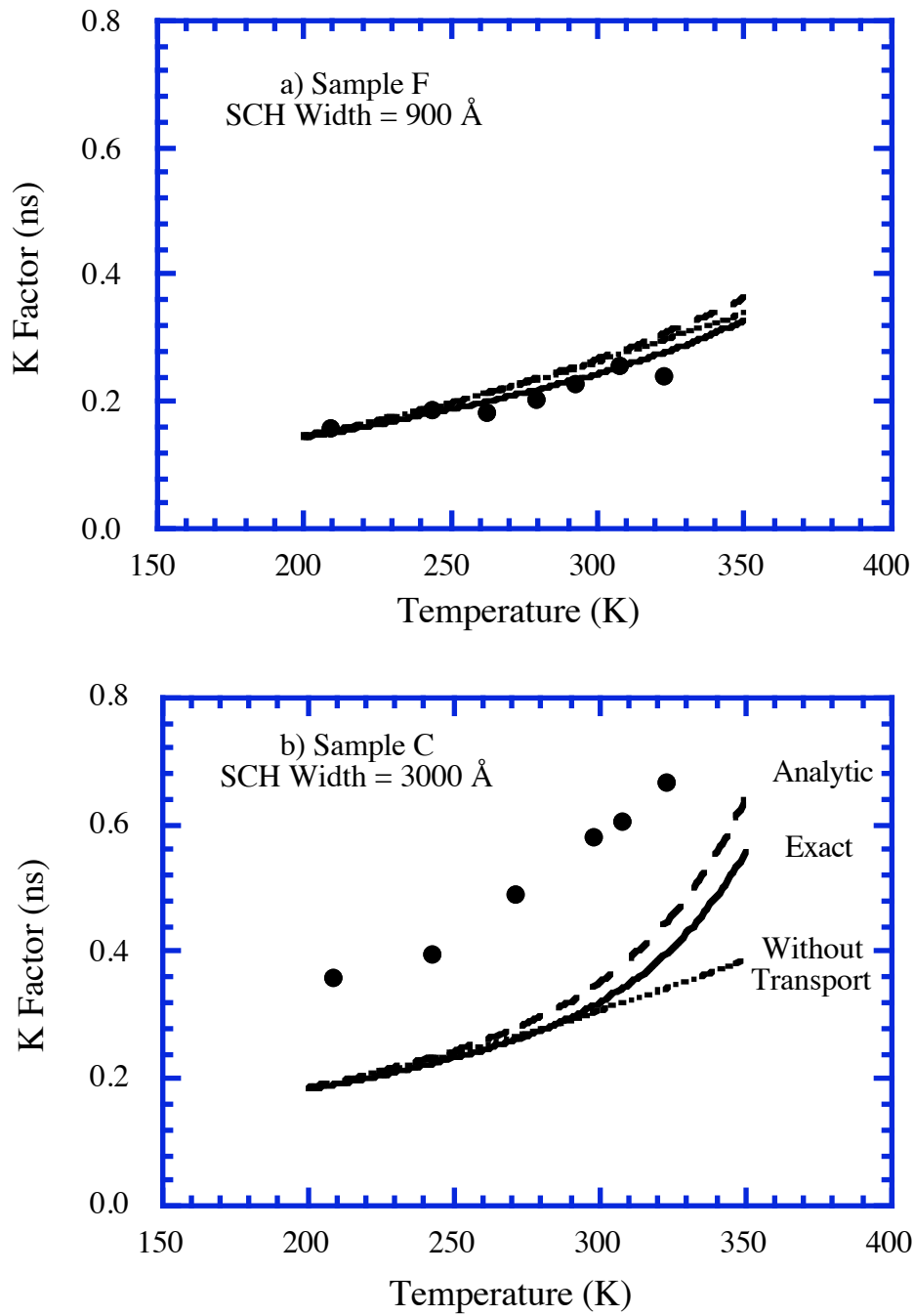


Fig. 3.11 Temperature dependence of K factor for (a) a narrow SCH (Sample F) and (b) a wide SCH (Sample C) SQW laser. A large contribution to the significant variation of K factor with temperature for wide SCH devices comes from the temperature dependence of the transport parameters.

Results from the model for three cases have been presented in Figs. 3.11 (a) and (b) together with the experimental data. The first curve was computed using the analytic expression, the second using the exact solution, and the third using the analytic solution but neglecting transport effects and considering only the variation in differential gain with temperature. For the case of Sample F, where the transport effects are not significant, all three curves lie close to one another and do not show much variation with temperature. For Sample C, variations in differential gain with temperature alone is clearly insufficient to explain the K factor trend with temperature. From the Figs. 3.11 (a) and (b) it can be seen that the analytic solution is in good agreement with the exact solution. There is some discrepancy in the actual K factor values predicted in the wide SCH case. The model assumes a constant value for the gain compression factor, ϵ , but experimentally there is some increase in the ϵ values for the wide SCH devices (Fig. 3.9). This increase in ϵ will have to be taken into account for better agreement between the model and the experiment.

The enhanced temperature sensitivity of the K factor in the wide SCH case is the result of the temperature dependence of the transport parameters. Fig. 3.12 shows the calculated variation of τ_e , τ_r and χ with temperature for Sample C with the widest undoped SCH region. The thermionic emission time decreases exponentially with temperature, and is the major contributor to the increase in χ . The SCH diffusion time is temperature dependent via the temperature dependence of the ambipolar diffusion coefficient. Generally the carrier mobilities decrease as the square of the temperature, and the diffusion coefficient increases linearly with temperature leading to a linear increase in τ_r with temperature. Both the decrease in τ_e and the increase in τ_r lead to an increase in χ , and thus an enhanced reduction in K . This clearly

demonstrates the significant role played by carrier transport in the modulation dynamics of semiconductor lasers.

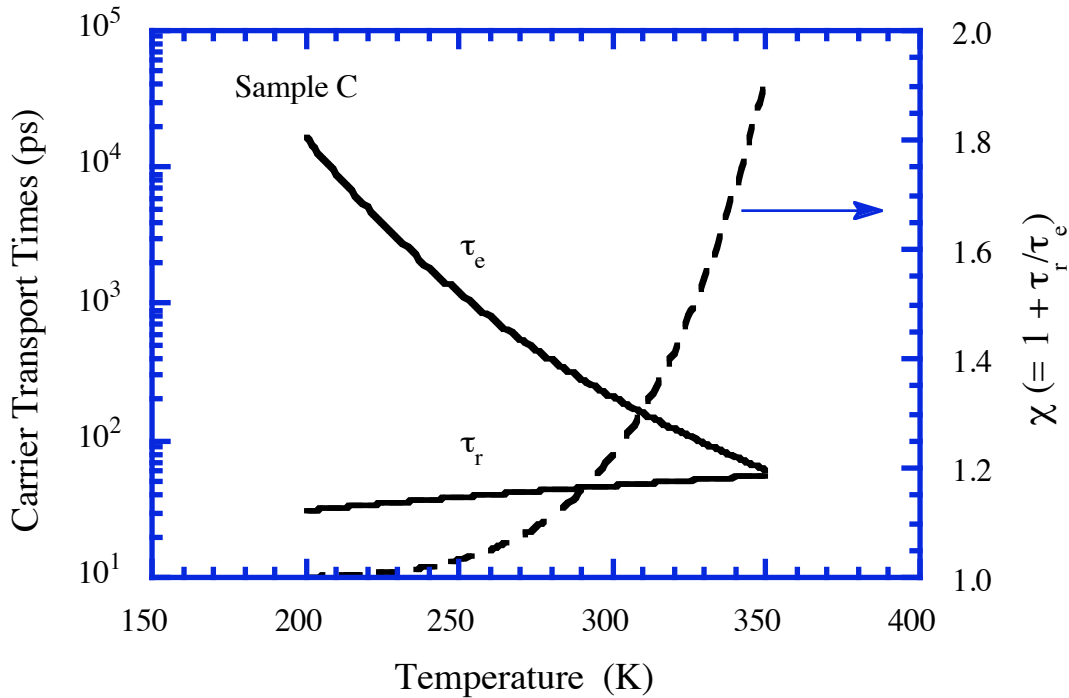


Fig. 3.12 Calculated temperature dependence of the transport times and the transport factor, χ , for the wide SCH sample. As the temperature increases, the thermionic emission lifetime from the quantum well is considerably reduced, and the transport time across the SCH is somewhat enhanced, leading to a significant increase in the transport factor χ for wide SCH devices.

3.8 Maximum Possible Modulation Bandwidth

Conventionally, the maximum possible modulation bandwidth in a semiconductor laser was determined by the K factor. In principle, if one could drive the laser to arbitrarily high output power levels without the deteriorating effects of device heating, then the maximum possible - 3 dB bandwidth, in the absence of

device parasitics, is given by this K factor limit. In the presence of carrier transport effects, the K factor is not only reduced due to the reduction in the effective differential gain, but also *no longer determines the maximum modulation bandwidth*, even in an otherwise perfect device.

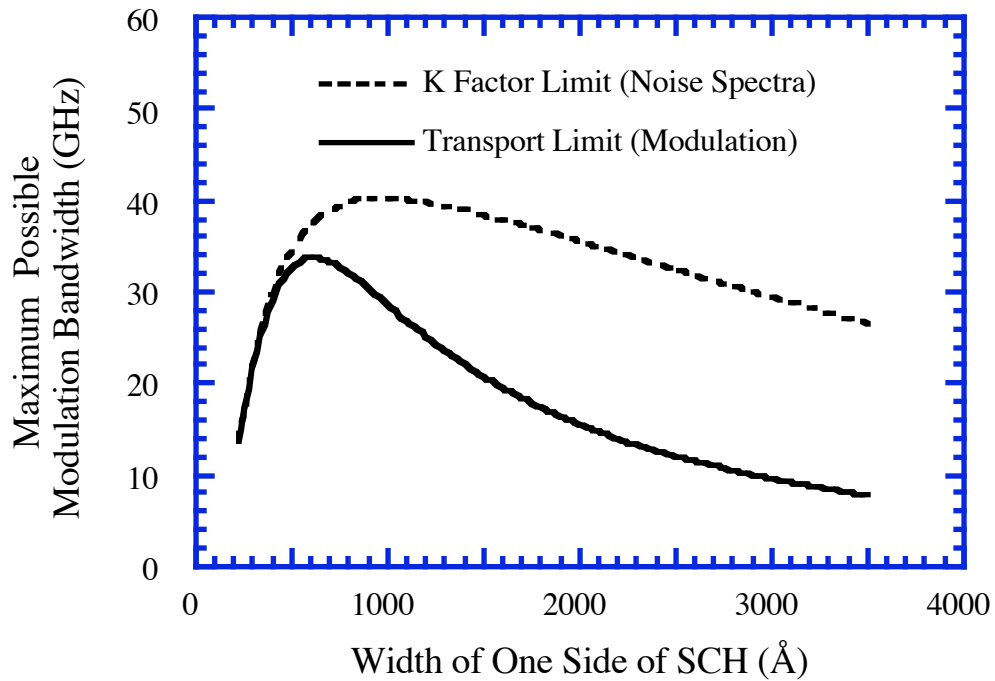


Fig. 3.13 Comparison of maximum possible modulation bandwidth inferred from the modulation response and intensity noise measurements.

Fig. 3.13 shows the maximum possible modulation bandwidth as a function of SCH width for a 300 μm cavity length SQW laser. The dashed line shows the K factor limit which is commonly inferred from noise spectra measurements. The bold line is the *real limit* determined by carrier transport across the SCH; this is the maximum that is possible before the low frequency rolloff due to transport becomes

severe enough to cause a *sudden drop* in the variation of modulation bandwidth with increasing optical power.

Herein lies the real danger of relying on K factors and RIN measurements to predict modulation bandwidths. A small K factor is indeed an indication of the good device and material quality, but one has to be careful as to the maximum modulation bandwidth limits implied by this quantity. One can truly use this as the limit only in devices where the carrier transport effects are minimal.

References

1. R. Nagarajan, T. Fukushima, M. Ishikawa, J. E. Bowers, R. S. Geels, and L. A. Coldren, "Transport Limits in High Speed Quantum Well Lasers: Experiment and Theory," *Photon. Tech Lett.*, vol. 4, pp. 121-123, 1992.
2. R. Nagarajan, M. Ishikawa, T. Fukushima, R. S. Geels and J. E. Bowers, "Carrier Transport Effects in High-Speed Quantum-Well Lasers," *Laser Diode Technology and Applications IV, OE/LASE '92 (SPIE Conference #1634)*, paper 1634-14, Los Angeles, Jan. 1992.
3. R. Nagarajan, M. Ishikawa, T. Fukushima, R. S. Geels and J. E. Bowers, "High Speed Quantum Well Lasers and Carrier Transport Effects," *J. Quantum Electron.*, 1992.
4. R. Nagarajan, M. Ishikawa, and J. E. Bowers, "Effects of Carrier Transport on Relative Intensity Noise and Critique of K Factor Predictions of Modulation Response," *Electron. Lett.*, vol. , pp. 846-847, 1992.
5. R. Nagarajan, M. Ishikawa and J. E. Bowers, "Effects of Carrier Transport on Relative Intensity Noise and Modulation Response in Quantum Well Lasers," *High-Speed Electronics and Optoelectronics, Symposium on Compound Semiconductor Physics and Devices, (SPIE Conference #1680)*, paper 1680-11, Somerset (New Jersey), USA, Mar. 1992.
6. J. E. Bowers, B. R. Hemenway, A. H. Gnauck, and D. P. Wilt, "High-Speed InGaAsP Constricted-Mesa Lasers," *J. Quantum Electron.*, vol. 22, pp. 833-844, 1986.
7. R. Olshansky, P. Hill, V. Lanzisera, and W. Powazinik, "Frequency Response of 1.3 μm InGaAsP High Speed Semiconductor Lasers," *J. Quantum Electron.*, vol. 23, pp. 1410-1418, 1987.
8. W. Rideout, W. F. Sharfin, E. S. Koteles, M. O. Vassell, and B. Elman, "Well-Barrier Hole Burning in Quantum Well Lasers," *Photon. Tech. Lett.*, vol. 3, pp. 784-786, 1991.

9. R. Nagarajan, T. Fukushima, S. W. Corzine, and J. E. Bowers, "Effects of Carrier Transport on High-Speed Quantum Well Lasers," *Appl. Phys. Lett.*, vol. 59, pp. 1835-1837, 1991.
10. R. Nagarajan, R. P. Mirin, T. E. Reynolds, and J. E. Bowers, "Effect of the Confinement Layer Composition on the Internal Quantum Efficiency and Modulation Response of Quantum Well Lasers," *Photon. Tech. Lett.*, August 1992.
11. L. F. Lester, W. J. Schaff, X. J. Song, and L. F. Eastman, "Modulation Characteristics of Short-Cavity Strained-Layer Lasers," *High-Speed Electronics and Optoelectronics, Symposium on Compound Semiconductor Physics and Devices, (SPIE Conference #1680)*, paper 1680-12, Somerset (New Jersey), USA, Mar. 1992.
12. J. Nagle, S. Hersee, M. Krakowski, T. Weil, and C. Weisbuch, "Threshold Current of Single Quantum Well Lasers: The Role of the Confining Layers," *Appl. Phys. Lett.*, vol. 49, pp. 1325-1327, 1986.
13. R. Nagarajan, T. Kamiya, and A. Kurobe, "Band Filling in GaAs/AlGaAs Multi-quantum Well Lasers and its Effect on the Threshold Current," *J. Quantum Electron.*, vol. 25, pp. 1161-1170, 1989.
14. B. Zhao, T. R. Chen, and A. Yariv, "Comparison of Differential Gain in Single Quantum Well and Bulk Double Heterostructure Laser", *Electron. Lett.*, vol. 27, pp. 2343-2345, 1991.
15. K. Kikuchi, and T. Okoshi, "Measurement of FM Noise, AM Noise, and Field Spectra of 1.3 μm InGaAsP Lasers and Determination of the Linewidth Enhancement Factor," *J. Quantum Electron.*, vol. 21, pp. 1814-1818, 1985.

See also T. Okoshi, and K. Kikuchi, *Coherent Optical Fiber Communications*, Tokyo:KTK Scientific, 1988, pp. 67.
16. M. Ishikawa, R. Nagarajan, T. Fukushima, J. Wasserbauer, and J. E. Bowers, "Long Wavelength High Speed Semiconductor Lasers with Carrier Transport Effects," *J. Quantum Electron.*, October 1992.

17. M. Ishikawa, T. Fukushima, R. Nagarajan, and J. E. Bowers, "Temperature Dependence of Damping in High Speed Quantum Well Lasers," *Appl. Phys. Lett.*, July 1992.

CHAPTER 4

INTERNAL QUANTUM EFFICIENCY

4.1 Background

The losses in the semiconductor laser fall into two general categories; one is the mirror loss, α_{mir} , which is the result of light emission from the cavity, and the other is the internal loss, α_{int} , which results from the various light scattering and radiation processes which do not contribute to useful power emission from the facets. A relationship can be written in terms of these losses for a quantity called external quantum efficiency, η_{ext} , which measures the injected carrier to photon conversion efficiency of the laser.

$$\eta_{\text{ext}} = \eta_i \frac{\alpha_{\text{mir}}}{\alpha_{\text{mir}} + \alpha_{\text{int}}}, \quad \text{where } \alpha_{\text{mir}} = \frac{1}{2 L_c} \ln\left(\frac{1}{R_1 R_2}\right)$$

The internal quantum efficiency term, η_i , has been phenomenologically included to account for the nonradiative recombination processes which deplete the injected carriers, and do not emit photons [1]. Thus, η_i is the fraction of the injected carriers that actually contribute to light emission. R_1 and R_2 refer to the front and the rear facet reflectivities of the cavity and L_c is the cavity length. Typically for semiconductor lasers with cleaved facets, $R = R_1 = R_2 = 0.3$. The internal quantum efficiency and the internal loss of the laser material are experimentally determined from the external quantum efficiency measurements on broad area lasers of various cavity lengths.

After substituting for α_{mir} in the expression for η_{ext} , we have

$$\frac{1}{\eta_{\text{ext}}} = \left(\frac{\alpha_{\text{int}}}{\eta_i} \right) \frac{L_c}{\ln\left(\frac{1}{R}\right)} + \frac{1}{\eta_{\text{int}}}$$

Using this expression, the internal quantum efficiency and internal loss can be determined by plotting $1/\eta_{\text{ext}}$ against $\frac{L_c}{\ln(1/R)}$ for lasers of several cavity lengths, and reading off the slope and the intercept of the linear relationship.

The external quantum efficiency is derived from the slope or the differential efficiency of the L/I curve. The slope of the L/I curve, η_d , is typically given in the units of mW/mA. This is converted into, η_{ext} , which is a dimensionless quantity. For a Fabry Perot laser structure with identical facet reflectivities, η_{ext} is given by

$$\eta_{\text{ext}} = \frac{2 \lambda q}{h c} \eta_d$$

where λ is the wavelength of operation of the laser, h is the Planck's constant and c is the speed of light in vacuum. The factor of 2 accounts for light emission from both facets of the laser cavity.

4.2 Theoretical Expression for Internal Quantum Efficiency

From the carrier transport model, laser structures with a small thermionic emission time out of the quantum well should have a large number of carriers occupying the SCH and barrier states. This, in principle, should not only affect the differential gain [2,3,4], but also the internal quantum efficiency or the carrier collection efficiency of the laser [2,3,5,6]. The internal quantum efficiency, η_i , at threshold can be written as,

$$\eta_i = \frac{\frac{N_W}{\tau_n}}{\frac{N_W}{\tau_n} + \frac{N_W}{\tau_{nr}} + \frac{N_B}{\tau_{nb}}}$$

where N_W and N_B are the number of carriers in the quantum well and the SCH respectively, τ_n is the radiative lifetime in the quantum well, τ_{nr} is the nonradiative lifetime in the quantum well, and τ_{nb} is the total recombination lifetime (including radiative and nonradiative) in the SCH. The leakage currents and interface recombination (Chapter two) cause an additional reduction in η_i . The rate equation at threshold, assuming that the stimulated emission is negligible, for the carriers in the quantum well can be written as,

$$\frac{dN_W}{dt} = \frac{N_B}{\tau_r} - \frac{N_W}{\tau_e} - \frac{N_W}{\tau_n} - \frac{N_W}{\tau_{nr}}$$

From the steady state solution to this rate equation, $\frac{dN_W}{dt} = 0$, we can obtain a relationship for the N_B/N_W ratio. Substituting this in the expression for η_i ,

$$\eta_i = \frac{1}{1 + \frac{\tau_r}{\tau_e} \left(\frac{\tau_n}{\tau_{nb}} \right) + \frac{\tau_r}{\tau_{nb}} \left(1 + \frac{\tau_n}{\tau_{nr}} \right) + \frac{\tau_n}{\tau_{nr}}}$$

Typically the recombination rate in the confinement region is negligible compared to the carrier transport/capture rate, $\tau_{nb} \gg \tau_r$. With this, the expression for η_i simplifies to;

$$\eta_i \approx \frac{1}{1 + \frac{\tau_r}{\tau_e} \left(\frac{\tau_n}{\tau_{nb}} \right) + \frac{\tau_n}{\tau_{nr}}}$$

In the limit of negligible recombination in the SCH and negligible nonradiative recombination in the active area, $\eta_i \approx 1$, *irrespective* of the relative magnitudes of τ_c and τ_r , i.e. χ , but in practice these recombination rates are not negligible, and a large χ contributes significantly to a reduction in η_i . Enhanced light emission from the confinement layers of heavily damped lasers have been experimentally observed [7].

In the limit of $\tau_n = \tau_{nb}$ and $\tau_{nr} \gg \tau_n$, the internal quantum efficiency and the transport factor have a simple relationship;

$$\eta_i \approx \frac{1}{\chi}$$

This limit for η_i is ideal because we have ignored the nonradiative recombination in the active area.

4.3 Experimental and Theoretical Results

The experimental data for the variation of internal quantum efficiency with thermionic emission time out of the quantum well is obtained from Samples D, E and G. Samples D and E are identical except for the composition of the SCH layer. Sample G also has 3 QWs and an SCH width which is almost identical (only 40 Å wider). The only other difference is that the cladding layer is $\text{Al}_{0.6}\text{Ga}_{0.4}\text{As}$ compared to $\text{Al}_{0.7}\text{Ga}_{0.3}\text{As}$ for the other two samples.

Fig. 4.1 shows the calculated variation of the $1/\chi$ limit for η_i with Al mole fraction in the SCH. If we assume that the discrepancy in the $1/\chi$ and η_i values for Sample D, with the 15 % Al mole fraction, is solely due to nonradiative mechanisms, then a τ_n/τ_{nr} ratio of 0.1 would resolve the difference. Fig. 4.1 also shows the theoretical variation of η_i , computed using the τ_n/τ_{nr} ratio of 0.1, and the

experimental data for different Al mole fraction in the SCH. The $1/\chi$ limit deviates from the exact expression for η_i at larger Al mole fraction, but the trend is the same in both cases.

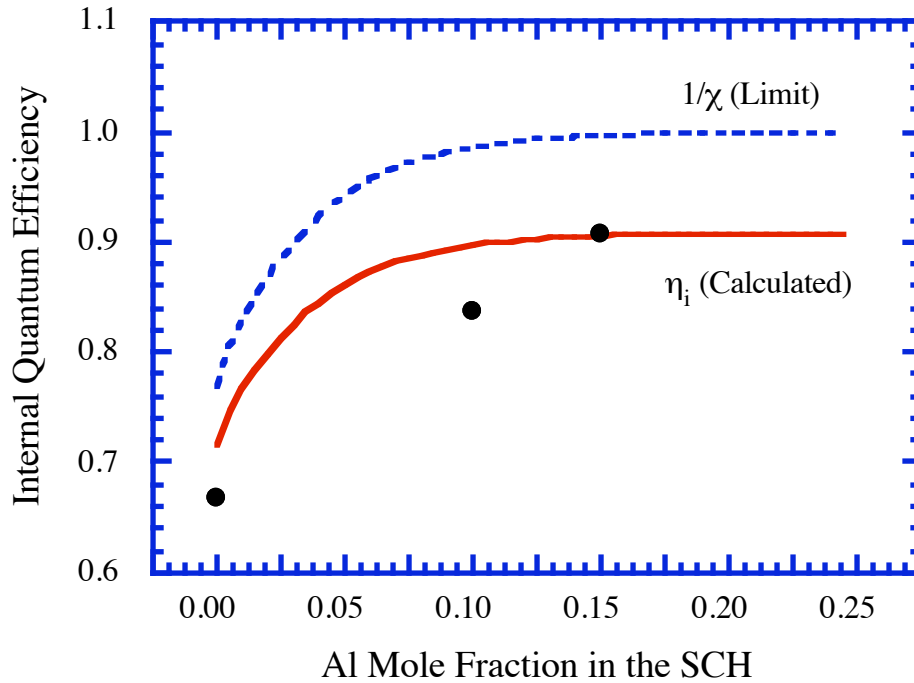


Fig. 4.1 Variation of internal quantum efficiency with Al content in the AlGaAs SCH. The experimental data points are given by full circles.

The internal quantum efficiency is also a function of temperature. At higher temperatures the thermionic emission rate is greatly increased, and the gain is reduced. The reduction in gain leads to an increase in bandfilling to reach the threshold condition, even if the cavity loss is independent of temperature. These effects increase the carrier occupation of the states in the barriers and the SCH. This

leads to an increase in the recombination from these layers, and hence a reduction of the internal quantum efficiency.

Fig. 4.2 shows the variation of the internal quantum efficiency with Al mole fraction in the SCH at different temperatures. At higher temperatures there is a drastic reduction in the internal quantum efficiency, and this requires the use of SCH layers with larger Al mole fractions for proper high speed operation of these lasers at elevated temperatures. In this calculation the radiative recombination time and the material gain has been assumed to be independent of temperature. In practice, the reduction of material gain with increase in temperature will further aggravate the problem.

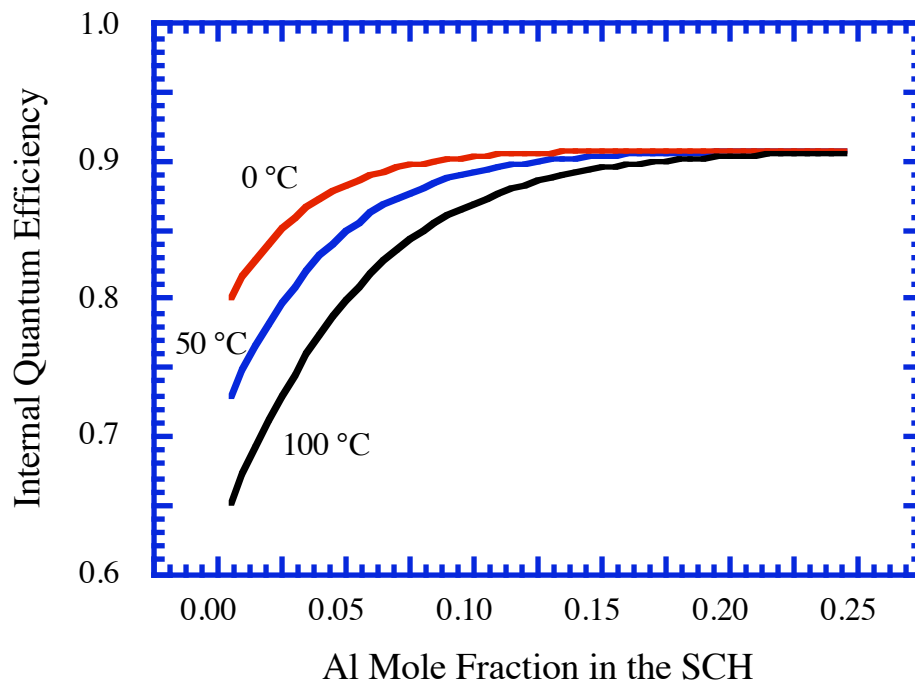


Fig. 4.2 Temperature dependence of internal quantum efficiency for different Al content in the AlGaAs SCH. The calculation is done for a τ_n/τ_{nr} ratio of 0.1 at all temperatures.

From Fig. 4.2, the use of 15% Al in the SCH layer seems to be sufficient for a high internal quantum efficiency in quantum well lasers operating at room temperature. In practice, this value is very much dependent on the threshold gain of the laser. For a large internal loss, increased levels of bandfilling at threshold will result in a reduced internal quantum efficiency. Experimentally this trend has been reported in the InGaAs system [8]. By varying the Al content in the cladding regions for a given InGaAs/GaAs quantum well-SCH system, the authors of Ref. [8] have observed an increase in the emission wavelength (due to a reduction in bandfilling) with an increase in the Al composition which increases the energy barrier to carrier overflow. In some cases, like the vertical cavity surface emitting lasers which operate at much larger current densities, Al mole fraction as high as 50% may be required in the SCH for efficient operation [9].

References

1. G. P. Agrawal, and N. K. Dutta, *Long Wavelength Semiconductor Lasers*, New York:Van Nostrand Reinhold, 1986, pp. 57.
2. R. Nagarajan, T. Kamiya, and A. Kurobe, "Band Filling in GaAs/AlGaAs Multiquantum Well Lasers and its Effect on the Threshold Current," *J. Quantum Electron.*, vol. 25, pp. 1161-1170, 1989.
3. R. Nagarajan, R. P. Mirin, T. E. Reynolds, and J. E. Bowers, "Effect of the Confinement Layer Composition on the Internal Quantum Efficiency and Modulation Response of Quantum Well Lasers," *Photon Tech. Lett.*, August 1992.
4. B. Zhao, T. R. Chen, and A. Yariv, "Comparison of Differential Gain in Single Quantum Well and Bulk Double Heterostructure Laser", *Electron. Lett.*, vol. 27, pp. 2343-2345, 1991.
5. J. Nagle, S. Hersee, M. Krakowski, T. Weil, and C. Weisbuch, "Threshold Current of Single Quantum Well Lasers: The Role of the Confining Layers," *Appl. Phys. Lett.*, vol. 49, pp. 1325-1327, 1986.
6. H. Shichijo, R. M. Kolbas, N. Holonyak, Jr., R. D. Dupuis, and P. D. Dapkus, "Carrier Collection in a Semiconductor Quantum Well," *Solid State Comm.*, vol. 27, pp. 1029-1032, 1978.
7. W. F. Sharfin, W. Rideout, E. Koteles, J. Schlafer, B. Elman, M. Vassell, D. Crawford, J. Benoit, P. Brosson, and B. Fernier, "Effect of Carrier Transport on Modulation Bandwidth of Quantum Well Lasers," in *Proc. 17th ECOC / 8th IOOC '91*, 1991, pp. 133.
8. P. K. York, S. M. Langsjoen, L. M. Miller, K. J. Beernink, J. J. Alwan, and J. J. Coleman, "Effect of Confining Layer Aluminum Composition on AlGaAs-GaAs-InGaAs Strained-Layer Quantum Well Heterostructure Lasers," *Appl. Phys. Lett.*, vol. 57, pp. 843-845, 1990.

9. J. W. Scott, R. S. Geels, S. W. Corzine, and L. A. Coldren, "Modeling Temperature Effects and Spatial Hole Burning to Optimize Vertical-Cavity Surface-Emitting Laser Performance," submitted to *J. Quantum Electron.*

CHAPTER 5

OPTIMIZATION OF HIGH SPEED LASERS

5.1 Material Considerations for the Enhancement of Differential Gain

Differential gain or the rate of change of gain with change in carrier density is one of the important parameters of concern when designing high speed lasers. Fig. 5.1 shows a schematic diagram of the approaches typically taken for the maximization of the differential gain in semiconductor lasers.

In bulk lasers, the differential gain is a more often a property of the material chosen for the active layer, and is relatively independent of the carrier density at which the diode operates. In this case, enhancement in differential gain has been demonstrated by selectively *p*-doping the active layer [1,2].

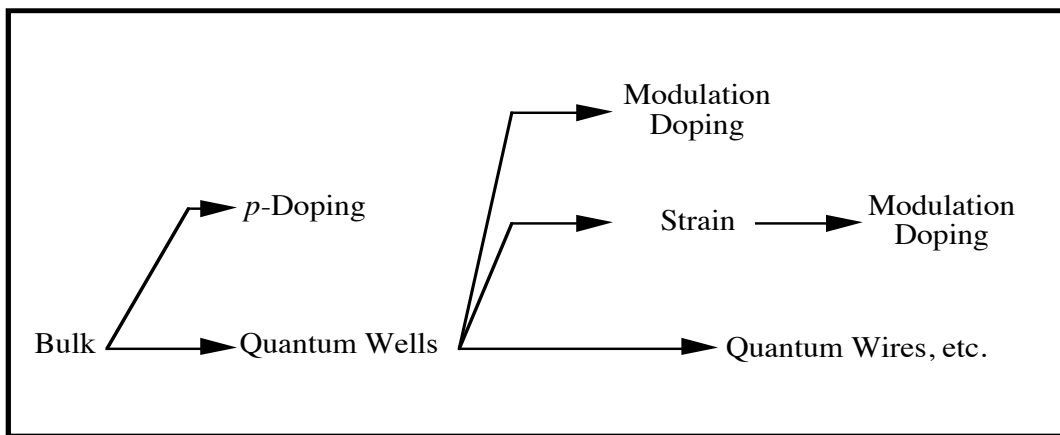


Fig. 5.1 Schematic diagram showing the possible approaches to enhance differential gain in semiconductor lasers.

An improvement over the bulk case is to use quantum wells for the active area [3]. The inclusion of strain in the active area reduces the in-plane hole effective mass at the bandedge, and leads to a reduction of the valence band density of states. This has been predicted and demonstrated to enhance the differential gain over the unstrained case [4,5,6]. In the case of quantum well structures the barriers and/or the confinement regions may be preferentially *p*-doped instead of the active layer. This has an advantage over the direct doping case. The optical properties of the active layer are not modified (by the formation of band tails and bandgap shrinkage), and the internal loss due to free carrier absorption is reduced as the ionized impurities are placed at some distance from the active layer. This is called modulation doping and differential gain enhancement has also been observed in this case [7].

As shown in Fig. 5.1, further improvements in differential gain may be obtained by using active layers with higher degrees of quantum carrier confinement. Theoretical [3,8] and some experimental work [3] done using high magnetic fields (resulting in carrier confinement by the formation of Landau energy bands) in this area show that it may be possible to obtain further enhancement in differential gain by using quantum wires and quantum boxes as the active layer in semiconductor lasers.

5.2 Maximization of the Optical Confinement Factor

The quantum wells have relatively small widths, and unlike the bulk lasers with much larger active areas, they require a separate confinement heterostructure (SCH) to maximize the transverse optical confinement factor. The SCH is inserted between the cladding regions and the quantum well active area. Given the sophistication of modern crystal growth techniques, the composition profile of the

SCH can be tailored in a number of ways to suit the particular application. For any specific energy profile chosen, the dimensions will have to be optimized for maximum mode confinement. This will ensure that the gain at threshold is minimized, and hence the differential gain is maximized. These ideas are presented in Fig. 5.2.

The upper part of Fig. 5.2 shows four typical profiles that may be employed in the fabrication of the SCH layer; 1) ungraded, 2) parabolic grading, 3) linear grading, and 4) inverse parabolic grading. The optical confinement factor is computed for the first order TE mode by first calculating the near field pattern, and then calculating the mode overlap with the quantum well. The program solves the second order Maxwell wave equation using the finite difference algorithm. This technique has the advantage that any arbitrary SCH profile can be easily analyzed without having to modify the original source code. A nonuniform mesh is used to discretize the wave equation, and by the way of matrix transformations, the symmetry of the resulting *banded* matrix is preserved. This allows for an accurate solution of the confinement factor with a minimal use of the computing resources [9].

Fig. 5.2 also shows the variation of the optical confinement factor with SCH width for the four different energy profiles considered. The confinement factor has a maximum value at different SCH widths for the different profiles. The results show that an optimized SCH with no grading at all has the largest optical confinement factor. The optimum width for the ungraded SCH is also the smallest. This is an advantage when carrier transport times become significant. Thus, the ungraded SCH is the most favored design for high speed lasers.

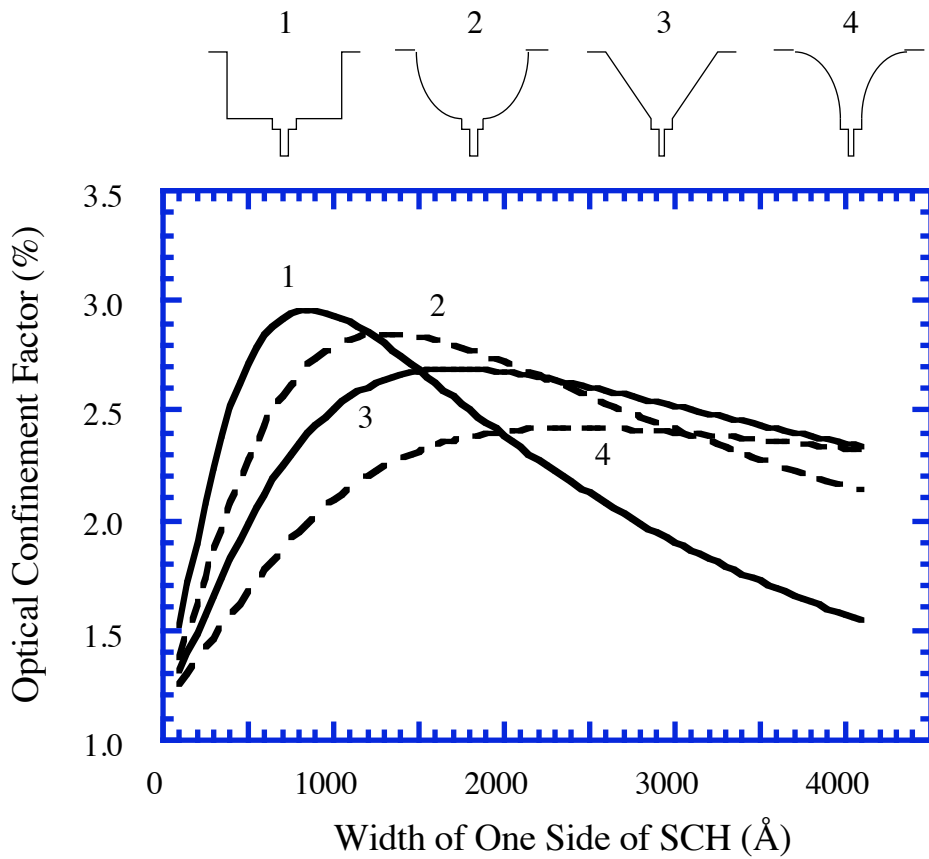


Fig. 5.2 Variation of optical confinement factor with SCH width for different energy profiles. All the profiles have a 50 Å GaAs smoothing layer adjacent to the 80 Å $\text{In}_{0.2}\text{Ga}_{0.8}\text{As}$ single quantum well. The SCH is graded from $\text{Al}_{0.6}\text{Ga}_{0.4}\text{As}$ to $\text{Al}_{0.1}\text{Ga}_{0.9}\text{As}$ on either side of the smoothing layer over the distance plotted as the independent variable.

Fig. 5.3 shows the variation of the optical confinement factor with the SCH width for the case of the ungraded SCH at three different levels of the Al composition in the cladding region. From the plots it is evident that higher the Al mole fraction, the larger the optical confinement factor. Further the optimal width of the SCH required is also somewhat reduced with the increasing Al mole fraction. Larger Al

containing cladding regions are more desirable, if they could grown just as efficiently, without enhanced incorporation of impurities.

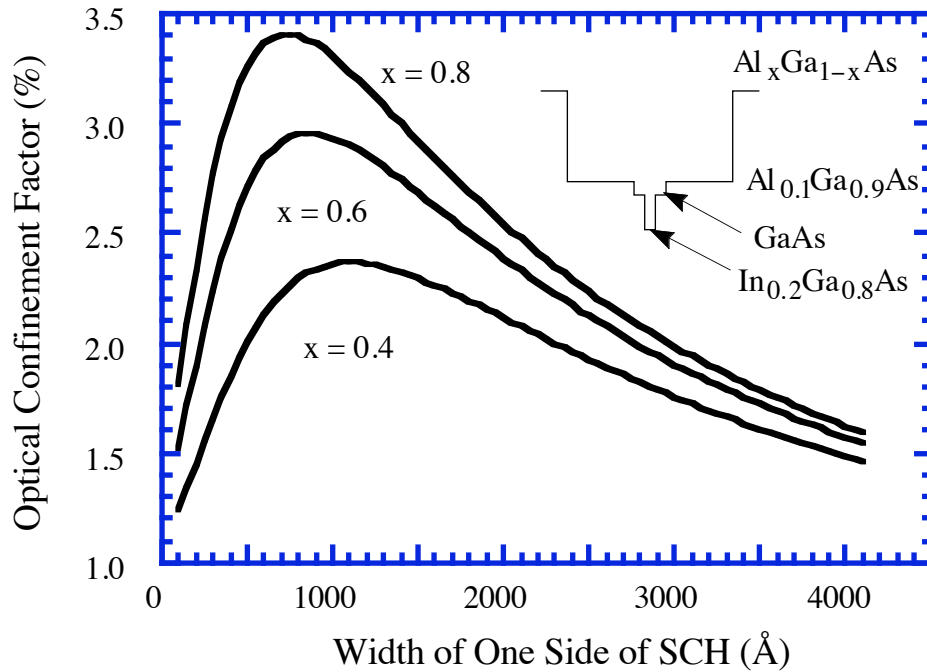


Fig. 5.3 Variation of the optical confinement factor with SCH width for an ungraded SCH profile described in Fig. 5.2. The curves refer to the different Aluminum mole fraction in the cladding region.

5.3 Optimization of the Quantum Well Width

In bulk lasers, the composition of the active area is usually determined by the emission wavelength requirements. In the case of quantum well active area, the operating wavelength is also additionally tuned by varying the well width. The upper limit to such a process may be set by the strain limit requirements.

The InGaAs used for the active layer is not lattice matched to GaAs. The lattice mismatch is accommodated as strain in the lattice, and there is an upper limit

to the thickness of the InGaAs active layer that may be grown before the layer relaxes and releases the strain. This critical thickness is a function of the amount of lattice mismatch (directly related to the In composition), and the amount of material that is grown over the strained layer to accommodate the strain [10]. For $\text{In}_{0.2}\text{Ga}_{0.8}\text{As}/\text{GaAs}$ laser structures with $1.3 \mu\text{m}$ of $\text{Al}_{0.2}\text{Ga}_{0.8}\text{As}$ upper and lower cladding regions, MQW structures with four quantum wells each 75 \AA thick with 80 \AA barriers have been successfully grown and tested [11]. This implies a total critical thickness of 300 \AA for the $\text{In}_{0.2}\text{Ga}_{0.8}\text{As}/\text{GaAs}$ system.

In the absence of any strict operating wavelength requirements and strain limits, the quantum well width may be optimized for maximum differential gain, and hence the largest modulation bandwidth.

One of the parameters that varies directly with quantum well width is the optical confinement factor. This may be maximized by using an ungraded SCH structure and optimizing its width. The result of such a computation is shown in Fig. 5.4. Also shown in Fig. 5.4 is the variation of the transparency carrier density. As the quantum well width varies, the form of the gain-carrier density relationship also changes. Qualitatively the gain-carrier density curves get steeper (higher differential gain), and shift to higher transparency carrier densities. The increase in differential gain is generally not dominant, and the net effect is that there is an increase in the threshold current density with a decrease in well width. This increase is pretty dramatic below the quantum well thicknesses of about 50 \AA for structures grown on substrates with a (100) orientation [12]. As seen from the calculation in Fig. 5.4, this also corresponds to the well width at which the transparency carrier density starts to

increase abruptly. Thus, the lower limit to the quantum well thickness is about 50 Å so as to keep the threshold current density within manageable limits.

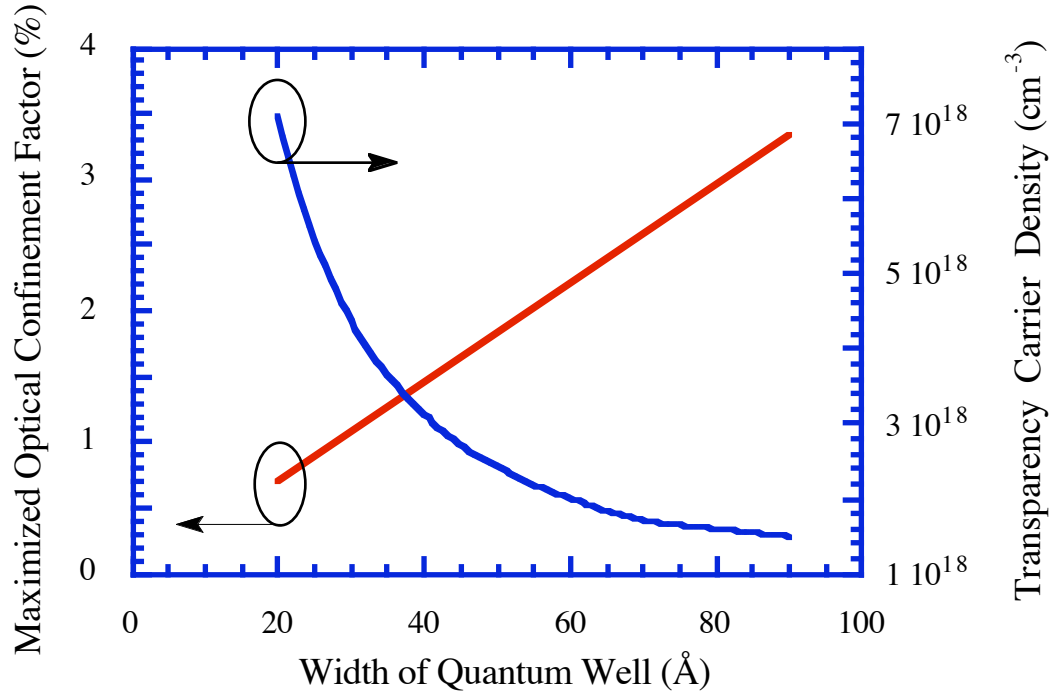


Fig. 5.4 Variation of the optical confinement factor and the transparency carrier density with quantum well width. The confinement factor is optimized for an ungraded SCH with 50 Å of GaAs smoothing layers and $\text{Al}_{0.6}\text{Ga}_{0.4}\text{As}$ cladding regions, as in Fig. 5.2.

The decreasing optical confinement factor (Fig. 5.4) with decreasing quantum well width also means an increase in the total gain required at threshold. Due to gain saturation in quantum well lasers, this also means a decrease in the differential gain. As pointed out earlier, the increase in differential gain which offsets this trend at smaller quantum well widths is not sufficiently large. Fig. 5.5 shows the variation in the differential gain with quantum well width for a modal gain of 40 cm^{-1} and 60 cm^{-1} . The differential gain is maximum at around the well width of 50 Å. Larger well

widths may be considered to minimize the operating current levels, as was done in this work, without sacrificing the differential gain too much. Quantum well width in the region of 50 Å to 80 Å is suitable for this purpose.

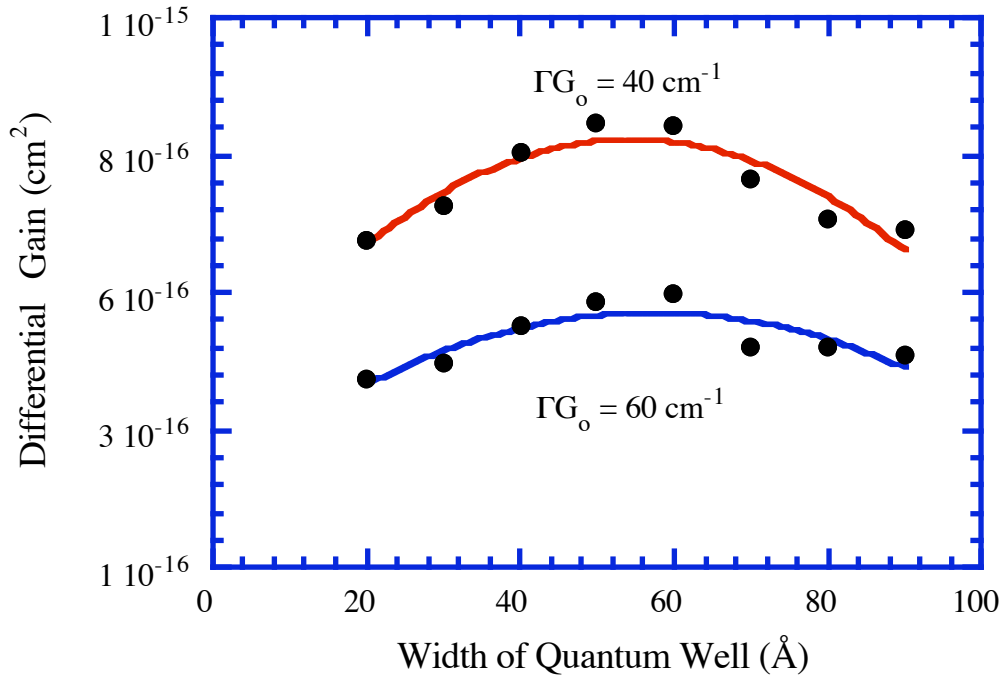


Fig. 5.5 Variation of differential gain with quantum well width plotted for the same active layer specifications as in Fig. 5.4. ΓG_0 refers to the modal gain for the particular plot. The full circles are computed points, and the lines have been drawn to show the trend in the data.

Using the spectral hole burning theory, some authors have computed the variation of the gain compression factor with the well width [13]. The figure of merit is then taken to be the ϵ/g_0 ratio which would maximize the K factor discussed in Chapter 3. The result of this computation also suggests an optimum quantum well width of about 80 Å to maximize the modulation bandwidth [13].

5.4 Optimization of the Barrier Width

Fig. 5.6 shows the modulation bandwidth dependence on the barrier width for the MQW case. In a MQW structure, the barriers must be of some minimum thickness to ensure that the carriers are two dimensionally confined to the quantum wells, and the inter-well coupling which leads to a broadening of the quantized energy levels is minimized. While taking advantage of the two dimensional confinement, one has to also ensure that carrier transport across the structure is not hampered leading to poor high speed performance. Further, the use of thick barriers, especially together with a large number of quantum wells, will result in carrier trapping leading to unequal carrier concentrations in the different wells.

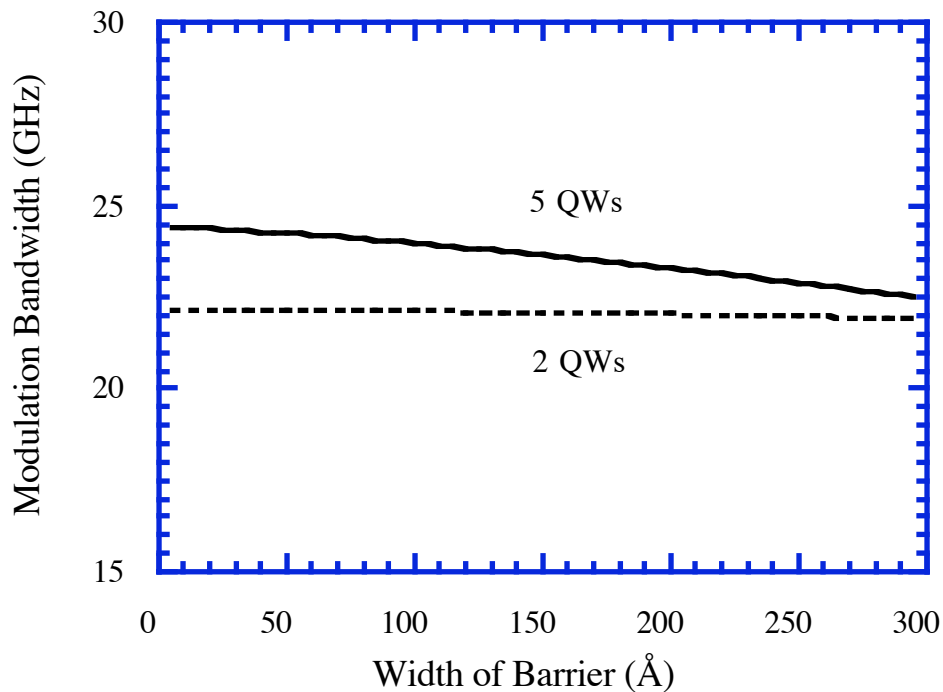


Fig. 5.6 Variation of modulation bandwidth, from transport considerations alone, as a function of the barrier thickness. This has been calculated for devices with 1000 Å SCH, 80 Å $\text{In}_{0.2}\text{Ga}_{0.8}\text{As}$ quantum well, and 2.5 μm ridge operating at 20 mW of output power.

Fig. 5.6 considers only the carrier transport effects, and thus clearly no minimum limit for the barrier width exists. Although there is some bandwidth penalty due to increasing barrier thickness, it is not very significant in the range considered here. This partly explains the success of high speed MQW structures with thick barriers [14,15].

5.5 Optimization of the Barrier Height/Carrier Confinement Potential

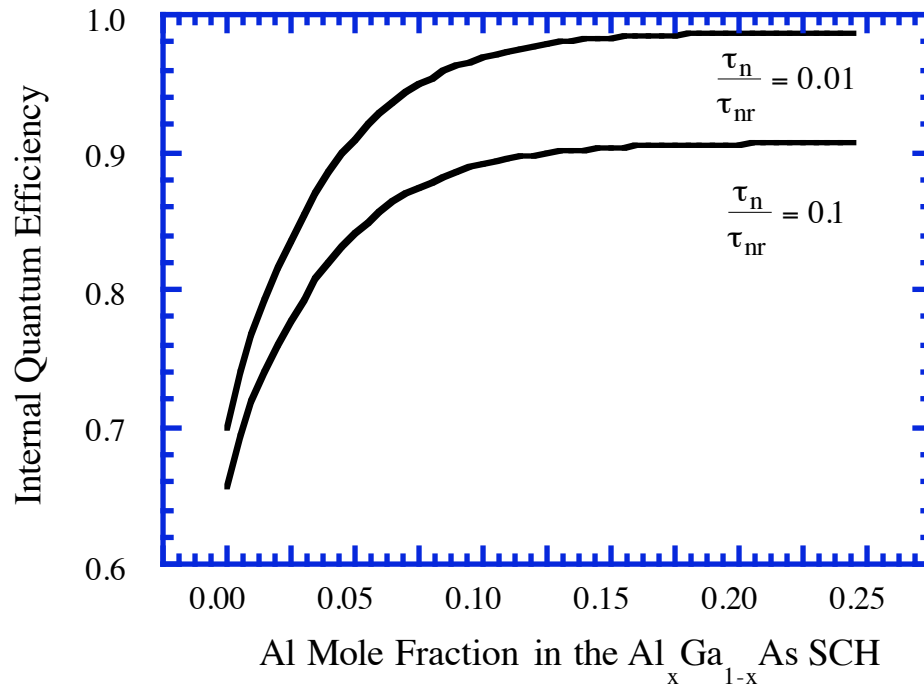


Fig. 5.7 Variation of internal quantum efficiency with Al mole fraction shown for two different values of nonradiative recombination times.

In SQW lasers, where the problem of carrier transport between quantum wells does not arise, thermionic emission time will have to be maximized in order to

minimize the value of χ . There is a limit to which one can increase the bandgap of the SCH layer to increase τ_e , before the resulting decrease in the optical confinement factor becomes unacceptable.

The barrier height in the SCH layer is optimized using the analysis for internal quantum efficiency presented in Chapter 4. Fig 5.7 shows the dependence of η_i on the Al mole fraction in the SCH layer for two different cases of nonradiative recombination times. A smaller nonradiative recombination time leads to a decrease in the maximum value for η_i , but the trend in the data with Al mole fraction remains unchanged. Since the transport factor, χ , is inversely related to η_i , maximizing η_i would minimize χ . From Fig. 5.7, it is evident that a minimum of 10 % Al is required in the AlGaAs SCH layer to avoid the detrimental effects of thermionic emission of carriers from the quantum well. The adverse effect on χ is also applicable to the case of MQW lasers, when one considers lowering the barrier height to facilitate carrier transport between the various quantum wells.

In the InGaAs/GaAs system, where carrier trapping in quantum wells is not as serious a problem as in the InGaAs/InP system, large bandwidth enhancements have been reported in MQW lasers with increased barrier heights [16]. A compromise in design can be achieved in MQW lasers by having a higher energy barrier between the first and the last quantum wells and the SCH layer, to minimize the overall χ , and a lower energy barrier between the quantum wells, to facilitate carrier transport [17,18].

5.6 Optimization of the Separate Confinement Heterostructure Width

The SCH width has to be optimized such that the optical confinement factor is maximized and the carrier transport time is minimized.

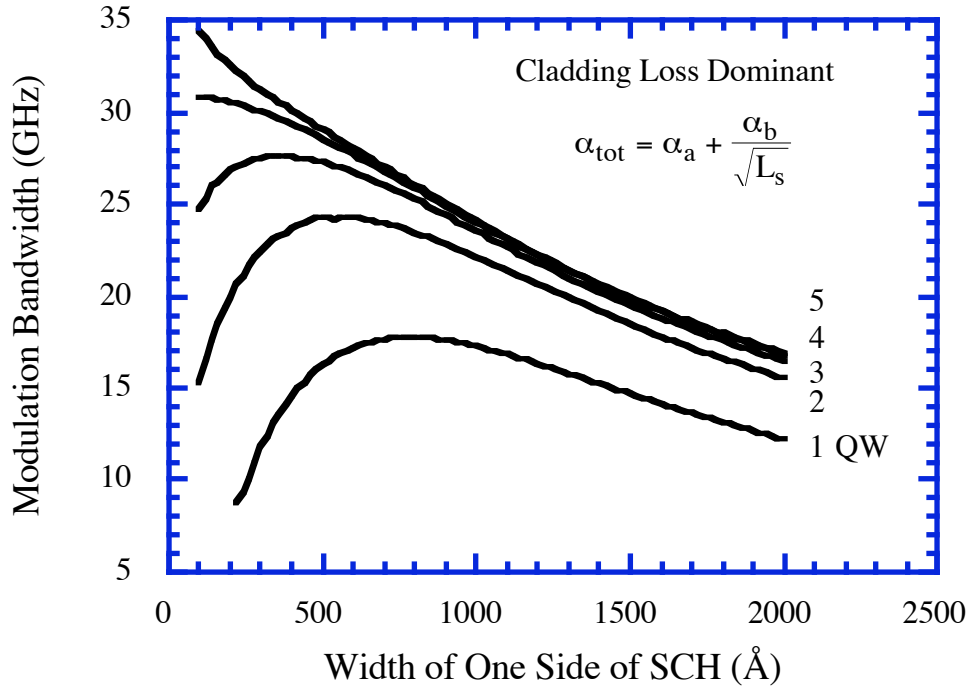


Fig. 5.8 Variation of modulation bandwidth with SCH width for the case when the cladding loss is dominant. This is calculated for devices with $300 \mu\text{m}$ cavity length, 80 \AA wide barriers, and other device parameters as specified for Fig. 5.6. The values for α_a and α_b in the expression given as the inset in the Fig. were obtained by fitting the internal loss variation with the SCH width for Samples A, B and C.

Figs 5.8 and 5.9 present two cases for the optimization of SCH widths. First is the case where the cladding loss is dominant. This is true in the case of Samples A, B and C where the total internal loss increased inversely with the square root of the SCH width.

Fig. 5.9 is a more typical case where the doping levels in the claddings are not very high, and consequently the loss in the active area dominates. In this case, the total internal loss can be written as a function of the optical confinement factor. This is true for Samples F and G.

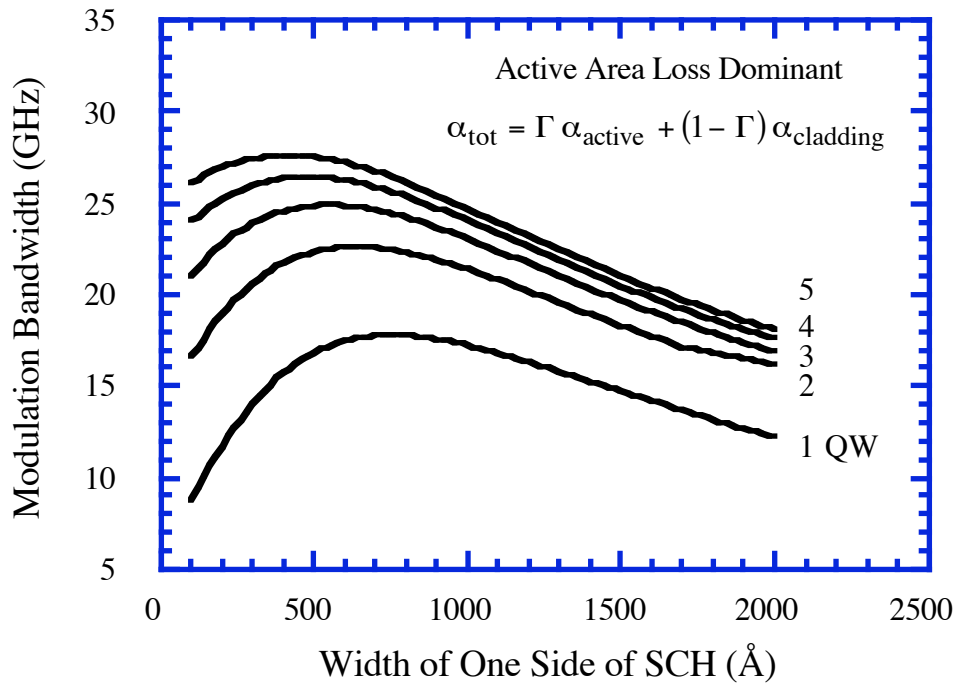


Fig. 5.9 Same plot as in Fig. 5.8 but for the case when the loss in the quantum well active area is dominant. The values for α_{active} and $\alpha_{cladding}$ are 124 cm^{-1} and 3.3 cm^{-1} respectively. These values were obtained by fitting the internal loss data for Samples F and G.

The functional relations for the total internal loss have been given as insets in the figures themselves. The various parameters in the relationships, α_a , α_b , α_{active} and $\alpha_{cladding}$ were experimentally determined. In both cases, there exists an optimum value of SCH width for maximum modulation bandwidth. The bandwidths are somewhat higher in Fig. 5.8, because the higher internal loss at narrow SCH widths also leads to a reduced photon lifetime which enhances the modulation performance. This enhancement comes at the expense of a larger operating current density, and thus the devices are more prone to the effects of thermal heating.

The SCH could be partly doped or doped all the way up to the quantum wells to help decrease the transport time. Depending on the doping level, this may increase

the internal loss considerably, leading to a reduction in the differential gain and an increase in the operating current density.

The optimum design for the SCH may be one in which the quantum well is placed asymmetrically in the structure, i.e. closer to the p cladding. This would minimize the hole transport time, and the width of the SCH on the n cladding side can then be optimized for maximum optical confinement factor. One drawback of this structure is the asymmetric optical mode pattern along the transverse direction.

5.7 Optimization of the Cavity Length

In quantum well lasers there exists an optimum cavity length for the maximum modulation bandwidth. This is quite unlike lasers with bulk active areas where shorter cavity lengths generally lead to larger modulation bandwidths due to the decrease in the photon lifetime. In quantum well lasers the differential gain is strongly carrier density dependent, and this works in opposition to the effects of a reduced photon lifetime. These tradeoffs are illustrated in Fig. 5.10, which shows the optimal cavity length for devices with a different number of quantum wells.

Generally, MQW lasers have a larger modulation bandwidth than SQW lasers, but the cavity length in the MQW case has to be sufficiently short to take full advantage of this. The optimal cavity length for the SQW case is $300\ \mu\text{m}$, and decreases to $60\ \mu\text{m}$ in the case of five quantum wells. The locus of the optimal cavity lengths is also indicated in Fig. 5.10. For three or more quantum wells the optimal cavity length is below $100\ \mu\text{m}$. It is difficult to cleave lasers below this limit, and one may have to resort to dry etching techniques to fabricate lasers with very short cavity lengths [14]. Further, lasers with short cavity lengths are more prone to thermal

heating, and may not perform as well as theoretically expected. To overcome this practical problem one may have to use MQW lasers with nonoptimal cavity lengths.

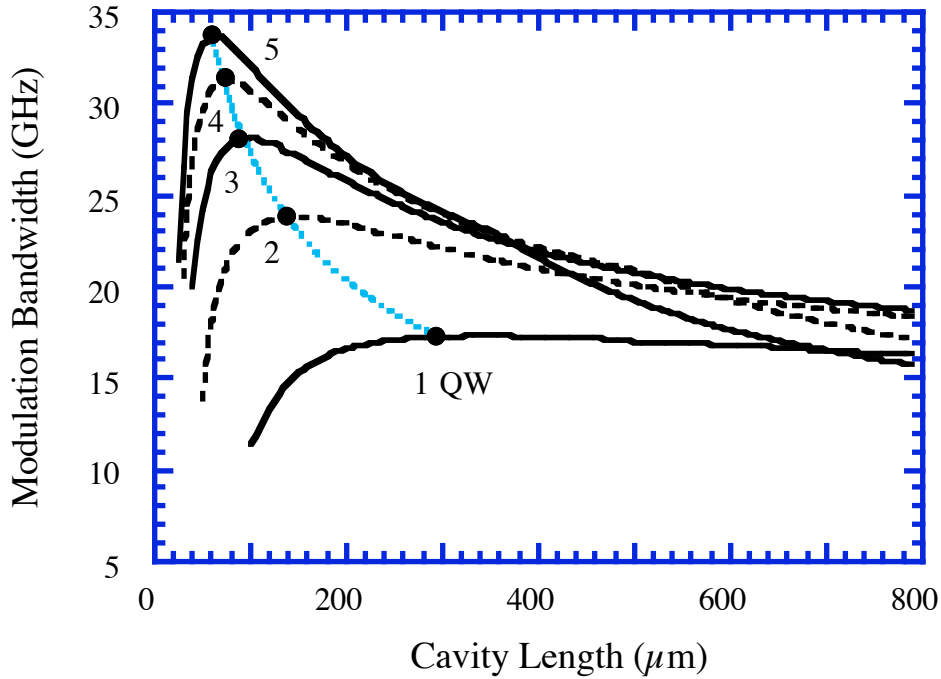


Fig. 5.10 Variation of modulation bandwidth as a function of cavity length. This has been calculated for the same devices parameters in Fig. 5.6. MQW lasers generally have a larger bandwidth than SQW lasers but are a lot more sensitive to cavity length variations.

5.8 Experimental Results

Fig. 5.11 shows the experimental variation in the -3 dB modulation bandwidth with SCH width at different power levels. These data are from Samples A, B and C. Here again the predictions of the analytic expression are very close to the results from the exact expression. The optimum SCH width also corresponds roughly to the point at which the optical confinement factor is a maximum. For a narrow SCH, the bandwidth drops off due to decreasing confinement factor resulting

in a larger threshold gain and thus a lower differential gain. At larger SCH widths, the combination of a decreasing confinement factor and increasing carrier transport time across the undoped regions of the SCH, limits the modulation bandwidth. At sufficiently high powers for wide SCH devices, the characteristic *drop* due to carrier transport appears in the modulation bandwidth curve.

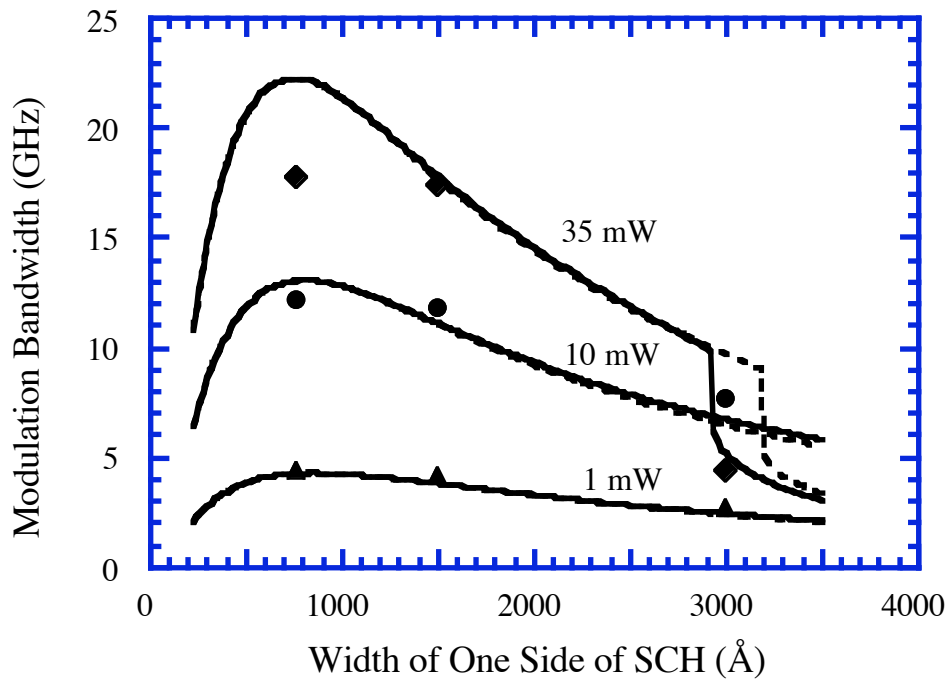


Fig. 5.11 Comparison of the calculated and measured variation in modulation bandwidth with SCH width. The dashed line is the result from the analytic solution and the bold line is that of the exact expression. The carrier transport effects dominate at sufficiently high power levels.

Fig. 5.12 shows the experimental and theoretical variation of modulation bandwidth with cavity length for SQW and MQW lasers. This data has been extracted from Samples F and G.

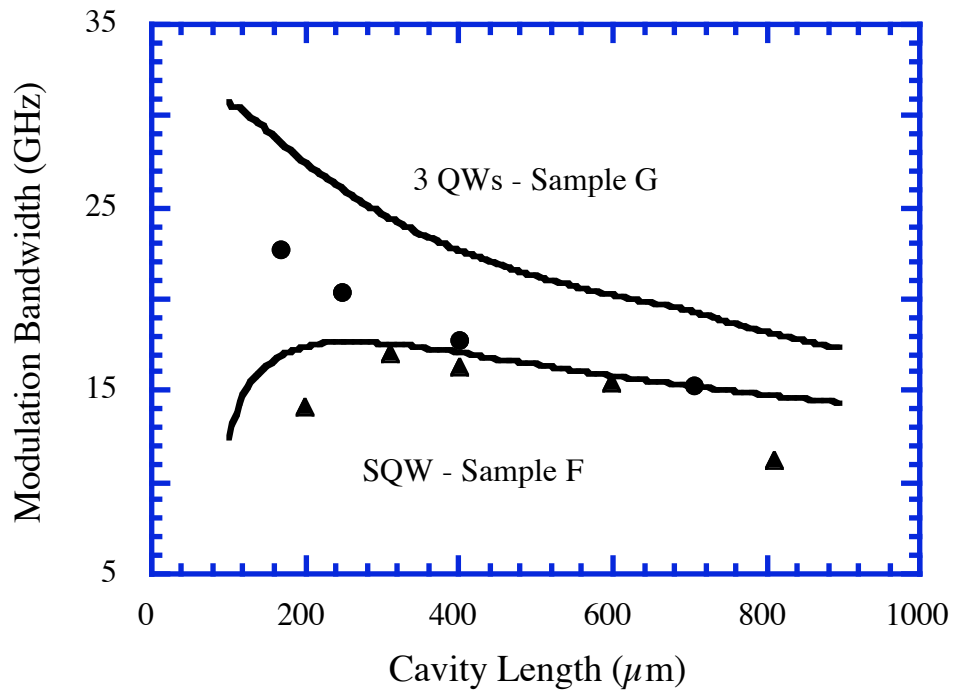


Fig. 5.12 Comparison of the calculated and measured variation in modulation bandwidth with cavity length for SQW and MQW lasers. The SQW lasers exhibit a broad maximum for the cavity length dependence of modulation bandwidth while MQW lasers are generally more sensitive to cavity length variations.

The parasitics were more significant in this set of devices, and the RC product was about 14.5 ps. The effects of the parasitics have been deconvolved from the experimental data presented in Fig. 5.12. As the cavity length is reduced, the threshold gain increases leading to a decrease in the differential gain. This is balanced by the reduction in the photon lifetime, and this results in an optimum cavity length for the maximum modulation bandwidth. The D factor [19], i.e. the slope of the resonance frequency variation with square root of optical power, gives a good indication of the maximum modulation bandwidth possible in the absence of severe

transport effects. Fig. 5.13 shows the variation of the D factor with cavity length for a 3 QW laser (Sample D) designed for minimal transport effects.

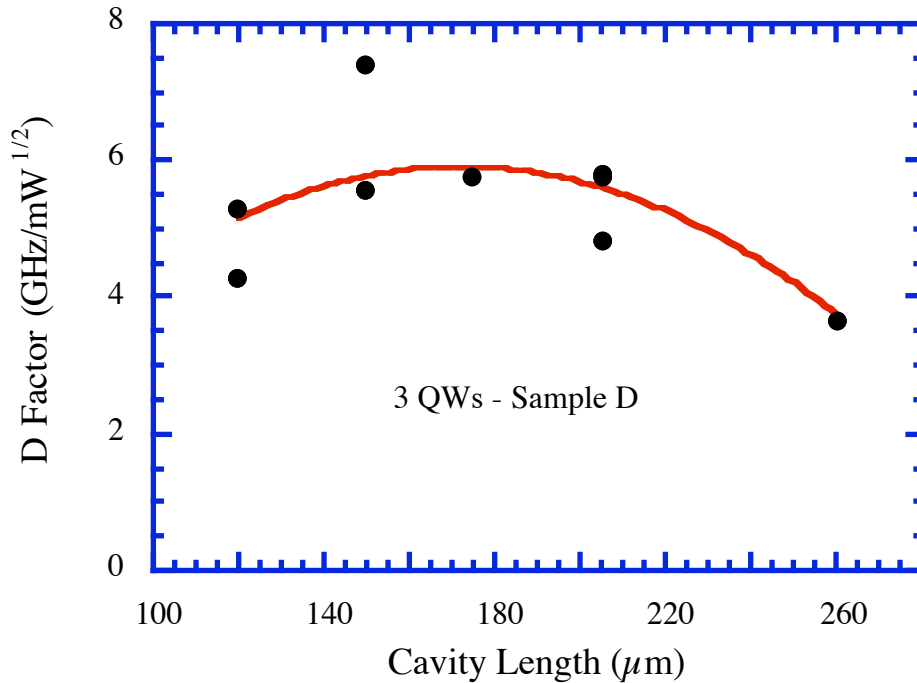


Fig. 5.13 Cavity length dependence of the D factor for a 3 QW sample. The bold line has been drawn to show the trend in the data.

As predicted earlier the optimum cavity length for a 3 QW sample is about $100 \mu\text{m}$. This is at the limit of what can be cleaved with reasonable yield in practice. Herein lies the practical advantage of a quantum well laser with a smaller number of wells; they can be easily fabricated for high speed applications. Further, longer cavity length lasers dissipate heat more efficiently, and therefore suffer less from the adverse effects of device heating.

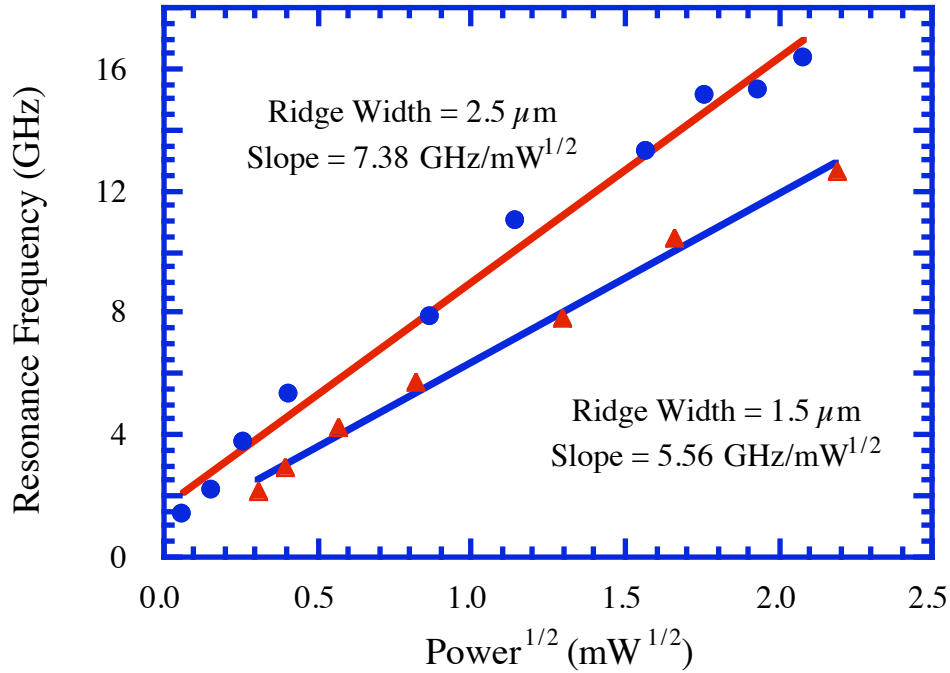


Fig. 5.14 Variation of resonance frequency with square root of power for two 150 μm cavity length 3 QW devices (Sample D) with different ridge widths.

Fig. 5.14 shows the variation of resonance frequency with square root of power for two 150 μm long 3 QW devices (Sample D) that differ only in the width of the ridge waveguide. One of the drawbacks of a ridge waveguide structure for high speed applications is the lateral carrier diffusion along the active area. This carrier diffusion is severe for wider ridges, and is known to introduce additional damping to the modulation response [20,21]. From Fig. 5.14, the device with a 2.5 μm wide ridge has a better response than one with a 1.5 μm wide ridge.

Lateral carrier diffusion is not the only concern when designing narrow ridge waveguide lasers. The loss of lateral confinement of the optical mode becomes severe for narrow ridges. This leads to an increase in the threshold current as the

ridge width is reduced below about $2 \mu\text{m}$ (see Fig. 6.8). Another area of concern is the poor thermal dissipation in narrow ridge waveguide lasers. These constraints lead to optimum ridge width of about $2.5 \mu\text{m}$ for the best modulation performance.

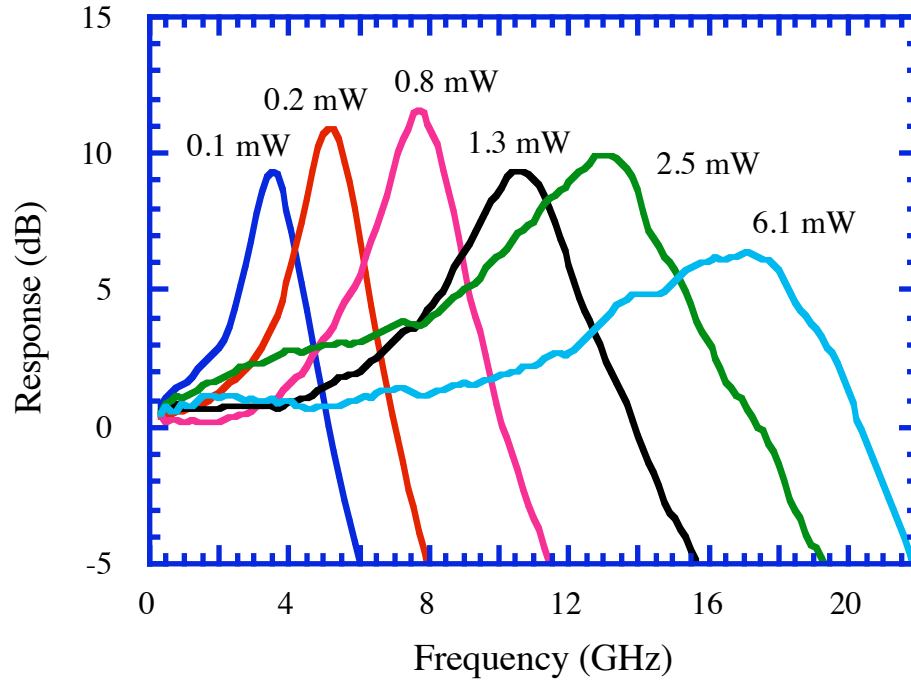


Fig. 5.15 Modulation response for a 3 QW sample with $150 \mu\text{m}$ cavity length, $2.5 \mu\text{m}$ ridge width and $\text{Al}_{0.15}\text{Ga}_{0.85}\text{As}$ SCH.

Fig. 5.15 shows the modulation response of the laser sample optimized using the model developed previously and the guidelines specified in this chapter. This device which has a $150 \mu\text{m}$ long cavity and a $2.5 \mu\text{m}$ wide ridge, is from Sample D which has 3 QWs and an $\text{Al}_{0.15}\text{Ga}_{0.85}\text{As}$ SCH. The maximum -3 dB modulation bandwidth is about 22 GHz. The device is presently thermally limited. The performance can be improved by having a lower internal loss in the material (see

Appendix A) which would lead to better external quantum efficiencies, and larger output powers at lower operating current levels.

One of the parameters that is significant, but not deliberately considered in the design process is the gain compression factor, ϵ . The possible physical origins of this factor was discussed in Chapter 1. Despite theoretical predictions that ϵ is enhanced in quantum well lasers, and further enhanced by the presence of strain, recent experimental evidence, reviewed in Chapter 1, suggests to the contrary.

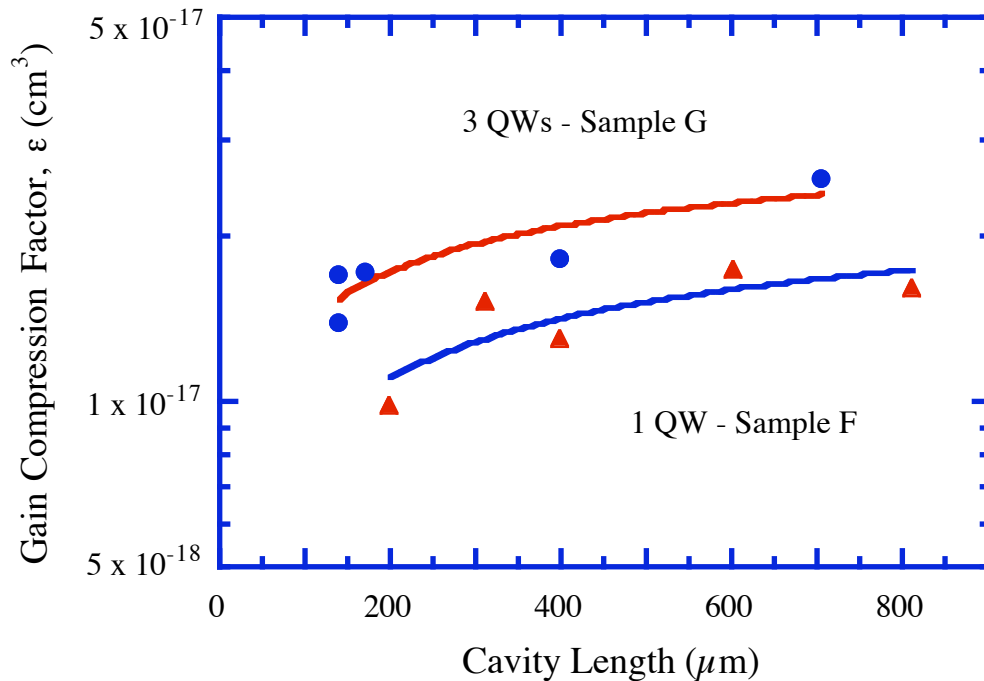


Fig. 5.16 Variation of the gain compression factor with cavity length for MQW and SQW lasers. The lines have been drawn to show the trend in the data.

The experimental data presented in Fig. 3.7 shows that the gain compression factor did not vary significantly with the SCH width. The carrier transport model that

was proposed did not influence ϵ at all. Fig. 5.16 shows the experimental variation of the gain compression factor with cavity length for SQW and MQW lasers [22]. The gain compression factor is lower for shorter cavity lasers and lasers with smaller number of wells. In this case the lowest value of ϵ was for a SQW laser of 200 μm cavity length. This value of $9.98 \times 10^{-18} \text{ cm}^{-3}$ is about 5 to 6 times lower than the values reported for MQW lasers operating at around 1.55 μm wavelength [24-29].

The higher values of gain compression for MQW lasers and lasers with longer cavity lengths indicate that this nonlinearity is enhanced by increasing the quantum confinement of the carriers. These trends are in *qualitative* agreement with the predictions reported previously, although this theoretical work predicts an overall increase in the gain compression factor for the case of quantum well lasers compared to the bulk ones [28], which we have not observed in our experiments.

References

1. C. B. Su, and V. Lanzisera, "Effect of Doping Level on the Gain Constant and Modulation Bandwidth of InGaAsP Semiconductor Lasers," *Appl. Phys. Lett.*, vol. 45, pp. 1302-1304, 1984.
2. W. -H. Cheng, K. -D Buehring, A. Appelbaum, D. Renner, S. Chin, C. B. Su, A. Mar, and J. E. Bowers, "High-Speed and Low-Relative-Intensity Noise 1.3 μm InGaAsP Semi-Insulating Buried Crescent Laser," *J. Quantum Electron.*, vol. 27, pp. 1642-1647, 1991.
3. Y. Arakawa, and A. Yariv, "Quantum Well Lasers-Gain, Spectra, Dynamics," *J. Quantum Electron.*, vol. 22, pp. 1887-1899, 1986.
4. S. W. Corzine, R. H. Yan, and L. A. Coldren, "Theoretical Gain in Strained InGaAs/ AlGaAs Quantum Wells Including Valence-Band Mixing Effects," *Appl. Phys. Lett.*, vol. 57, pp. 2835-2837, 1990.
5. I. Suemune, "Theoretical Study of Differential Gain in Strained Quantum Well Structures," *J. Quantum Electron.*, vol. 27, pp. 1149-1159, 1991.
6. L. F. Lester, S. D. Offsey, B. K. Ridley, W. J. Schaff, B. A. Foreman, and L. F. Eastman, "Comparison of the Theoretical and Experimental Differential Gain in Strained Layer InGaAs/GaAs Quantum Well Lasers," *Appl. Phys. Lett.*, vol. 59, pp. 1162-1164, 1991.
7. K. Uomi, T. Mishima, and N. Chinone "Modulation-Doped Multi-Quantum Well (MD-MQW) Lasers. II. Experiment," *Jpn. J. Appl. Phys.*, vol. 29, pp. 88-94, 1990.
8. M. Asada, Y. Miyamoto, and Y. Suematsu, "Gain and the Threshold of Three-Dimensional Quantum-Box Lasers," *J. Quantum Electron.*, vol. 22, pp. 1915-1921, 1986.
9. I-H. Tan, G. L. Snider, L. D. Chang, and E. L. Hu, "A Self-Consistent Solution of Schrödinger-Poisson Equations Using a Nonuniform Mesh," *J. Appl. Phys.*, vol. 68, pp. 4071-4076, 1990.

10. G. A. Vawter, and D. R. Myers, "Useful Design Relationships for the Engineering of Thermodynamically Stable Strained-Layer Structures," *J. Appl. Phys.*, vol. 65, pp. 4769-4773, 1990.
11. C. Shieh, H. Lee, J. Mantz, D. Ackley, and R. Engelmann, "Critical Thickness in Strained-Layer GaInAs/GaAs Quantum Well Laser," *Electron. Lett.*, vol. 25, pp. 1226-1228, 1989.
12. T. Hayakawa, T. Suyama, K. Takahashi, M. Kondo, S. Yamamoto, and T. Hijikata, "Near-Ideal Low Threshold Behavior in (111) Oriented GaAs/AlGaAs Quantum Well Lasers," *Appl. Phys. Lett.*, vol. 52, pp. 339-341, 1988.
13. K. Uomi, and N. Chinone, "Proposal on Reducing the Damping Constant in Semiconductor Lasers by Using Quantum Well Structures," *Jpn. J. Appl. Phys.*, vol. 28, pp. L1424-L1425, 1989.
14. S. D. Offsey, L. F. Lester, W. J. Schaff, and L. F. Eastman, "High-Speed Modulation of Strained-Layer InGaAs-GaAs-AlGaAs Ridge Waveguide Multiple Quantum Well Lasers," *Appl. Phys. Lett.*, vol. 58, pp. 2336-2338, 1991.
15. L. F. Lester, W. J. Schaff, X. Song, and L. F. Eastman, "Optical and RF Characteristics of Short-Cavity-Length Multiquantum-Well Strained-Layer Lasers," *Photon. Tech. Lett.*, vol. 3, pp. 1049-1051, 1991.
16. L. F. Lester, D. Teng, W. J. Schaff, and L. F. Eastman, "Design of Quantum Well Lasers for High Differential Gain," in *Conf. Dig. LEOS '91 Annual Meeting*, 1991, p. 86.
17. R. Nagarajan, T. Fukushima, J. E. Bowers, R. S. Geels, and L. A. Coldren, "High-Speed InGaAs/GaAs Strained Multiple Quantum Well Lasers with Low Damping," *Appl. Phys. Lett.*, vol. 58, pp. 2326-2328, 1991.
18. R. Nagarajan, R. P. Mirin, T. E. Reynolds, and J. E. Bowers, "Effect of the Confinement Layer Composition on the Internal Quantum Efficiency and Modulation Response of Quantum Well Lasers," *Photon. Tech. Lett.*, August 1992.

19. J. E. Bowers, B. R. Hemenway, A. H. Gnauck, and D. P. Wilt, "High-Speed InGaAsP Constricted-Mesa Lasers," *J. Quantum Electron.*, vol. 22, pp. 833-844, 1986.
20. N. Chinone, K. Aiki, M. Nakamura, and R. Ito, "Effects of Lateral Mode and Carrier Density Profile on Dynamic Behaviors of Semiconductor Lasers," *J. Quantum Electron.*, vol. 14, pp. 625-631, 1978.
21. D. Wilt, K. Y. Lau, and A. Yariv, "The Effect of Lateral Carrier Diffusion on the Modulation Response of a Semiconductor Laser," *J. Appl. Phys.*, vol. 52, pp. 4970-4974, 1981.
22. R. Nagarajan, T. Fukushima, J. E. Bowers, R. S. Geels, and L. A. Coldren, "Single Quantum Well Strained InGaAs/GaAs Lasers with Large Modulation Bandwidth and Low Damping," *Electron. Lett.*, vol. 27, pp. 1058-1059, 1991.
23. W. F. Sharfin, J. Schlafer, W. Rideout, B. Elman, R. B. Lauer, J. LaCourse, and F. D. Crawford, "Anomalously High Damping in Strained InGaAs-GaAs Single Quantum Well Laser," *Photon. Tech. Lett.*, vol. 3, pp. 193-195, 1991.
24. L. D. Westbrook, N. C. Fletcher, D. M. Cooper, M. Stevenson, and P. C. Spurdens, "Intensity Noise in $1.5\mu\text{m}$ GaInAs Quantum Well Buried Heterostructure Lasers," *Electron. Lett.*, vol. 25, pp. 1183-1184, 1989.
25. M. Kitamura, "1.5 μm Multiple Quantum Well Distributed Feedback Laser Diodes grown by MOVPE," *7th International Conference on Integrated Optics and Optical Fiber Communication '89*, Kobe, 1989, paper 19C1-5.
26. K. Uomi, T. Tsuchiya, M. Aoki, and N. Chinone, "Oscillation Wavelength and Laser Structure Dependence of Nonlinear Damping Effect in Semiconductor Laser," *Appl. Phys. Lett.*, vol. 58, pp. 675-677, 1991.
27. T. Fukushima, J. E. Bowers, R. A. Logan, T. Tanbun-Ek, and H. Temkin, "Effect of Strain on the Resonant Frequency and Damping Factor in InGaAs/InP Multiple Quantum Well Lasers," *Appl. Phys. Lett.*, vol. 58, pp. 1244-1246, 1991.

28. T. Takahashi, and Y. Arakawa, "Effect of Nonlinear Gain on Modulation Dynamics in Quantum Well Lasers," *Electron. Lett.*, vol. 25, pp. 169-170, 1989.

CHAPTER 6

DEVICE FABRICATION

6.1 Broad Area Lasers

Broad area lasers are fabricated to evaluate the quality of the laser material. The broad area threshold current density is a good indication of the material quality and the epitaxial layer design. In addition, the data for internal quantum efficiency and internal loss can also be extracted from broad area measurements.

The normal broad area lasers have large dimensions and are gain guided. Although these are easy to fabricate, the drawback is that they do not provide accurate data on threshold current density due to carrier diffusion. The carrier diffusion can be significant if the resistance of the epitaxial layers between the cap layer, on which the contact is deposited, and the active layer is low. This causes an active area wider than the stripe width to be pumped, leading to an overestimation of the threshold current density. To prevent this ridge waveguide lasers with fairly wide ridges are fabricated for broad area lasers.

A self aligned process is used to fabricate the broad area lasers. The process used to fabricate the broad area devices corresponds to the first two steps in the fabrication of the polyimide buried ridge waveguide lasers (Fig. 6.3). The *p*-metal sequence is first deposited on the epitaxial cap layer using lift-off. This contact metal sequence consists of Cr/Pd/Zn/Pd/Cr/Au/Ni with the respective thicknesses of 50 Å/125 Å/50 Å/250 Å/50 Å/1200 Å/300 Å. The first Cr layer is used to improve

the adhesion of the contact metal to the semiconductor surface. The thermal evaporator can handle only a maximum of three different source materials during one run, and therefore this metal sequence is deposited in two consecutive runs. In the first run Cr/Pd/Zn/Pd is deposited and the evaporator is opened with the Pd layer exposed. To ensure good adhesion of the subsequent Au and Ni layers, the second intermediate Cr layer is used. The final Ni layer is the mask for the subsequent Cl_2 reactive ion etching (RIE) step used for the fabrication of the self aligned ridges.

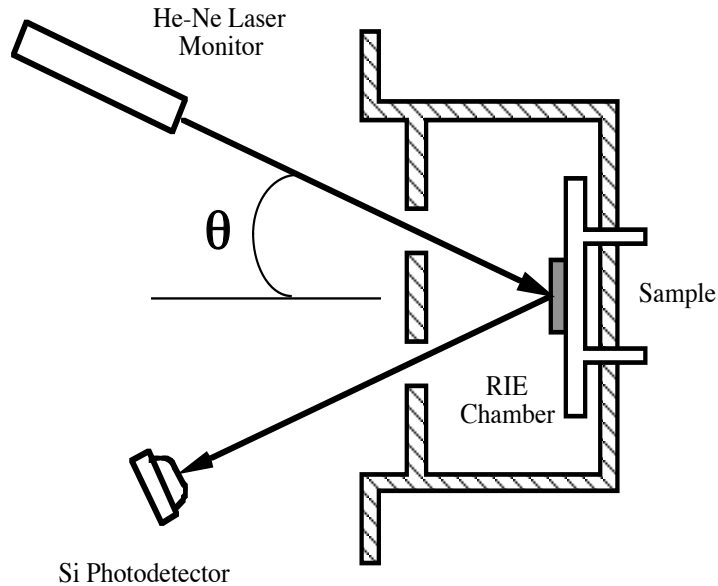


Fig. 6.1 Schematic diagram of the RIE system and the laser reflectivity measurement setup.

The schematic diagram of the RIE system is shown in Fig. 6.1. The Cl_2 RIE system uses a 13.56 MHz radio frequency (RF) power supply. The sample is attached to the a 6 inch Si wafer using a high vacuum compatible, and thermally and electrical

conductive paste, similar to the one typically used to attach samples to the holders in the scanning electron microscopes (SEM) [1]. The Si wafer is similarly attached to one of the electrodes, which is water cooled.

The RIE machine also has a reflectivity measurement setup based on the 633 nm He-Ne laser to accurately monitor the etch depth. The laser beam is directed at the sample through a quartz viewport (a series of holes covered with a quartz window) in the grounded electrode at the rear of the chamber. The light reflects off the sample and is monitored with a Si photodetector.

The He-Ne wavelength is barely absorbed by $\text{Al}_{0.5}\text{Ga}_{0.5}\text{As}$, and any epitaxial layer with a higher Al composition is transparent. The various layers of the sample permit light propagation to different extents, and have correspondingly different delays. The reflected signal varies in intensity as the etch proceeds, because the relative phase delay between light reflected at the different interfaces varies as the thickness of the top layer decreases with time. For a given azimuthal angle, θ , of the incident He-Ne beam, the reflected beam intensity can be calculated if the refractive index and the absorption of the various layers at He-Ne wavelength are known [2].

Fig. 6.2 shows the calculated and experimental variation of the reflected He-Ne signal with etch depth. The equivalent layer thickness information is obtained from the growth calibration during the molecular beam epitaxy (MBE) growth. There is fairly good agreement between the calculated ($\theta = 20^\circ$) and the experimentally observed reflected signals. Some of the discrepancy is due to variations in the value of θ , and the lack of accurate refractive index and absorption values in the AlGaAs system at He-Ne wavelength. Using the calculated signal variation as a guide, the etch depth is determined by observing the experimental signal in real time. The etch

is stopped once the required depth is reached. This is an accurate and reproducible way to etch ridges using dry etching techniques without having to use stop etch layers as an intrinsic part of the epitaxial layer design.

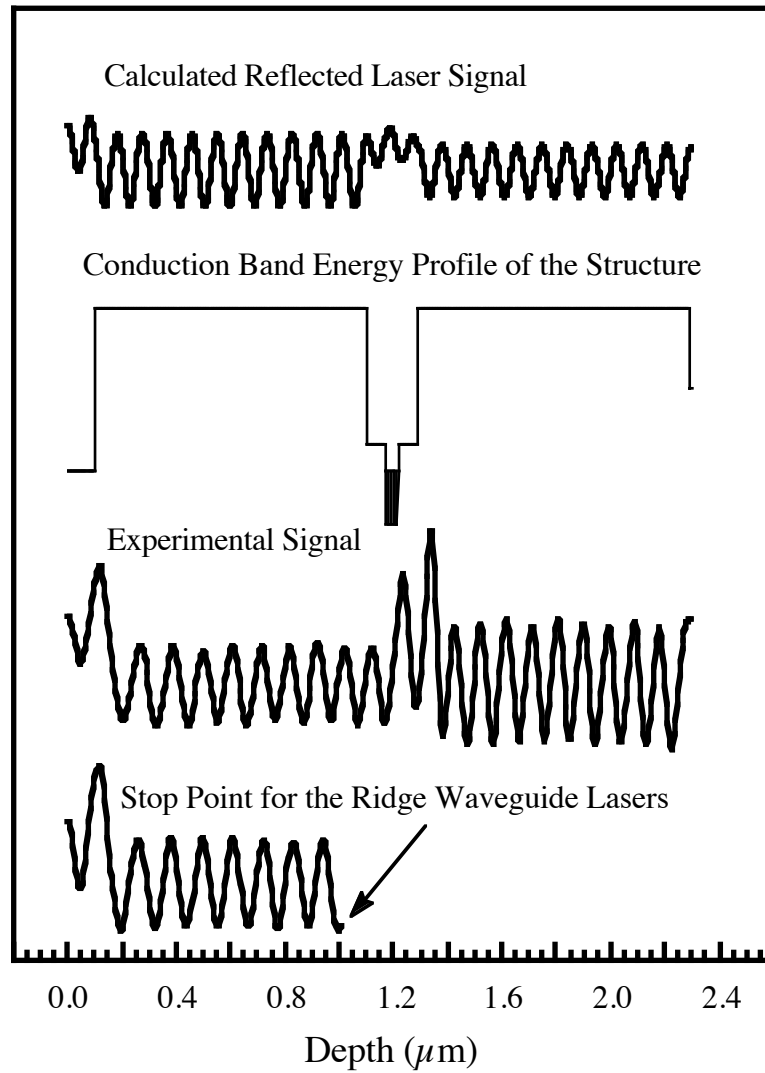


Fig. 6.2 Variation of the reflected laser signal from the sample with time, plotted with respect to the equivalent etch depth.

The RIE system has a load lock which is evacuated to about 2 mTorr using a liquid N₂ absorption pump before the sample is inserted into the high vacuum chamber. The high vacuum chamber is evacuated by a turbomolecular pump. The background pressure is typically $< 5 \times 10^{-7}$ Torr before the start of the etch. The Cl₂ flow rate is set at 4 sccm, and the chamber pressure at 0.8 mTorr for the etch. The electrodes are biased at a level (about 400 V) suitable for a forward power of 60 W, and the RF matching network is tuned for minimal reflected power. The etch rate is typically 1200 Å/min.

The last laser reflectivity signal in Fig. 6.2 shows the depth to which the ridge waveguide lasers are typically etched. The etch is stopped in the high Al (typically 60 % to 70 %) *p*-cladding AlGaAs region. The active layer is not etched here as well as in the case of narrow ridge waveguide lasers later.

Etching past the active layer will provide better current confinement leading to a lower threshold current, and minimize the adverse effects of lateral carrier diffusion on the damping of high speed lasers (Section 5.8). The polyimide material used in the planarization of the narrow ridge waveguide structure has poor thermal dissipation characteristics. The active area *buried* in this material will heat up at a much faster rate compared to the case where it is not etched, and is surrounded by the epitaxial semiconductor material. This will result in poor device characteristics at high bias levels used in the modulation experiments. Further, due to the high surface recombination velocity in the GaAs material system (Section 2.10), the injected carriers will easily recombine at etched active layer surface resulting in enhanced leakage currents. Additionally, defects are also easily formed at the etched active layer surface. These defects then propagate throughout the active layer, and act as

nonradiative recombination centers. This leads to a complete degradation in the light output from the laser.

The dry etched sample is then *slightly* wet etched to remove any possible damage from the Cl₂ RIE. The wet etchant used is a combination of Br water (saturated solution of Br in water at 20 °C), 49 % HBr and water in the 1:2:1 ratio by volume. The samples are typically immersed for 15 s in the etchant. This etches an additional 400 Å to 700 Å of material depending on the composition of the cladding region. Layers with higher Al composition have a faster etch rate in this reagent. The bonus of using this etchant is that it also etches off the remaining Ni mask layer. This is especially useful as Ni tends to *ball up* (roughen the surface) in the subsequent annealing step.

The *p*-contacts are then alloyed by annealing in forming gas (about 10 % H₂ in N₂ mixture) in a rapid thermal annealer (RTA) at 420 °C for about 20 s. A temperature ramp rate of 40 °C/s is used. A break point is inserted at 300 °C for 30 s to allow the temperature to become uniform over the sample, and complete any outgassing that may occur from the sample during the annealing.

The sample is then mechanically thinned so that it can be cleaved into bars and tested. The sample is first lapped using a 5 μm aluminum oxide powder [3]. The GaAs substrates are initially about 400 μm thick. The substrates are lapped down to about 100 μm in thickness. The grain size of the aluminum oxide powder is then switched to 1 μm, and backside surface is finally lapped off to a fairly smooth finish. The final substrate thickness is below 90 μm.

The backside surface is cleaned, and the substrate metallization is deposited. An *n*-metal sequence of Ni/AuGe/Ni/Au of 50 Å/1000 Å/150 Å/1500 Å thickness is

deposited. The n -contact is then annealed as previously at 380 °C for about 15 s. The same temperature ramp and break point are used. A lower annealing temperature is deliberately chosen so as to not over anneal the previously alloyed p -contact, and further, annealing temperatures below 400 °C is sufficient to obtain good contact resistance. This also ensures a good surface morphology.

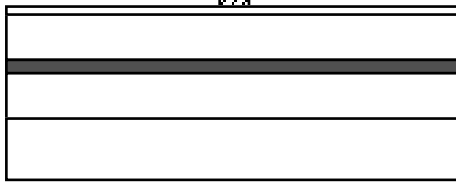
The sample is then cleaved into bars and pulse tested to determine the L/I characteristics.

6.2 Self Aligned Polyimide Buried Ridge Waveguide Lasers

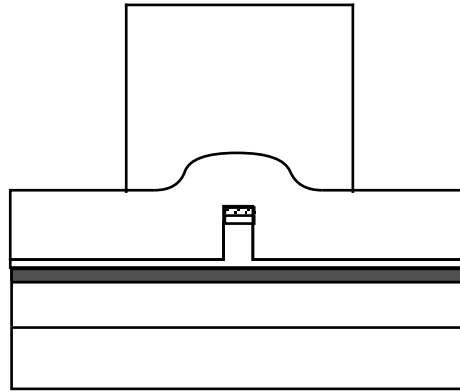
The narrow ridge waveguide devices are fabricated in a similar fashion. The first two steps of the broad area laser fabrication are repeated except that the width of the ridges is much reduced. The complete sequence of the fabrication process is given in Fig. 6.3.

The main difference here is that the ridges are too narrow to be probed or bonded to directly. For these devices to function at high speeds, contact pads would have to be fabricated with a minimal addition of parasitic capacitance. A typical way is to use a SiO₂ dielectric layer, and deposit the contacts on them. It is difficult to grow thick layers of SiO₂ uniformly, and also this process does not planarize the etched surface, which is essential to avoid breakage in the deposited metal films.

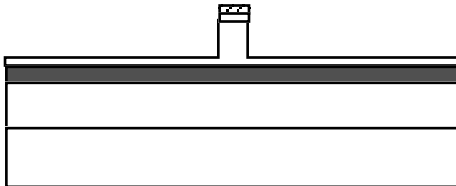
A preferable way is to deposit the bonding pads over a layer of polyimide. This material is easily spun on to any desired thickness by an appropriate choice of the polyimide type and/or the spin speed. Further, this material also has a lower dielectric constant compared to SiO₂. This is the method that is used here, and hence the name *polyimide buried* for the resulting laser structure.



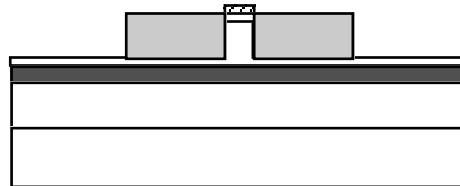
First Mask Step
1. Lift-Off *p*-Metal



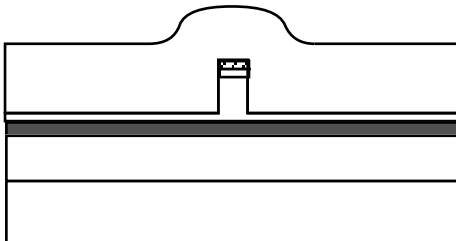
Second Mask Step
7. Spin on a thick photoresist and pattern it to produce a planar surface



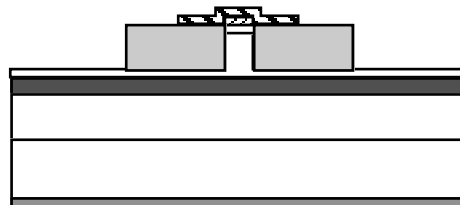
2. Chlorine RIE to form the ridges
3. Use wet etch to remove RIE damage



8. Oxygen RIE of polyimide using photoresist as the planarizing mask



4. Anneal the contacts
5. Spin-on the polyimide
6. Cure the polyimide



Third Mask Step
9. Deposit Au over the *p*-contact for bonding and probing
10. Lap the substrate
11. Deposit *n*-metal contact on the substrate side

Fig. 6.3 Process steps for the fabrication of the self-aligned polyimide buried ridge waveguide lasers.

After the *p*-contact is annealed, a thick layer of polyimide (Probimide™ 284 [4]) is spun on and cured. A spin speed of 5000 rpm is used, and the resulting film is about 1.2 μm thick. The ridge waveguides are less than 1 μm in height, and the polyimide completely covers the ridges. This particular type of polyimide is fully imidized, and does not shrink during the subsequent thermal processing. The glass transition temperature of this polyimide is 320 °C, above which crosslinking of the polymer occurs, and the compound becomes very stable. QZ 3289 adhesion promoter concentrate [4] diluted 1 to 9 with QZ 3290 diluent [4] is first spun on at 5000 rpm before the polyimide. The polyimide coated sample is then baked at 90 °C for 30 min., then at 150 °C for 15 min., followed by 240 °C for 15 min. and finally at 325 °C for 1 hr. The last two curing steps are done on a strip heater in a N_2 environment.

During the curing process, it is important to remember that the *p*-contact used for the self aligned process is also being annealed albeit at a lower temperature. The depth to which the contact material diffuses (for diffusion from a limited source) into the semiconductor has an exponential dependence on temperature and a square root dependence on time [5]. The final curing temperature is kept lower than the initial annealing temperature of the contact, and the activation energy of diffusion for most materials in GaAs is in excess of 1 eV. Thus, the additional drive-in of the contact is negligible even though the sample is being heated at an elevated temperature for 1 hr.

The sample surface is only partially planarized after this polyimide step. A quantity called the degree of planarization, DOP, can be defined to describe the level of planarity achieved after curing. The definition of DOP is shown in the schematic diagram given in Fig. 6.4 [6]. This index varies from 0, for no planarization at all, to 1 when there is complete planarization. The DOP depends on the viscosity of the

polyimide [7]. For Probimide™ 284 as used in this process, DOP factor of about 0.5 is achieved for a single coat application. For a more complete planarization multiple coatings of the polyimide may be used.

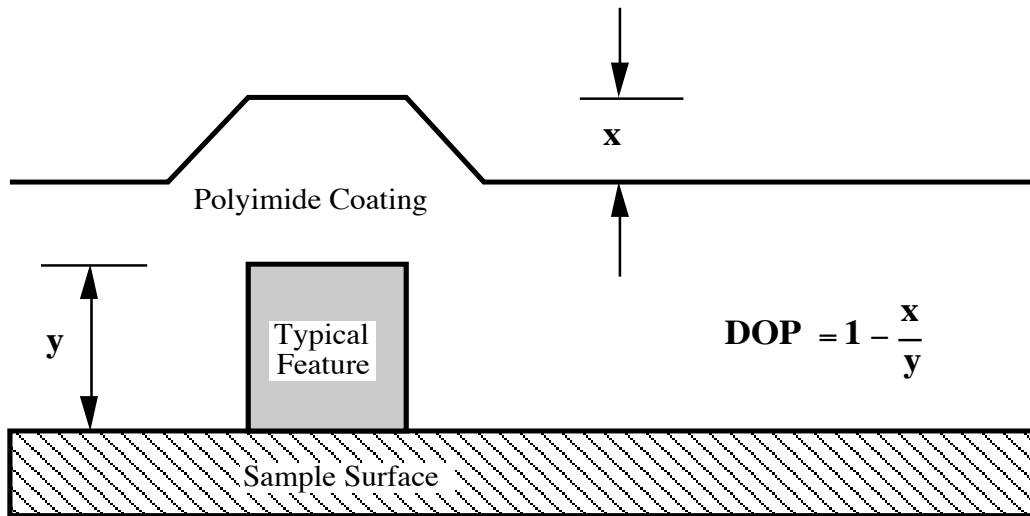


Fig. 6.4 Definition of the degree of planarization in the polyimide process.

Since the average thickness of the polyimide, after a single coating, is larger than the typical height of the ridges, planarization can also be achieved by an application of a thick photoresist mask layer and subsequent dry etching of the combination in O_2 . The next step is to etch the polyimide such that the self aligned p -contact is exposed while a planar surface is obtained adjacent to the ridge, on which the bond pad may be deposited. This is done by first spinning on a thick layer of photoresist (AZ 4330 [8]) at 5000 rpm, and patterning it over the required area as shown in Fig. 6.3. The spin on thickness of the photoresist is in excess of $3 \mu m$, and the resulting sample surface is almost planar.

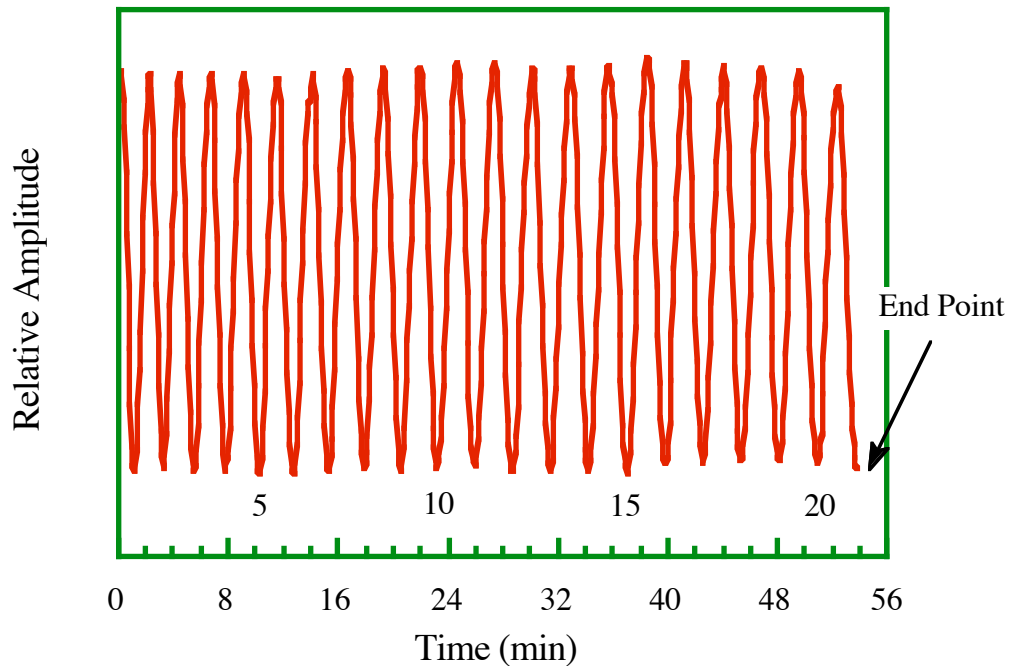


Fig. 6.5 Variation of the reflected laser signal with time from a test piece for the O₂ etching of polyimide with a photoresist mask.

The sample is then dry etched in O₂, and the progress of the etch is monitored, as previously, using the He-Ne laser monitoring system. The reflected He-Ne signal monitored during the etch from a test piece with identical polyimide and photoresist layers on it is given in Fig. 6.5. The background pressure is not critical for this etch, and is typically about 10⁻⁶ Torr before the start of the etch. The O₂ flow rate is set at 7 sccm, and the chamber pressure at 10 mTorr for the etch. The electrodes are biased at about 350 V, which is required for a forward power of 60 W, and the RF matching network is tuned for minimal reflected power. The photoresist and polyimide etch at about the same rate in O₂. This can be seen from the evenly spaced time variation in the reflection spectra. The even etch rate of the photoresist mask and the polyimide

layer results in a planar surface when the self aligned contacts are exposed. By the end of the etch all the photoresist has been removed, and only the polyimide remains. The endpoint is detected by counting the number of fringes.

The etch typically takes 21 periods of the reflected signal to complete. After this the height variation on the sample surface is carefully measured to check if all the polyimide has been removed from the top of the ridges. Sometimes additional etching is required, and this can be conveniently done using a O_2 plasma etcher which operates at a lower RF frequency (30 kHz) and at a higher background pressure (300 mTorr). The etching characteristics of the plasma etcher are far less anisotropic than that of the RIE system, but it is not a problem when only a minimal amount of polyimide has to be removed.

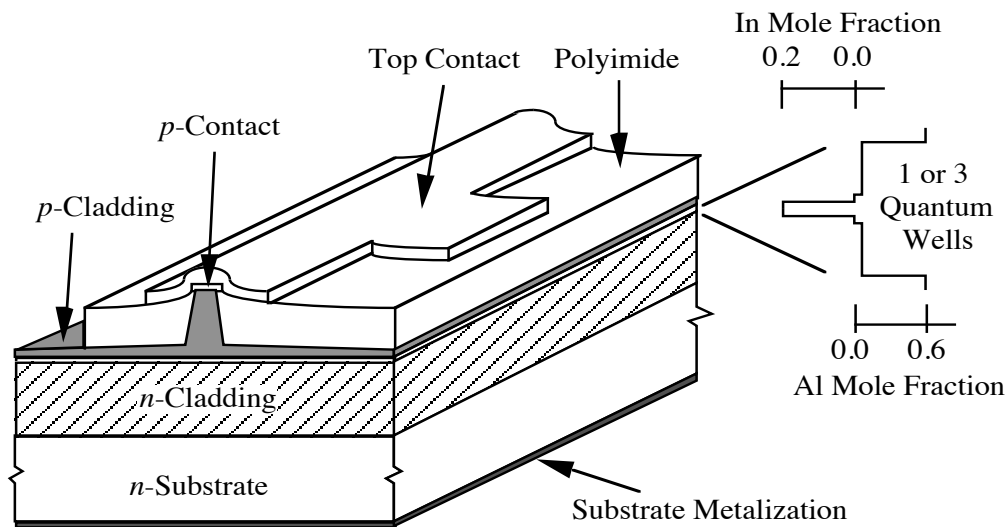


Fig. 6.6 Polyimide buried ridge waveguide laser.

The bond/probe pad is then deposited over the p -contact using lift-off. The metal sequence consists of 150 Å of Cr for adhesion followed by about 3500 Å of Au. The polyimide surface is severely *pitted* by the previous O₂ etch step, and the deposited bond pad adheres rather well to such a roughened surface.

The substrate is then thinned as previously, and the backside metallization is deposited. After this the sample is cleaved, and the devices are tested. The schematic diagram of the completed device is shown in Fig. 6.6. The bond pad/top contact deposited over the polyimide layer is patterned to minimize the parasitic capacitance.

6.3 Static Characteristics of Narrow Ridge Waveguide Devices

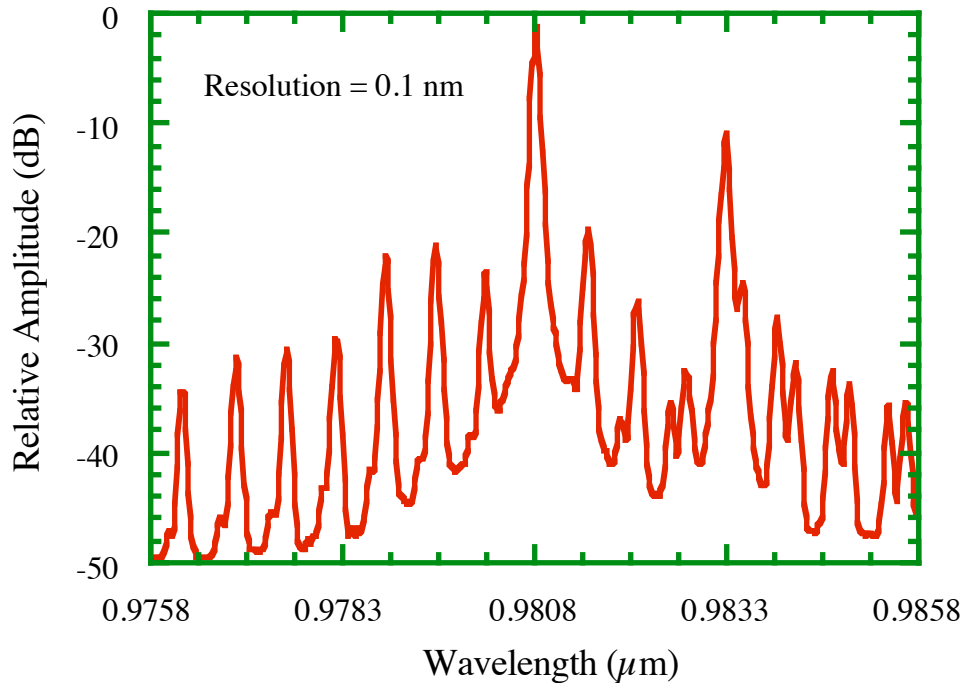


Fig. 6.7 Longitudinal mode spectrum of the polyimide buried ridge waveguide laser above threshold. The operating wavelength is about 980 nm.

Fig. 6.7 shows a typical longitudinal mode spectrum of the SQW polyimide buried ridge waveguide laser made from wafer F. The operating wavelength is, $\lambda = 980$ nm. The laser is multi-moded due to the Fabry-Perot design and the absence of any wavelength selective elements in the cavity. The next dominant mode is about 10 dB below in intensity. The cavity length of this device is, $L_c = 200 \mu\text{m}$, and from the mode spacing ($\Delta\lambda$), the mode index (n_{mode}) is calculated to be 3.66.

$$n_{\text{mode}} = \frac{\lambda^2}{2 L_c \Delta\lambda}$$

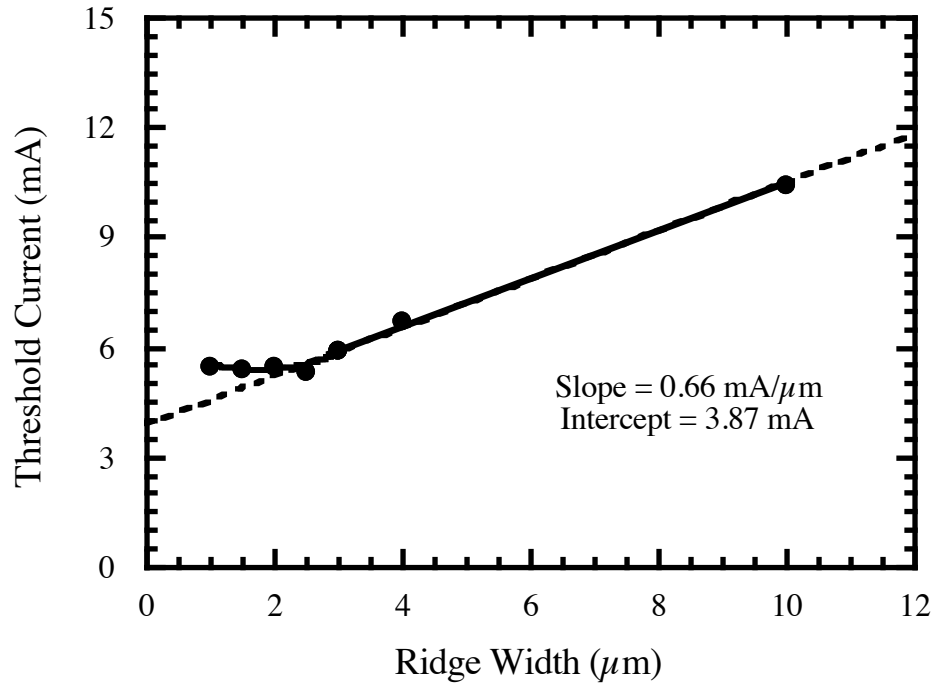


Fig. 6.8 Variation of threshold current with ridge width for $170 \mu\text{m}$ cavity length 3 QW device (Sample G).

Fig. 6.8 shows the variation of threshold current with stripe/ridge width for a $170 \mu\text{m}$ long 3 QW ridge waveguide laser (Sample G). The variation of threshold

current with stripe width is $0.66 \text{ mA}/\mu\text{m}$, and the linear extrapolated intercept is 3.87 mA . The intercept gives a measure of the leakage current and the lateral diffusion of carriers. For typical ridge widths of about $2 \mu\text{m}$, more than half the current at threshold ends up leaking, and hence not useful. This is one drawback of a ridge waveguide structure. Despite the high leakage current component, the results show that it is possible to fabricate lasers with low absolute threshold currents with narrow ridge waveguides down to $1 \mu\text{m}$ with this process.

The threshold current reaches a minimum at around the ridge width of $2 \mu\text{m}$. The increase in threshold current at smaller ridge widths is due to the loss of lateral optical confinement factor in the narrower ridge waveguide structures. At these dimensions the optical mode is no longer completely confined to the ridge waveguide, and the index discontinuity at the semiconductor/polyimide interface begins to introduce a significant amount of optical loss.

Fig. 6.9 shows the threshold current variation with temperature for two SQW laser samples. Sample C has a 3000 \AA wide SCH and Sample F has a 900 \AA wide SCH. Both of them have large T_0 , and the threshold current is very stable against variations in temperature. On closer examination of Fig. 6.9, one may notice that the T_0 value is not constant throughout the measurement range, but instead increases at about room temperature.

The threshold current for these lasers is very stable with variations in temperature. The values of T_0 measured here for the InGaAs/GaAs lasers are large compared to those between 50 K and 70 K reported for InGaAsP lasers at room temperature [9]. This suggests a good possibility of high speed operation of these lasers at elevated temperatures.

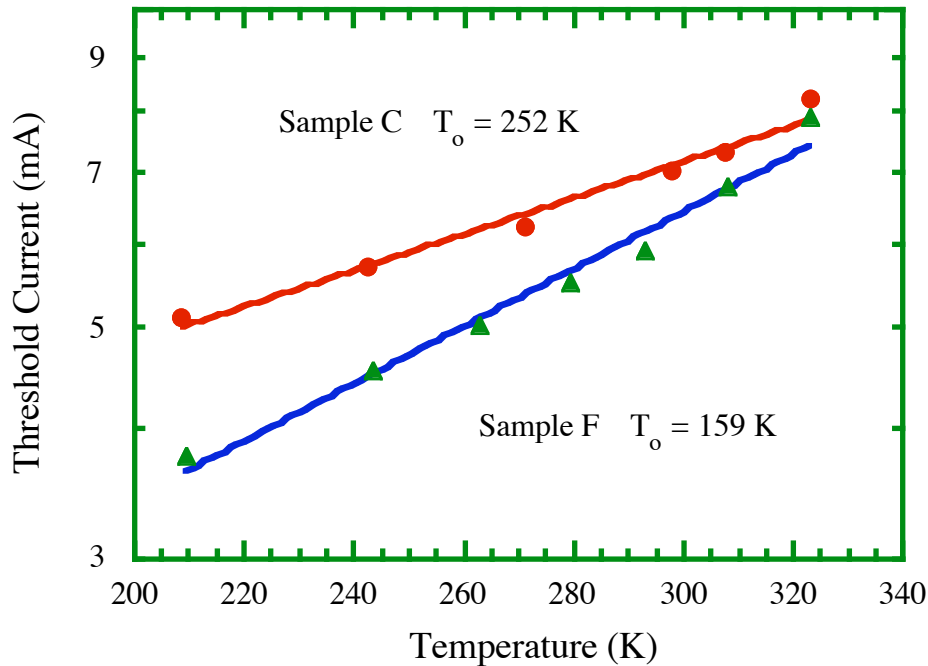


Fig. 6.9 Variation of threshold current with temperature for two SQW laser samples. Sample C has a $300 \mu\text{m}$ long cavity and $2.5 \mu\text{m}$ wide ridge. Sample F has a $200 \mu\text{m}$ long cavity and $2.0 \mu\text{m}$ wide ridge.

6.4 Microwave Mounting and Measurement of Laser Diodes

For the modulation response and the relative intensity noise measurement, the laser diodes have to be suitably packaged first. The schematic diagram of a mounted device is given in Fig. 6.10.

A laser bar is first separated into individual dies each consisting typically of 3 diodes. Each die is then attached to a copper heatsink using a Pb/Sn/Ag solder alloy (36 % Pb, 62.5 % Sn and 1.5 % Ag by weight) [10]. The rectangular solder preforms used for the die attach are 0.015" by 0.01" and 0.001" in thickness. The solder typically melts at around 140°C to 150°C . A soft solder liquid flux (no. 30) is also used with this process [11].

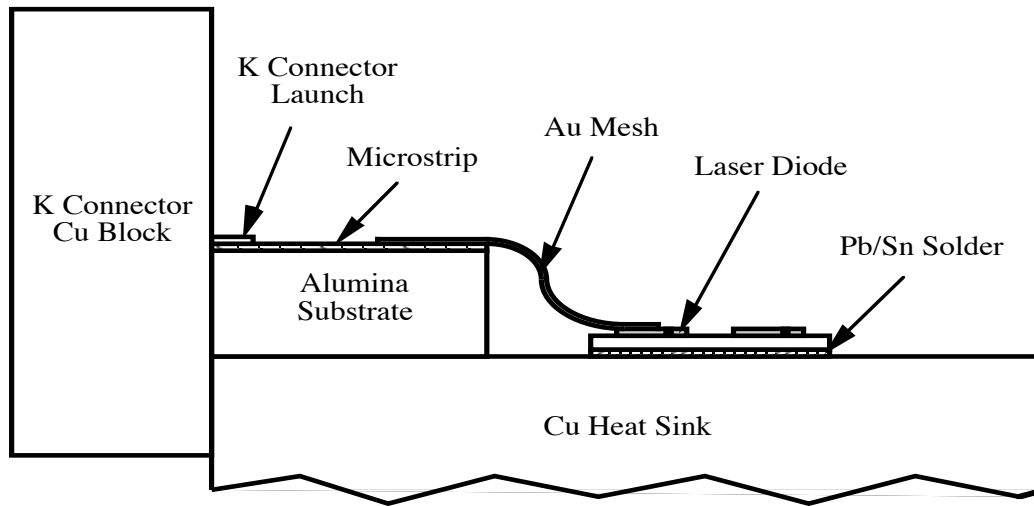


Fig. 6.10 Schematic diagram of the high speed laser mount.

The device is then bonded to a 50Ω microstrip transmission line (width = $250 \mu\text{m}$) on an alumina substrate (thickness = $250 \mu\text{m}$, $\epsilon_r \approx 10$) with a gold mesh. The other end of the microstrip is attached to the center of a K-connector launch [12].

The schematic diagram of the experimental setup used for the modulation response measurement is shown in Fig. 6.11.

The modulation response of the above microwave package is measured using a HP 8510 vector network analyzer and a high speed photodetector [13,14]. The data acquisition is done over the IEEE 488 type interface using a commercial instrumentation control software called the LABVIEW™ [15] which runs on a Macintosh II computer. This allows the data to be directly downloaded and manipulated on the computer.

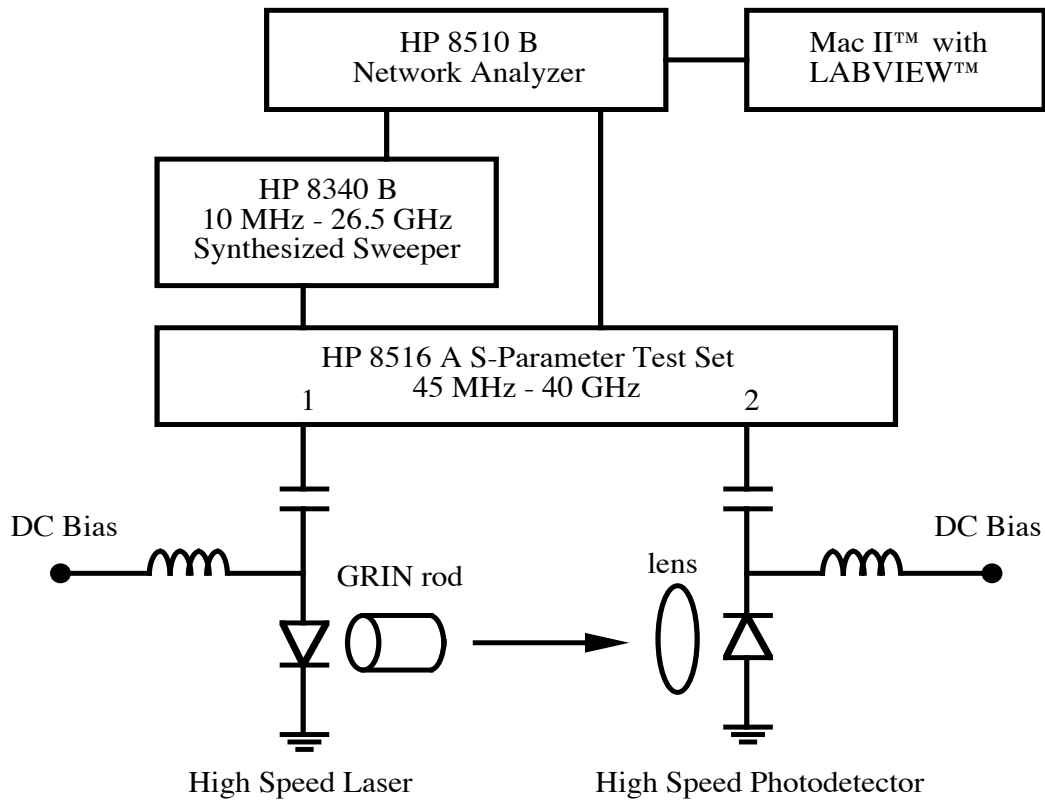


Fig.6.11 Schematic diagram of the experimental setup for the measurement of modulation response of laser diodes.

The experimental setup for the measurement of the relative intensity noise is shown in Fig. 6.12. Although the same laser mount is used, this is essentially a D.C. measurement. The laser diode is biased at various current levels (preferably C.W. for the best signal to noise ratio), and the spectrum of the steady state output is measured using a high speed photodiode and a spectrum analyzer. The process is again controlled and the data downloaded using a computer.

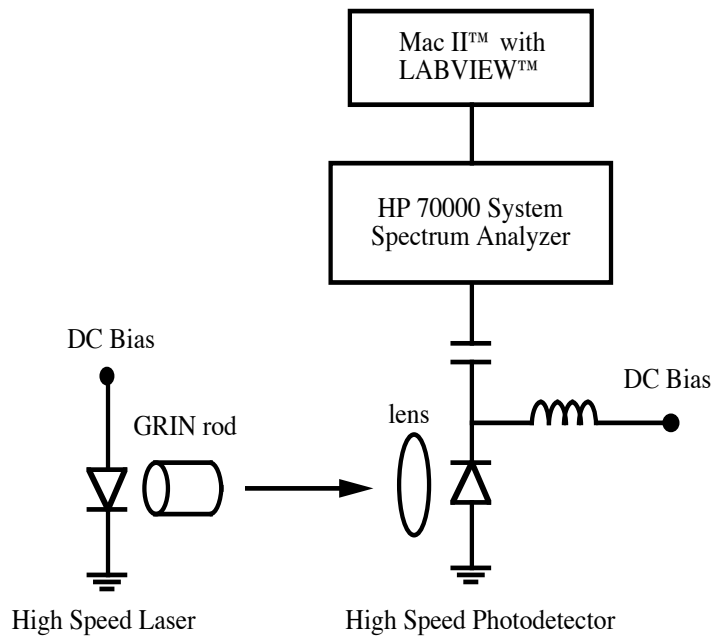


Fig. 6.12 Schematic diagram of the experimental setup for the measurement of relative intensity noise in laser diodes.

References

1. Manufactured by Commonwealth Scientific Corp., Alexandria, VA.
2. Program written by S. W. Corzine, University of California, Santa Barbara.
3. Manufactured by Buehler Corp., Lake Bluff, IL.
4. Manufactured by Ciba-Geigy Corp., Santa Clara, CA.
5. S. K. Ghandhi, *VLSI Fabrication Principles*, New York:Wiley, 1983, pp. 143.
6. P. Burggraaf, "Polyimides in Microelectronics," *Semiconductor International*, pp. 58-62, March 1988.
7. S. K. Ghandhi, *VLSI Fabrication Principles*, New York:Wiley, 1983, pp. 585.
8. Manufactured by Hoechst-Celanese Corp., Somerville, NJ.
9. G. P. Agrawal, and N. K. Dutta, *Long Wavelength Semiconductor Lasers*, New York:Van Nostrand Reinhold, 1986, pp. 128.
10. Manufactured by Coining Corp., Saddlebrook, NJ.
11. Manufactured by Superior Flux & Mfg. Co., Cleveland, OH.
12. Manufactured by Wiltron Corp., Morgan Hill, CA.
13. J. E. Bowers, and C. A. Burrus, "Ultrawide-Band Long-Wavelength *p-i-n* Photodetectors," *J. Lightwave Tech.*, vol. 5, pp. 1339-1350, 1987.
14. Y. G. Wey, D. L. Crawford, K. Giboney, J. E. Bowers, M. J. Rodwell, P. Silvestre, M. J. Hafich, and G. Y. Robinson, "Ultrafast Graded Double-Heterostructure GaInAs/InP Photodiode," *Appl. Phys. Lett.*, vol. 58, pp. 2156-2158, 1991.
15. Distributed by National Instruments, Austin, TX.

CHAPTER 7

CONCLUSION

Despite the initial enthusiasm generated by the early theoretical predictions of enhancement in differential gain, and consequently an enhancement in the modulation bandwidth in quantum well lasers, the road to the practical demonstration of these promised ultra high speed devices has been fraught with difficulties. In most cases, the high speed performance of quantum well lasers was worse than that of the lasers with bulk active areas. Part of this lack of progress is attributable to the relative infancy of the advanced crystal growth techniques that is required for the fabrication of these lasers. Large part of it is due to the incomplete knowledge of the parameters that had to be optimized in the design of these devices. Given the number of parameters that can be varied in designing a quantum well laser, the lack of good understanding of how these lasers operated led to the experimentation with a large variety of structures, and the publication of a wide range of results that seemed impossible to reconcile.

A major part of this work has been to establish the significance of carrier transport effects in the operation of high speed quantum well lasers, and develop a model that can be used for the practical design of such devices. It has been shown that the conventional high speed design philosophy in semiconductor lasers is not sufficient for the optimization of high speed quantum well lasers. The cladding, SCH and barrier layers in a quantum well laser have to be carefully designed to not only

maximize the optical confinement, but also to optimize the various carrier transport times, and carrier capture and confinement.

The transport time, τ_r , across the undoped regions of the laser has to be minimized. Long carrier transport delay in the undoped regions of the laser, as in the SCH in our case, introduces a low frequency parasitic-like rolloff which severely limits the maximum possible modulation bandwidth. A narrow SCH is desirable towards this end, but this will increase the internal loss in the case where the cladding loss is dominant, and decreasing the SCH width below an optimum point will also lead to a sharp drop in the optical confinement factor. These will result in a higher carrier density at threshold, and consequently a lower differential gain as a result of rapid gain saturation in quantum well lasers. These constraints lead to an optimum width for the SCH.

The transport factor χ given by $(1 + \tau_r/\tau_e)$ has to be minimized. A large χ leads to a decrease in the *effective* differential gain, and thus a decrease in the resonance frequency and an increase in the K factor. So, in addition to minimizing τ_r , the thermionic emission lifetime, τ_e , has to be maximized. This can be done by having deeper and wider quantum wells. This is generally true for a SQW laser, but in a MQW structure τ_e cannot be increased arbitrarily by increasing the depth of the quantum wells or the width of the barriers, because it will lead to carrier trapping in the quantum wells, and poor carrier transport between the quantum wells. The barriers must be of some minimum thickness and height to ensure that the carriers are two dimensionally confined to the quantum wells, and the inter-well coupling which leads to a broadening of the quantized energy levels is minimized. These

compromises lead to an optimum barrier height and width to maximize the modulation bandwidth in MQW lasers.

Modulation bandwidth in quantum well lasers is also a sensitive function of the cavity loss because of the rapid gain saturation with increasing carrier density. Thus, in quantum well lasers there is an optimum cavity length for the maximum modulation bandwidth below which the reduction in photon lifetime can no longer offset the loss in differential gain. This optimum value is dependent on the number of quantum wells, and for a SQW laser or lasers with a small number of quantum wells, good high speed performance can be obtained over a large range of cavity lengths.

In the presence of transport effects, the K factor extracted from relative intensity noise (RIN) measurements *cannot* be used to predict the modulation bandwidth of quantum well lasers. The maximum modulation in this case is limited by the low frequency rolloff due to transport, which does not affect the RIN spectrum. The maximum modulation bandwidth occurs at a power level where the initial rolloff due to carrier transport is so severe that the actual modulation response barely touches the - 3 dB point before the resonance peak in the intrinsic laser response causes it to turn back up again, before finally rolling off at a higher frequency.

The internal quantum efficiency of the semiconductor laser has a simple relationship to the carrier transport parameters derived here. The *carrier overflow* from the quantum well which is the result of insufficient carrier confinement and hence a reduced thermionic emission time, leads to a degradation of the high speed properties as well as the internal quantum efficiency of the lasers. This is the first time a link has been established between the static and dynamic properties of quantum well lasers on the basis of carrier transport effects.

Thus, careful device design is required to take advantage of the enhancement in differential gain obtained by the use of quantum wells in the active area. A mere replacement of the active area in a bulk laser by quantum wells is not sufficient.

In addition to establishing the design guidelines for high speed devices, detailed procedures have been demonstrated for the fabrication of high speed laser structures with a minimal amount of parasitic capacitance and resistance. As a result, quantum well lasers with minimum threshold currents of 5 mA and maximum modulation bandwidth of 22 GHz have been demonstrated. The performance of these lasers at present is limited by the thermal dissipation.

It is clear that carrier transport effects are a significant factor in the design of high speed quantum well lasers. This will be more of a problem as lower dimensional materials, like the quantum wires and the quantum boxes, are investigated for their suitability as the active medium with even higher differential gain in semiconductor lasers. The problem in the quantum well lasers have been addressed here in a quasi classical manner. It is not obvious that it may still be possible to do so in yet lower dimensional materials where there is a much reduced set of available energy states between which carrier interactions can take place. There may be a need for a complete quantum mechanical treatment of the carrier capture and emission processes in relation to the operation of high speed lasers.

The bandwidth requirements in a modern communication system are on the increase. The requirement for devices performing at ever increasing speeds has also been on the increase. Apart from the obvious material requirements, there is a real need for novel ideas to beat the limits to the speed of operation set by the device parasitics as well as the device size.

The biggest problem with present day high speed laser diodes is the device and package parasitics. Typically this limits the frequency of operation of these diodes to the 20 GHz to 30 GHz region. New fabrication techniques are required, based on the semi-insulating substrate technology to beat this limit. Successful microwave packaging is as much an art as it is a science. More work is needed in this field to make it more of a science, and more readily accessible.

The most successful present day laser diodes have cleaved facets for a long operating lifetime, and large power output at low operating current. There is a cavity length limit to which these devices may be usefully cleaved. Good cleaves require the cavity length to be somewhat larger than the substrate thickness. Substrate thicknesses of the order of 50 μm or so become difficult to handle, and this places the lower limit of 100 μm or so on the length of cleaved cavities. This will be a problem when the wavelength of the microwave signal becomes the same order of magnitude as the cavity length at very high frequencies.

The quest for devices operating at ever increasing speeds has been in the forefront of semiconductor laser research for a number of years now, and will be so for years to come. It is hoped that this work has made some lasting contribution towards the advancement of this field.

APPENDIX A

BROAD AREA CHARACTERISTICS

There were several different wafers fabricated during the period of this work. The material quality of all of them were determined by fabricating broad area lasers before the polyimide buried devices were made. This Appendix lists the epitaxial design and the broad area characteristics (indicative of the material quality) of the wafers from which the devices described in this dissertation were fabricated.

The wafers could be generally classified into four types from their respective carrier/optical confinement structures. These are given in Fig. A.1.

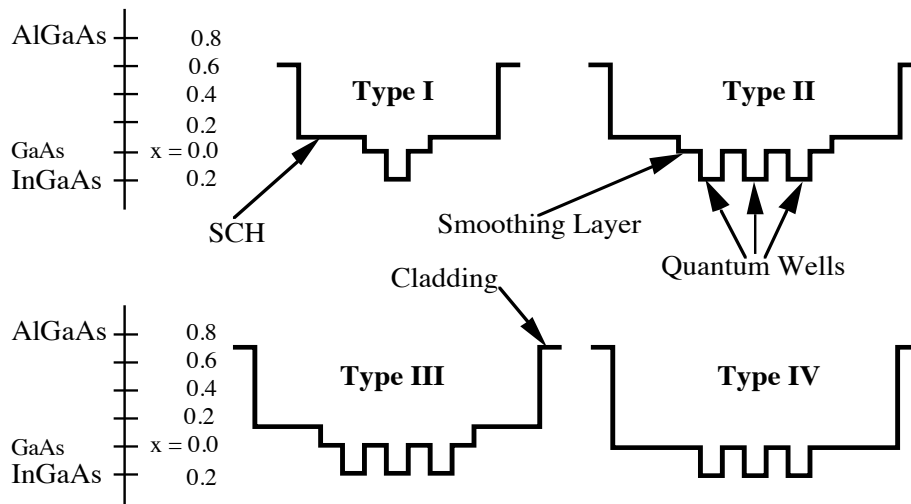


Fig. A.1 Conduction band energy diagram in terms of the Al mole fraction in AlGaAs and In mole fraction in InGaAs for the different structures investigated in this study.

The active layer structures vary in the width and the number of quantum wells, the width and the composition of the SCH, and the composition of the cladding. The quantum wells are composed of $\text{In}_{0.2}\text{Ga}_{0.8}\text{As}$, and smoothing layers are GaAs. In MQW lasers, the barriers are GaAs, and 80 Å thick. Type I and II have 1 μm thick claddings, while Type III and IV have 0.6 μm thick claddings.

The summary of the broad area results for the various wafers which have been referred to in the previous chapters is given in the following Table.

Wafer #	Type	L_s (Å)	L_w (Å)	Γ (%)	Min. J_{th} (A/cm ²)	α_{int} (cm ⁻¹)	η_i (%)
910528A - A	I	760	80	2.9	140	21.8	95.5
910528B - B	I	1500	80	2.7	129	11.8	80.7
910528C - C	I	3000	80	1.9	93	4.3	83.5
920103A - D	III	710	70	8.2	322	59.2	90.7
920103B - E	IV	710	70	8.9	387	36.9	66.7
901211B - F	I	900	80	3.0	125	6.9	93.8
901219A - G	II	700	80	9.2	247	14.4	83.8

- L_s Width of one side of SCH layer
- L_w Width of quantum well
- Γ Optical confinement factor
- Min. J_{th} Minimum threshold current density
- α_{int} total internal loss
- η_i internal quantum efficiency

APPENDIX B

MATERIAL PARAMETERS

B.1 Bandgaps, Effective Masses and Refractive Indices

The composition dependent direct bandgaps and effective masses used for the computations are as tabulated below;

Ref.	Quantity
1	Unstrained bandgap in the $\text{Al}_x\text{Ga}_{1-x}\text{As}$ alloy $E_g(x) = 1.424 + 1.594 x + x(1-x)(0.127 - 1.310 x) \text{ eV}$
2	Unstrained electron effective mass in the $\text{Al}_x\text{Ga}_{1-x}\text{As}$ alloy $m_e(x) / m_o = 0.0665 + (0.124 - 0.0665) x$
2	Unstrained heavy hole effective mass in the $\text{Al}_x\text{Ga}_{1-x}\text{As}$ alloy $m_h(x) / m_o = 0.34 + (0.5 - 0.34) x$
3	Strained bandgap in the $\text{In}_x\text{Ga}_{1-x}\text{As}$ alloy $E_g(x) = 1.424 - 1.061 x + 0.07 x^2 + 0.03 x^3 \text{ eV}$
3	Unstrained electron effective mass in the $\text{In}_x\text{Ga}_{1-x}\text{As}$ alloy $m_e(x) / m_o = 0.0665 + (0.023 - 0.0665) x$
3	Unstrained heavy hole effective mass in the $\text{In}_x\text{Ga}_{1-x}\text{As}$ alloy $m_h(x) / m_o = 0.377 + (0.341 - 0.377) x$

The refractive index values required for the computation of the optical mode profile and the confinement factor are calculated using the single effective oscillator (SEO) method. From the model derived by Afromowitz [4], the refractive index, n , is given by the following relationship,

$$n^2 = 1 + \frac{E_d}{E_o} + \frac{E_d}{E_o^3} (hv)^2 + \frac{\sigma}{\pi} (hv)^4 \ln \left[\frac{2 E_o^2 - E_g^2 - (hv)^2}{E_g^2 - (hv)^2} \right]$$

where

$$\sigma = \frac{\pi E_d}{2 E_o^3 (E_o^2 - E_g^2)}$$

The values for the direct bandgap, E_g , have been already tabulated. The hv term is the photon energy of the propagating field. The values for E_o and E_d are,

Material	Quantity	Ref.
$Al_xGa_{1-x}As$	$E_o(x) = 3.65 + 0.871x + 0.179x^2$ eV	4
	$E_d(x) = 36.1 - 2.45x$ eV	4
$In_xGa_{1-x}As$	$E_o(x) = 3.65 - 2.15x$ eV	5
	$E_d(x) = 36.1 - 19.9x$ eV	5

This theoretical model agrees fairly well with the experimentally measured refractive index values, but has a singularity at the bandgap, i.e. at $E_g = hv$. In this region, a simpler relationship based also on the SEO method derived by Wemple and DiDomenico [6] is more useful;

$$n^2 = 1 + \frac{E_d E_o}{E_o^2 - (h\nu)^2}$$

B.2 Electron and Hole Mobilities and Diffusion Coefficients

At thermal equilibrium the diffusion coefficient, D , is related to the carrier mobility via the Einstein relation. In nondegenerate semiconductors the following relation holds;

$$D = \left(\frac{k T}{q} \right) \mu_d$$

where the subscript d refers to the fact that the mobility used is the drift (conductivity) mobility [7]. Since most of the transport parameters reported in literature are typically from Hall measurements, the resulting mobility is the Hall mobility, μ_H . The two mobilities are related to one another via the Hall factor, r_H .

$$\mu_d = \frac{\mu_H}{r_H}$$

The temperature dependence of hole mobility generally has the following form,

$$\mu = \mu_{300\text{K}} \left(\frac{300\text{(K)}}{T\text{(K)}} \right)^\beta$$

For holes in GaAs, at sufficiently large temperatures, i.e. in the region of interest to us (100K to 400K), Hill [8] has suggests that $\beta = 2.41$ would be a good fit

to the temperature dependence of mobility, while Wiley [9] from his earlier work and an extensive review later, suggests a β of 2.3. This is somewhat higher than the temperature dependence of $T^{-2.1}$ suggested by Sze [7]. A numerical fit to the later work by Masu, et al., [10] gives a temperature dependence of $T^{-2.3}$. The Hall factor is also temperature dependent, and after accounting for it, Adams [11] suggests a β of - 2.2. This value of β has also been assumed for the AlGaAs SCH layer (10 % to 15 % Al mole fraction). The Hall mobility for holes at room temperature in $\text{Al}_{0.1}\text{Ga}_{0.9}\text{As}$ is taken to be $250 \text{ cm}^2/\text{Vs}$ [10], and the Hall factor to be 1.25 [12] resulting in a value of $\mu_{300\text{K}} = 200 \text{ cm}^2/\text{Vs}$.

The temperature dependence of electron mobility is more complicated. No simple power fit is suitable to model the temperature dependence of electron mobility in the range of our interest [12,13]. We have done a polynomial fit to the data reported by Bhattacharya, et al., [14] and obtained the following expression for the temperature dependence of electron mobility in $\text{Al}_{0.1}\text{Ga}_{0.9}\text{As}$;

$$\mu_{\text{H,n}} = 5820 - 3110 \left[\frac{T(\text{K})}{300(\text{K})} \right] + 535 \left[\frac{T(\text{K})}{300(\text{K})} \right]^2 \text{ cm}^2 / \text{V s}$$

We have taken the Hall factor to be 1.175 [12], and independent of temperature.

The variation of electron Hall mobility with composition, x , in $\text{Al}_x\text{Ga}_{1-x}\text{As}$ at 300 K was taken from [15]. Fig. B.1 shows the reproduction of Fig. 1 from [15], and the corresponding numerical fit to the original data. There is clearly a minimum in the electron mobility at $x \approx 0.47$, and separate numerical fits have been used for the variation before and after this point ($x = 0.48$ seemed to be the best point to do this).

$$x \leq 0.48$$

$$\mu_e(x) = 6594.2 - 17460x + 38478x^2 - 101530x^3 + 76269x^4 \text{ cm}^2 / \text{V s}$$

$$x > 0.48$$

$$\mu_e(x) = -9240.2 + 59510x - 150610x^2 + 190860x^3 - 120970x^4 + 30637x^5 \text{ cm}^2 / \text{V s}$$

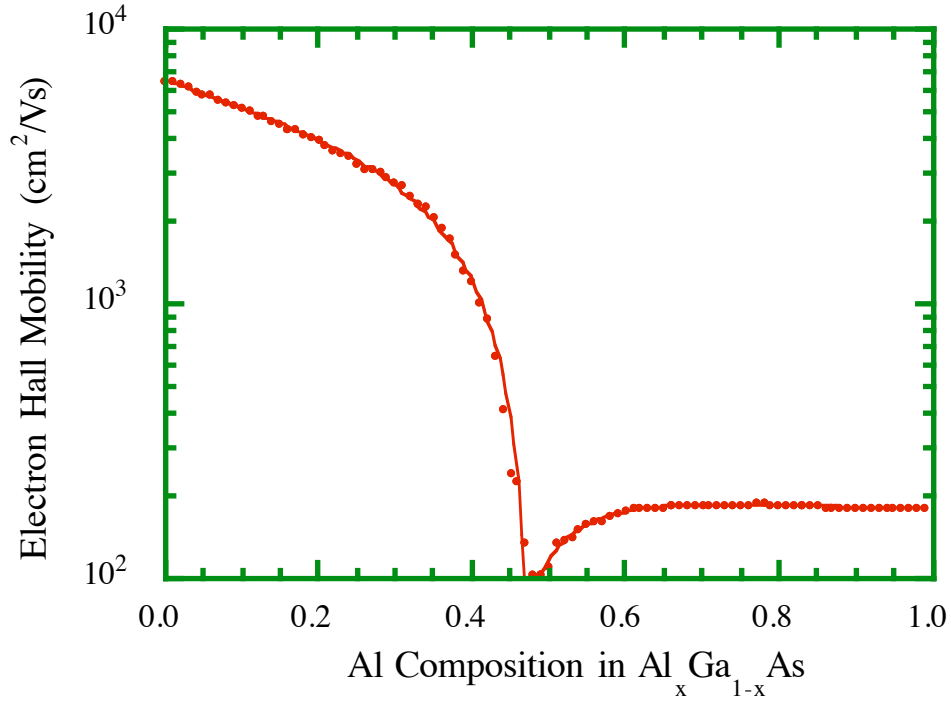


Fig. B.1 Variation of electron Hall mobility in Al_xGa_{1-x}As with Al composition.

For low alloy compositions, $0 \leq x \leq 0.32$, the Γ minimum is the lowest energy minimum and the effect of electrons in the L and X minima on Hall mobility are negligible. Similarly for high alloy compositions, $0.60 \leq x \leq 1.00$, X minima are the lowest in energy, and the effect of electrons in Γ and L minima are negligible. For the intermediate compositions, $0.32 \leq x \leq 0.60$, the contributions from all three minima

become significant, and the minimum in Hall mobility at about $x \approx 0.47$ occurs due to a combination of intervalley, alloy, and space charge scattering. The direct (Γ)-indirect (X) crossover composition is at $x \approx 0.43$ [15]. The Hall factor for electron mobility is also dependent on Al mole fraction, and attains a peak value of 3.8 at $x = 0.42$, due to the multiband conduction effects [16]. This ratio is found to be close to unity for the alloy composition ranges of interest to us in this work; $0 \leq x \leq 0.25$ and $0.6 \leq x \leq 0.78$. Thus our previous assumption of a constant Hall factor is appropriate.

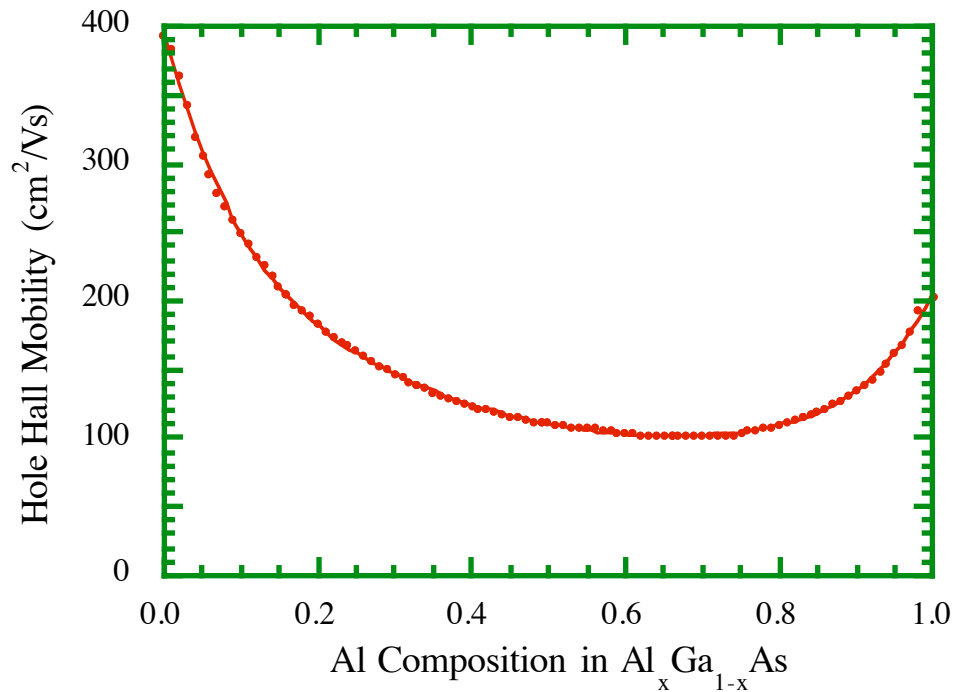


Fig. B.2 Variation of hole Hall mobility in $\text{Al}_x\text{Ga}_{1-x}\text{As}$ with Al composition.

The variation of hole Hall mobility with composition, x , in $\text{Al}_x\text{Ga}_{1-x}\text{As}$ at 300 K was taken from [10]. Fig. B.2 shows the reproduction of Fig. 3 (the curve for $\Delta E_{\text{alloy}} = 0.7$ eV and $N_a = 1 \times 10^{16} \text{ cm}^{-3}$) from [10], and the corresponding numerical

fit to the original data. There are no discontinuities in the curve as before, and a single numerical fit is sufficient in this case;

$$\mu_h(x) = 397.98 - 2154.2x + 8567.0x^2 - 21234x^3 + 30765x^4 - 23620x^5 + 7484.8x^6 \text{ cm}^2 / \text{V s}$$

B.3 Optical Gain and its Temperature Dependence

The carrier density dependent optical gain is theoretically calculated using valence band mixing effects from the model presented in [3]. A conduction band offset of 60% is used. In calculating the energy bands in the strained material, valence band mixing is taken into account via the Luttinger-Kohn Hamiltonian while the conduction band is treated in the effective mass approximation.

The band offset ratio has been taken to be temperature independent, and the bandgaps of the various constituent layers to have the same temperature dependence. This assumption would ensure that the energy offsets between the various layers, or in other words the potential barrier heights, in the laser structure are independent of temperature although the absolute bandgaps are changing.

Fig. B.3 shows the theoretically calculated gain-threshold current density relation presented together with the experimental data for threshold gain obtained from broad area measurements on three wafers of SQW lasers; Samples A, B and C. Except at very low current densities there is a good agreement between the model and the measured gain values.

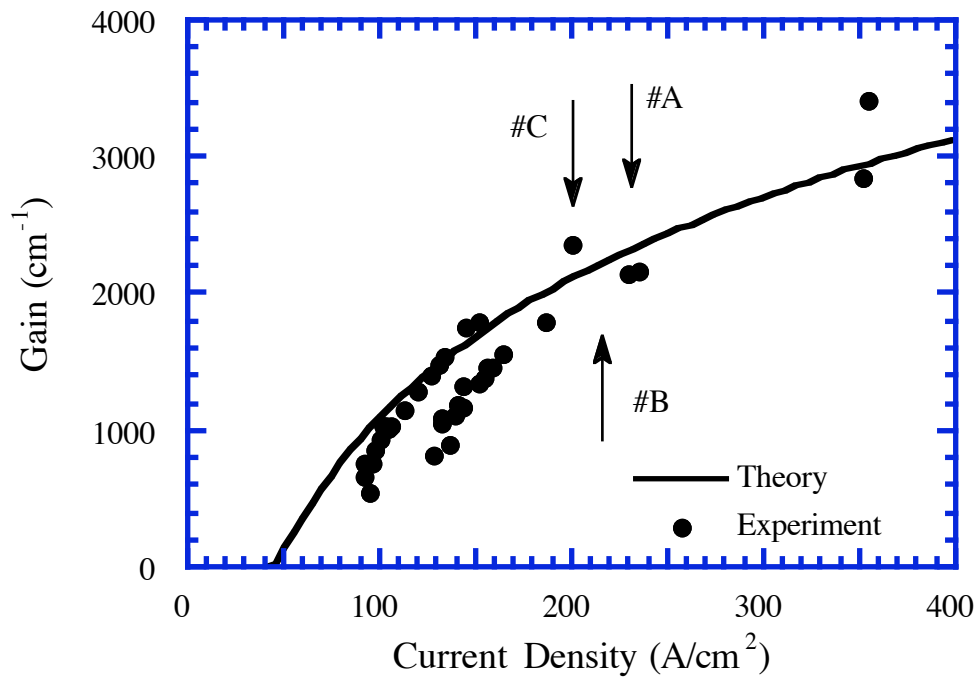


Fig. B.3 Theoretical and experimental variation of material gain with current density for an 80 Å $\text{In}_{0.2}\text{Ga}_{0.8}\text{As}/\text{GaAs}$ quantum well. The experimental data are from the broad area measurements on Samples A, B and C. The arrows indicate the respective operation points of 300 μm cavity length devices.

Using the same model, the gain-carrier density relationship can be calculated at various temperatures. Fig. B.4 shows the carrier density dependence of gain at a number of different temperatures. For a constant level of loss in the cavity the material gain as well as the differential gain are reduced at increased temperatures. This is the loss in static differential gain with increasing temperature. This can be further aggravated by the deterioration of transport factor, χ , at elevated temperatures.

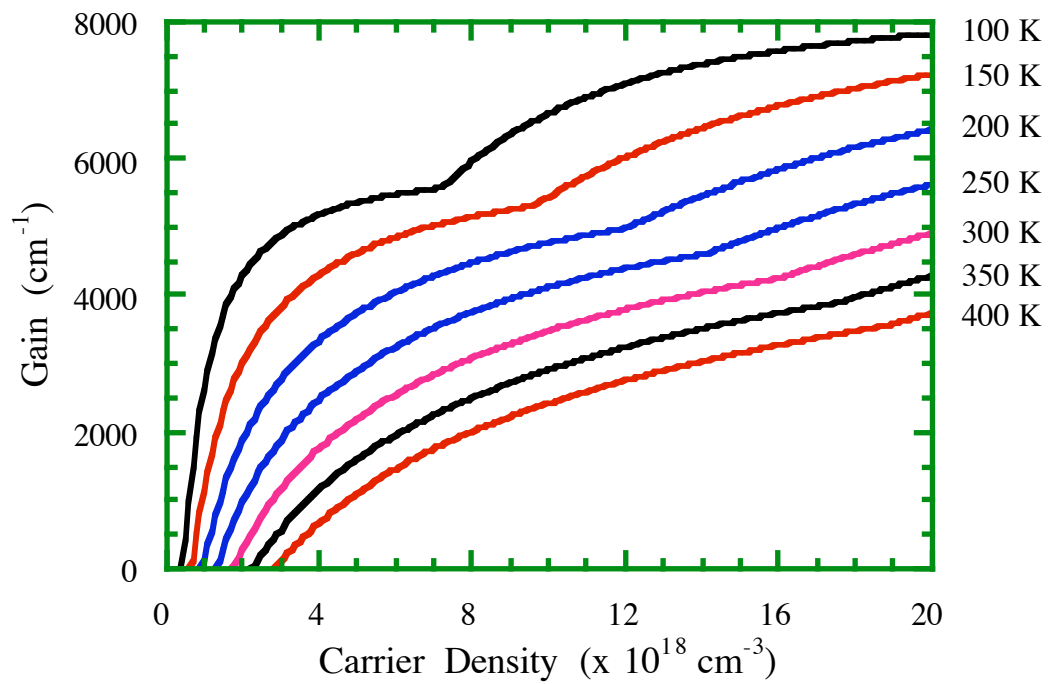


Fig. B.4 Temperature dependence of gain-carrier density relationship for the same active layer parameters in Fig. B.3.

References

1. D. E. Aspnes, S. M. Kelso, R. A. Logan, and R. Bhat, "Optical Properties of $\text{Al}_x\text{Ga}_{1-x}\text{As}$," *J. Appl. Phys.*, vol. 60, pp. 754-767, 1986.
2. D. A. Kleinman, and R. C. Miller, "Band-gap Renormalization in Semiconductor Quantum Wells containing Carriers," *Phys. Rev.*, vol. B 32, pp. 2267-2272, 1985.

See also B. V. Shanabrook, O. J. Glembocki, D. A. Broida, and W. I. Wang, "Luttinger Parameters for GaAs Determined from the Intersubband Transitions in GaAs/ $\text{Al}_x\text{Ga}_{1-x}\text{As}$ Multiple Quantum Wells," *Phys. Rev.*, vol. B 39, pp. 3411-3414, 1989.
3. S. W. Corzine, R. H. Yan, and L. A. Coldren, "Theoretical Gain in Strained InGaAs/AlGaAs Quantum Wells Including Valence-Band Mixing Effects," *Appl. Phys. Lett.*, vol. 57, pp. 2835-2837, 1990.

See also S. W. Corzine, R. H. Yan, and L. A. Coldren, "Optical Gain in III-V Bulk and Quantum Well Semiconductors," in *Quantum Well Lasers*, Chap. 1, P. S. Zory:Ed., New York:Academic, to be published.
4. M. A. Afromowitz, "Refractive Index of $\text{Ga}_{1-x}\text{Al}_x\text{As}$," *Solid State Comm.*, vol. 15, pp. 59-63, 1974.
5. T. Takagi, "Refractive Index of $\text{Ga}_{1-x}\text{In}_x\text{As}$ Prepared by Vapor-Phase Epitaxy," *Jpn. J. Appl. Phys.*, vol. 17, pp. 1813-1817, 1978.
6. S. H. Wemple, and M. DiDomenico, Jr., "Behavior of the Electronic Dielectric Constant in Covalent and Ionic Materials," *Phys. Rev.*, vol. B 3, pp. 1338-1351, 1971.
7. S. M. Sze, *Physics of Semiconductor Devices*, 2nd ed. New York:Wiley, 1981, pp. 29-30.

8. D. E. Hill, "Activation Energy of Holes in Zn-Doped GaAs," *J. Appl. Phys.*, vol. 41, pp. 1815-1818, 1970.

See also D. Kranzer, "Mobility of Holes of Zinc-Blende III-V and II-VI Compounds," *Phys. Stat. Sol.*, vol. A 26, pp. 11-52, 1974.
9. J. D. Wiley, and M. DiDomenico, Jr., "Lattice Mobility of Holes in III-V Compounds," *Phys. Rev.*, vol. B 2, pp. 427-433, 1970.

See also J. D. Wiley, "Mobility of Holes in III-V Compounds," in *Semiconductor and Semimetals*, R. K. Williardson, and A. C. Beer, Eds., New York: Academic Press, 1975, pp. 91-174.
10. K. Masu, E. Tokumitsu, M. Konagai, and K. Takahashi, "Alloy Scattering Potential in *p*-type Ga_{1-x}Al_xAs," *J. Appl. Phys.*, vol. 54, pp. 5785-5792, 1983.
11. A. R. Adams, "Hole Mobility in GaAs, Temperature Dependence", in *EMIS Datareview Series No. 2: RN=15457*, 2nd ed. New York:INSPEC, IEE, 1990, pp. 103.
12. J. S. Blakemore, "Semiconducting and other Major Properties of Gallium Arsenide," *J. Appl. Phys.*, vol. 53, pp. R123-R181, 1982.
13. D. L. Rhode, and S. Knight, "Electron Transport in GaAs," *Phys. Rev.*, vol. B 3, pp. 2534-2541, 1971.

See also D. L. Rhode, "Low Field Electron Transport," in *Semiconductor and Semimetals*, R. K. Williardson, and A. C. Beer, Eds., New York: Academic Press, 1975, pp. 1-89.
14. P. K. Bhattacharya, U. Das, and M. J. Ludowise, "Transport Properties of *n*-type Metalorganic Chemical-Vapor-Deposited Al_xGa_{1-x}As (0 ≤ x ≤ 0.6)", *Phys. Rev.*, vol. B 29, pp. 6623-6631, 1984.
15. A. K. Saxena, "Electron Mobility in Ga_{1-x}Al_xAs Alloys," *Phys. Rev.*, vol. B 24, pp. 3295-3302, 1981.

16. A. K. Saxena, "Hall to Drift Mobility Ratio in $\text{Ga}_{1-x}\text{Al}_x\text{As}$ Alloys," *Solid State Comm.*, vol. 39, pp. 839-842, 1981.

APPENDIX C

DETAILS OF RATE EQUATION ANALYSIS

C.1 Small Signal Expansion of the Stimulated Emission Term

The stimulated emission term in the rate equations for the carrier density and the photon density has the gain compression factor in the denominator. This makes the small signal expansion of this term more complicated. With the small signal quantities inserted, the stimulated emission term can be written as,

$$\frac{v_g G(P) S}{1 + \epsilon S} = \frac{v_g [G_o + g_o P_W] (S_o + s)}{1 + \epsilon (S_o + s)}$$

Expanding the denominator alone in a Taylor series,

$$\begin{aligned} & \frac{1}{1 + \epsilon (S_o + s)} \\ &= 1 - \epsilon (S_o + s) + \epsilon^2 (S_o + s)^2 - \epsilon^3 (S_o + s)^3 + \dots \\ &= \left(1 - \epsilon S_o + \epsilon^2 S_o^2 - \epsilon^3 S_o^3 + \dots\right) - \epsilon s \left(1 - 2 \epsilon S_o - \epsilon s + 3 \epsilon^2 S_o^2 + 3 \epsilon^2 S_o s + \epsilon^2 s^2 + \dots\right) \end{aligned}$$

The s^2 term, which is product of two small signal quantities, is very small, and is therefore negligible when only the first order terms are considered.

$$\begin{aligned} & \frac{1}{1 + \epsilon (S_o + s)} \\ &\approx \left(1 - \epsilon S_o + \epsilon^2 S_o^2 - \epsilon^3 S_o^3 + \dots\right) - \epsilon s \left(1 - 2 \epsilon S_o + 3 \epsilon^2 S_o^2 - \dots\right) \\ &= \frac{1}{1 + \epsilon S_o} - \frac{\epsilon s}{(1 + \epsilon S_o)^2} \end{aligned}$$

This is then substituted into the original expression which then simplifies to,

$$\begin{aligned}
\frac{v_g G(P) S}{1 + \epsilon S} &= \frac{v_g [G_o + g_o P_W] (S_o + s)}{1 + \epsilon (S_o + s)} \\
&= v_g [G_o + g_o P_W] (S_o + s) \left(\frac{1}{1 + \epsilon S_o} - \frac{\epsilon s}{(1 + \epsilon S_o)^2} \right) \\
&= \frac{v_g G_o S_o}{1 + \epsilon S_o} + \frac{v_g g_o S_o}{1 + \epsilon S_o} P_W + \frac{v_g G_o}{1 + \epsilon S_o} s - \frac{v_g G_o \epsilon S_o}{(1 + \epsilon S_o)^2} s \\
&= \frac{v_g G_o S_o}{1 + \epsilon S_o} + \frac{v_g g_o S_o}{1 + \epsilon S_o} P_W + \frac{v_g G_o}{(1 + \epsilon S_o)^2} s
\end{aligned}$$

C.2 Maximum Modulation Bandwidth in terms of the K Factor

In the absence of the low frequency rolloff, the relationship for the - 3 dB point in the modulation response is given by,

$$\begin{aligned}
\frac{\omega_r^4}{(\omega^2 - \omega_r^2)^2 + \omega^2 \gamma^2} &= \frac{1}{2} \\
\omega^4 - \omega_r^4 - 2 \omega^2 \omega_r^2 + \omega^2 \gamma^2 &= 0
\end{aligned} \tag{1}$$

The maximum modulation bandwidth is only limited by the photon lifetime and the gain compression factor, and not the output power of the device. From the small signal analysis, both the square of the resonance frequency and the damping rate vary linearly with output power.

$$\omega_r^2 = a P \qquad \gamma = b P$$

If these linear relations are substituted into the equation for the - 3 dB point of the modulation response function,

$$\omega^4 - a^2 P^2 - 2 a P \omega^2 + b^2 P^2 \omega^2 = 0$$

To find the maximum possible bandwidth, differentiate ω with respect to P .

$$\frac{d \omega}{d P} = \frac{2 a^2 P + 2 a \omega^2 - 2 b^2 \omega^2 P}{4 \omega^3 - 4 a P \omega + 2 b^2 P^2 \omega}$$

Setting the above expression to zero, and substituting back for the terms in P , one obtains the expression for the maximum modulation bandwidth,

$$2 a^2 P + 2 a \omega_{\max}^2 - 2 b^2 \omega_{\max}^2 P = 0$$

$$\omega_{\max}^2 = \frac{\omega_r^4}{\gamma^2 - \omega_r^2} \quad (2)$$

Together with (1), one obtains the relationship between ω_r and γ at $\omega = \omega_{\max}$,

$$\left(\frac{\omega_r^4}{\gamma^2 - \omega_r^2} \right)^2 - \omega_r^4 - 2 \omega_r^2 \left(\frac{\omega_r^4}{\gamma^2 - \omega_r^2} \right) + \gamma^2 \left(\frac{\omega_r^4}{\gamma^2 - \omega_r^2} \right) = 0$$

$$2 \omega_r^2 = \gamma^2$$

$$\gamma = \sqrt{2} 2 \pi f_r$$

Substituting this into (2), the expression for f_{\max} can be written as,

$$f_{\max} = f_r$$

From the definition of the K factor, the following relation can be written,

$$\gamma = K f_r^2$$

$$\sqrt{2} 2 \pi f_r = K f_r^2$$

$$\sqrt{2} 2 \pi f_{\max} = K f_{\max}^2$$

$$f_{\max} = \frac{2 \sqrt{2} \pi}{K}$$

APPENDIX D

DEVICE AND MOUNT PARASITICS

D.1 Parameter Extraction from Network Analyzer Measurements

In addition to the optimum design of the epitaxial layers of the quantum well laser, the device and mount parasitics have to be minimized to obtain the maximum modulation bandwidth. The knowledge of these parasitics is essential to distinguish between the intrinsic and parasitic limits to the modulation bandwidth of the quantum well lasers. This is especially significant in the case of transport limited lasers where the low frequency rolloff in the modulation response is similar to a parasitic limited device.

The device and mount parasitics were carefully determined for identical devices from Samples A, B and C to establish that the wide SCH devices were truly transport limited. As discussed in Chapter 6, a vector network analyzer (HP 8510B) is used to determine the modulation bandwidth (S_{21}) of the combination of the laser diode (connected to port 1) and a high speed photodetector (connected to port 2). Using the same setup the parasitics of the laser diode can be extracted from the power reflection coefficient measured at port 1, i.e. by measuring the S_{11} parameter.

The equivalent circuit of the mounted high speed laser diode is determined by numerically fitting to the measured S_{11} parameter using a commercial microwave modeling program called Touchstone™ [1]. The elements of this equivalent circuit are the parasitics of interest here. Due to the numerical nature of this fitting process,

to correctly obtain the values for the parasitic elements, one has to have some prior knowledge of the simplest equivalent circuit which would be physically correct.

The electrical equivalent circuit of the packaged laser diode has been analyzed as two separate two parts [2-6]; one that of the package and laser chip parasitics and the other that of the intrinsic active area. Fig. D.1. shows an equivalent circuit of a packaged laser diode, and the model in [3] will be closely followed here.

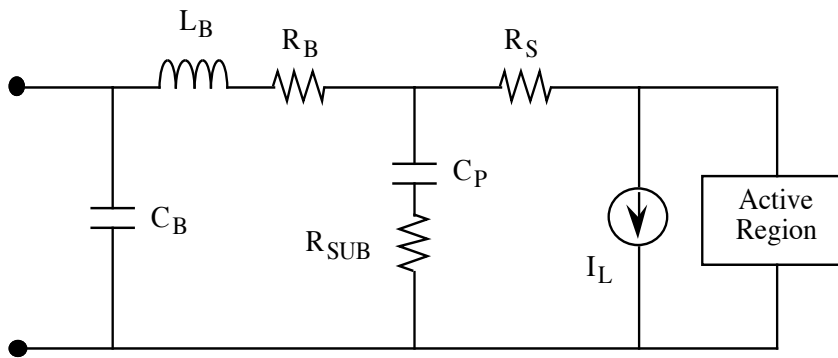


Fig. D.1 Equivalent circuit of a packaged laser diode.

The various elements of the circuit above are as follows,

I_L	D.C. leakage current in the paths which bypass the active region. This will not have any effect on the circuit parameters extracted from the S_{11} data at microwave frequencies.
R_S	Series diode resistance which has contributions from the contacts, bulk epitaxial layers (the narrow p cladding especially) and the heterointerfaces. Suitable contact metals, heavily doped cap and cladding regions and graded heterointerfaces are used to minimize the series resistance

C_P	Parasitic capacitance of the laser diode structure. The typical in-plane laser is a parallel plate capacitor. The capacitance contribution from the epitaxial layers is significant due to their much larger relative permittivity, and a narrow ridge waveguide polyimide buried laser structure minimizes this.
R_{SUB}	Substrate resistance which appears in series with the parasitic capacitance. This is small since the lasers have been grown on n^+ substrates doped in the range of 10^{18} cm^{-3} .
L_B	Bond wire inductance.
R_B	Bond wire resistance. The lasers here are bonded using a fairly short mesh instead of a wire. Thus, R_B is not significant.
C_B	Package capacitance due to the bond wire-microstrip transition.

The equivalent circuit for the active region is given in Fig. D.2.

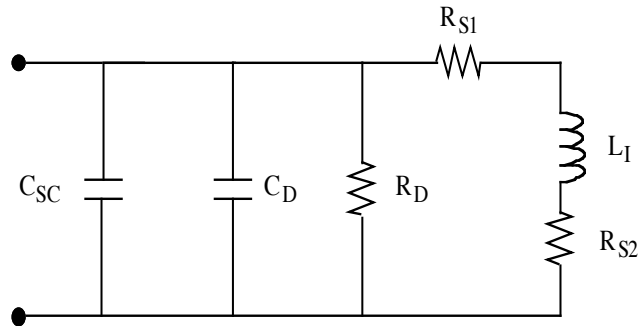


Fig. D.2 Equivalent circuit of laser diode active area.

Except for C_{SC} , the space charge capacitance, all the other circuit elements in Fig. D.2 are derived from the small signal analysis of the conventional laser rate

equations [2,3]. Ref. [4] considers an extension of this model to quantum well lasers, and Ref. [5] has also included the effects of the carrier capture (ignoring the SCH transport time) and escape times on the electrical equivalent circuit.

The charge storage in the active layer is represented by the diffusion capacitance, C_D , and the small signal photon storage by the inductance, L_I . The relaxation oscillation is a resonance between the total capacitance $C_D + C_{SC}$ and the inductance L_I [3]. This relaxation oscillation is the exchange of energy between the carriers and photons. The damping of this resonance is determined by the resistors R_{S1} , R_{S2} and R_D . These resistances are proportional to R_d , which is the intrinsic diode resistance given by $\frac{\eta kT}{qI_{bias}}$ where η is the ideality factor of the laser diode, I_{bias} is the operating current level and kT/q is the thermal voltage which is 25.9 mV at 300 K.

The laser diodes are operated at high bias currents (typically about 100 mA) to obtain the largest modulation bandwidths. At these current levels the intrinsic diode resistance, R_d , is about 0.5 Ω ($\eta = 2$), and R_D is a very low resistance path to ground [6]. Thus, the effects of the intrinsic laser active area parameters become negligible at these bias levels, and the resulting equivalent circuit is *virtually* a short circuit to ground. The simplified equivalent circuit for the package and laser chip parasitics is then combined with that for the laser active area. Further, the laser mount has a K connector and a length of 50 Ω matched microstrip. The effective length of these connectors will add to the total phase of the S_{11} parameter. Including these elements, the equivalent circuit for a highly forward biased laser diode is given in Fig. D.3. The characteristics of the microstrip and the Alumina substrate used in the model are given in Fig. D.3. The length of the microstrip, L_{mstrip} , is determined from the fitting

process. L_{mstrip} also includes the effective length of the K connector block which is before the microstrip. The microwave characteristics of the bias T is included in the calibration of the network analyzer, and does not have to be separately accounted for.

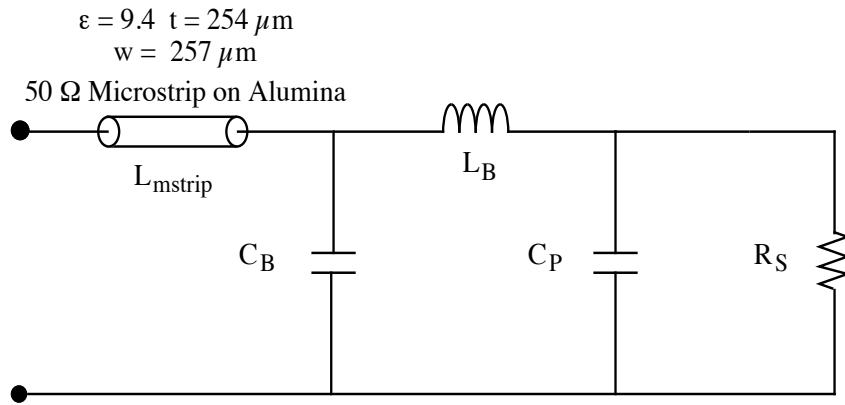


Fig. D.3 Equivalent circuit of the laser diode and mount used in the parameter extraction from measured S_{11} values.

For Samples A, B and C which have different SCH widths, intrinsic diode capacitance is different, and this will make a difference at low bias levels when R_d is large. At operating current levels used here R_d is small, and the equivalent circuit in Fig. D.3 is sufficient for the parameter extraction purposes. The tabulated values of these parameters for the case of Samples A, B and C are given below.

Sample	SCH Width (\AA)	L_{mstrip} (mm)	R_S (Ω)	C_P (pF)	L_B (nH)	C_B (pF)
A	760	9.0	4.0	1.80	0.115	0.43
B	1500	9.7	3.8	1.95	0.20	0.36
C	3000	9.1	4.0	2.00	0.13	0.40

From the table it can be seen that the parasitic circuit elements for the devices from all three samples have quite similar values. C_P is slightly larger for the wider SCH devices but this is not significant. The values for L_{mstrip} and L_B are within the tolerances expected for devices that have to be operator mounted one at a time.

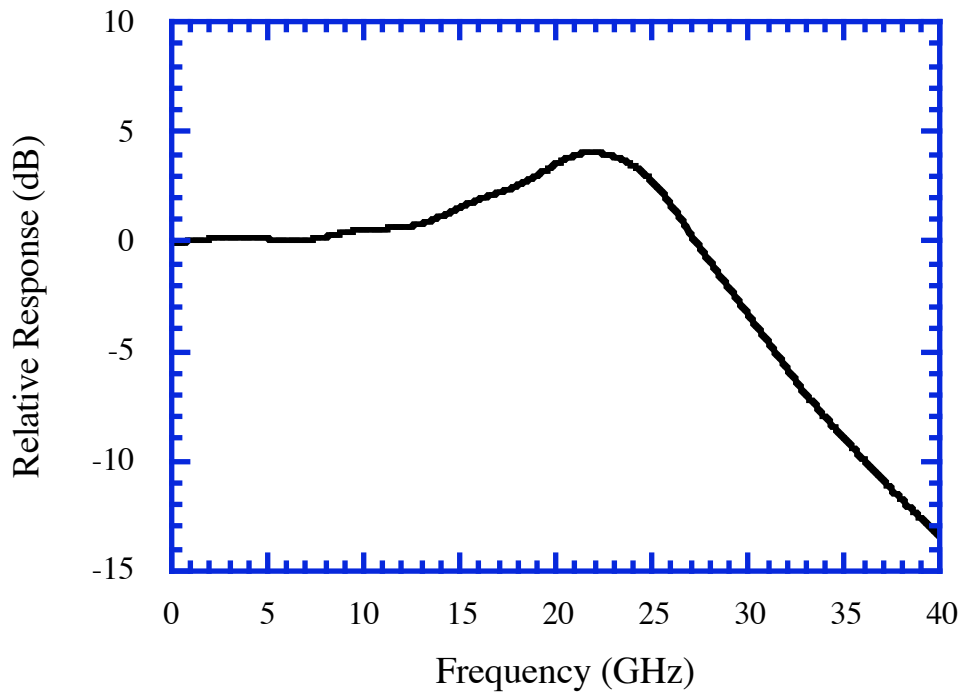


Fig. D.4 Relative passband response (S_{21}) of the equivalent parasitic circuit of Sample C. The modulation response measured for this device is well within the rolloff frequency due to the parasitics.

Fig. D.4 shows the passband response (S_{21}) of the equivalent circuit for Sample C. The - 3 dB bandwidth of the parasitic circuit is in excess of 25 GHz. This is also true for all three of the mounted devices. The largest modulation bandwidth measured in these set of devices is below 19 GHz for Sample A, and the parasitics

should not have any effect on the modulation performance in this range. Thus, the *parasitic-like* low frequency rolloff observed in Sample C can only be due to transport effects.

Another interesting effect here is the peaking in the modulation response of the mounted laser diode due to the bond wire inductance. If the value of this inductance can be carefully controlled during mounting (by controlling the placement of the laser diode relative to the microstrip and the length of the bond wire), then the modulation response can be enhanced at about the point where the intrinsic response begins to rolloff, to increase the overall modulation bandwidth. The drawback is that the pole introduced by this inductive element causes an additional 10 dB/decade rolloff. This is not *really* a disadvantage because it occurs in the region where the intrinsic response is rolling off anyway.

D.2 Independent Diode Series Resistance Measurements

Alternatively the diode series resistance can be determined from the I-V characteristics of the laser diode. This may be used as an independent check on the R_S parameter extracted from the numerical fit to the experimental S_{11} data.

Modeling the laser diode as an ideal $p-n$ junction in series with a resistance R_S , the I-V characteristics can be written as,

$$I = I_o \left[\exp \left(\frac{q(V - IR_S)}{\eta k T} \right) - 1 \right]$$

where I_o is the saturation current, V is the applied voltage and η is the diode ideality factor. The diode series resistance causes an additional voltage drop, IR_S , which must be subtracted from the applied terminal voltage to determine the junction voltage.

This diode equation can also be written in the following differential form,

$$\frac{dV}{dI} = \frac{\eta k T}{q} \left(\frac{1}{I} \right) + R_S$$

The more commonly used form of the above relationship is [7],

$$I \frac{dV}{dI} = I R_S + \frac{\eta k T}{q}$$

If $(I dV/dI)$ is plotted as a function of I , the slope will give the value of the diode series resistance, R_S , and the intercept the value of the diode ideality factor, η . This can be automatically done while measuring the laser I-V curve using the HP 4145B semiconductor parameter analyzer.

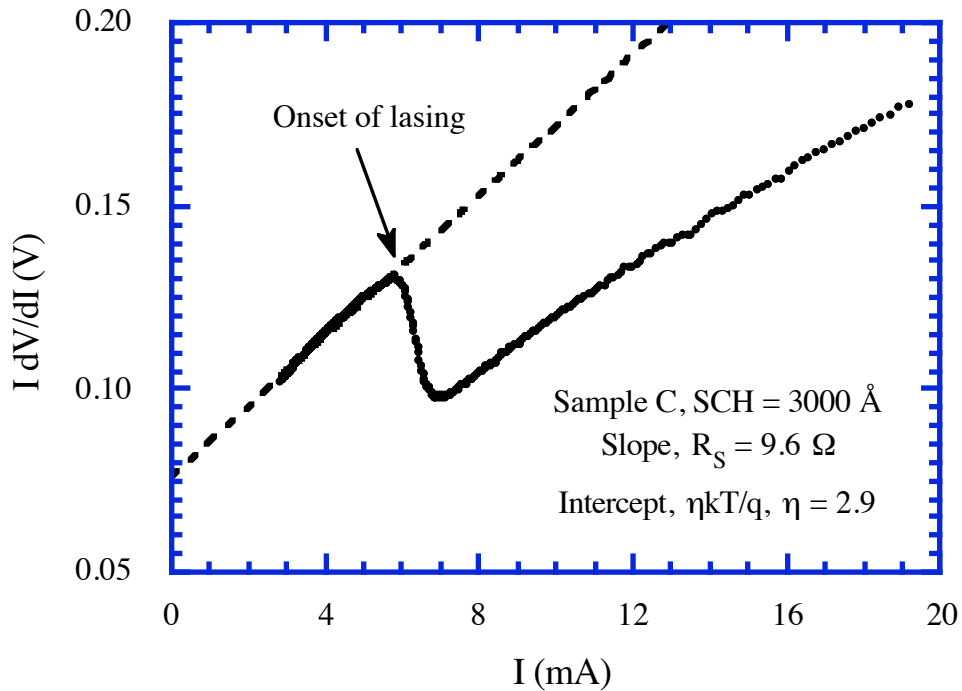


Fig. D.5 $I dV/dI$ as a function of I for Sample C with the widest SCH. The discontinuity in the curve occurs at lasing, and R_S and η are extracted from the straight line fit as shown.

Fig. D.5 shows $(I \, dV/dI)$ plotted as a function of I for Sample C with the widest SCH region. A discontinuity occurs in the curve at threshold. In an ideal semiconductor laser, the carrier density above threshold is clamped at its threshold value. This results in the pinning of the separation of the electron and hole quasi Fermi levels, and the saturation of the junction voltage, V_j , above threshold. The total voltage V across the laser diode above threshold is the sum of the junction voltage at threshold and the voltage drop across the series resistance, R_S .

$$V = (V_j)_{th} + I R_S$$

The derivative dV/dI above threshold is constant and equal to R_S . At threshold the value of $(I \, dV/dI)$ abruptly decreases from $(I R_S + \eta kT/q)$ to $(I R_S)$. This abrupt decrease, which is due to the saturation of the junction voltage at threshold, results in the discontinuity in the $(I \, dV/dI)$ curve as shown for Sample C in Fig. D.5. Thus, for an ideal diode, the extrapolation of the above-threshold part of the $(I \, dV/dI)$ curve should intercept at the origin. This is not the case in the experiments. The non-zero intercept that is experimentally measured has been attributed to presence of contact nonlinearities in the laser diode [8]

The diode equation used here and the derivative that results from it are strictly only applicable below threshold in the absence of stimulated emission [9,10]. Above threshold, the current through the laser diode is determined mainly by the rate of stimulated recombination in the active area. The values for R_S and η are, thus, derived from the straight line fit to the $(I \, dV/dI)$ curve below threshold as shown in Fig. D.5. Further, the diode equation above is derived for the I-V characteristics of a *non-degenerate p-n* junction [9]. This simple theory describes the experimental data

well here, even though the semiconductor laser active region is *degenerate* under forward bias.

The I-V characteristics of Samples A and B were also measured. The values of the diode series resistance and the ideality factor for Samples A, B and C are given in the table below. The measured value of R_S also includes the resistance of the cables and the probe R_C . This is then separately measured.

Sample	SCH Width (Å)	$R_S + R_C$ (Ω)	Ideality Factor, η
A	760	8.1	3.0
B	1500	8.3	3.0
C	3000	9.6	2.9

The value for R_C is 2.3 Ω . If this is accounted for, then the intrinsic diode series resistance is about 6 Ω for Samples A and B, and about 7 Ω for Sample C. These are higher than the values for R_S extracted from the S_{11} data. The value for R_S extracted from the I-V characteristics is dependent on the current region over which the slope of the $(I \, dV/dI)$ curve is measured. Even though the diode equations are only strictly valid below threshold, the $(I \, dV/dI)$ term varies linearly with I above threshold also. As seen from Fig. D.5, above threshold the slope of the curve gradually decreases at larger currents, i.e. R_S is smaller at the current level where the laser diode actually operates. The R_S value measured from the slope of the $(I \, dV/dI)$ curve at high currents agree with the data extracted from the S_{11} measurements.

The determination of R_S from I-V characteristics is more complicated if shunt resistances are present around the active layer. Ref. [10] considers the effects of such

shunt resistances, and Ref. [8], in addition to the leakage current paths, also analyzes the effects of contact nonlinearities.

The diode ideality factor is 3 for all the three samples. For diodes where the current flow is mainly via recombination and generation in the neutral p and n regions, the ideality factor is 1. In the case where the recombination in the space charge region of the p - n junction dominates, the Sah-Noyce-Shockley model results in an ideality factor of 2 [11]. Ideality factors greater than 2 have been shown to be theoretically possible, and experimentally measured ($\eta = 3.2$) in p - n junctions where the current conduction is mainly via recombination (resulting in light emission) in the space charge region [12]. Ideality factors up to 3, in localized regions (in the case of spatially varying recombination current density) of the base-emitter junction have also been calculated for the case of heterostructure bipolar transistors (HBT) [13].

References

1. Distributed by EESOF Inc., Westlake Village, CA.
2. J. Katz, S. Margalit, C. Harder, D. Wilt, and A. Yariv, "The Intrinsic Equivalent Circuit of a Laser Diode," *J. Quantum Electron.*, vol. 17, pp. 4-7, 1981.
3. R. S. Tucker, and I. P. Kaminow, "High-Frequency Characteristics of Directly Modulated InGaAsP Ridge Waveguide and Buried Heterostructure Lasers" *J. Lightwave Technol.*, vol. 2, pp. 385-393, 1984.
4. Ch. S. Harder, B. J. Van Zeghbroeck, M. P. Kesler, H. P. Meier, P. Vettiger, D. J. Webb, and P. Wolf, "High-Speed GaAs/AlGaAs Optoelectronic Devices for Computer Applications," *IBM J. Res. Develop.*, vol. 34, pp. 568-584, 1990.
5. S. C. Kan, and K. Y. Lau, "Intrinsic Equivalent Circuit of Quantum-Well Lasers," *Photon. Tech Lett.*, vol. 4, pp. 528-538, 1992.
6. R. S. Tucker, and D. J. Pope, "Circuit Modeling of the Effect of Diffusion on Damping in a Narrow-Stripe Semiconductor Laser," *J. Quantum Electron.*, vol. 19, pp. 1179-1183, 1983.
7. T. L. Paoli, and P. A. Barnes, "Saturation of the Junction Voltage in Stripe-Geometry (AlGa)As Double-Heterostructure Junction Lasers," *Appl. Phys. Lett.*, vol. 28, pp. 714-716, 1976.
8. P. D. Wright, W. B. Joyce, and D. C. Craft, "Electrical Derivative Characteristics of InGaAsP Buried Heterostructure Lasers," *J. Appl. Phys.*, vol. 53, pp. 1364-1372, 1982.
9. M. J. Adams, and P. T. Landsberg, "The Theory of the Injection Laser," in *Gallium Arsenide Lasers*, pp. 5-79, C. H. Gooch:Ed., New York:Wiley-Interscience, 1969.
10. P. A. Barnes, and T. L. Paoli, "Derivative Measurements of the Current-Voltage Characteristics of Double-Heterostructure Injection Lasers," *J. Quantum Electron.*, vol. 12, pp. 633-639, 1976.

11. C. -T Sah, R. N. Noyce, and W. Shockley, "Carrier Generation and Recombination in p - n Junctions and p - n Junction Characteristics," *Proc. IRE*, vol. 45, pp. 1228, 1957
12. T. N. Morgan, "Luminescence and Recombination Through Defects in p - n Junctions," *Phys. Rev.*, vol. 139, pp. A294-A299, 1965.
13. S. Tiwari, and D. J. Frank, "Analysis of the Operation of GaAlAs/GaAs HBTs," *Trans. Electron Devices*, vol. 36, pp. 2105-2121, 1989.